ETSI GR RIS 004 V1.1.1 (2025-03)

GROUP REPORT

Reconfigurable Intelligent Surfaces (RIS); Implementation and Practical Considerations

Disclaimer

The present document has been produced and approved by the Reconfigurable Intelligent Surfaces (RIS) ETSI Industry Specification Group (ISG) and represents the views of those members who participated in this ISG.
It does not necessarily represent the views of the entire ETSI membership.

Reference
DGR/RIS-004

Keywords
cellular, radio, radio measurements, RIS

ETSI

650 Route des Lucioles
F-06921 Sophia Antipolis Cedex - FRANCE

Tel.: +33 4 92 94 42 00 Fax: +33 4 93 65 47 16

Siret N° 348 623 562 00017 - APE 7112B
Association à but non lucratif enregistrée à la
Sous-Préfecture de Grasse (06) N° w061004871

Important notice

The present document can be downloaded from the ETSI Search & Browse Standards application.

The present document may be made available in electronic versions and/or in print. The content of any electronic and/or print versions of the present document shall not be modified without the prior written authorization of ETSI. In case of any existing or perceived difference in contents between such versions and/or in print, the prevailing version of an ETSI deliverable is the one made publicly available in PDF format on ETSI deliver repository.

Users should be aware that the present document may be revised or have its status changed, this information is available in the Milestones listing.

If you find errors in the present document, please send your comments to the relevant service listed under Committee Support Staff.

If you find a security vulnerability in the present document, please report it through our Coordinated Vulnerability Disclosure (CVD) program.

Notice of disclaimer & limitation of liability

The information provided in the present deliverable is directed solely to professionals who have the appropriate degree of experience to understand and interpret its content in accordance with generally accepted engineering or other professional standard and applicable regulations.
No recommendation as to products and services or vendors is made or should be implied.
No representation or warranty is made that this deliverable is technically accurate or sufficient or conforms to any law and/or governmental rule and/or regulation and further, no representation or warranty is made of merchantability or fitness for any particular purpose or against infringement of intellectual property rights.
In no event shall ETSI be held liable for loss of profits or any other incidental or consequential damages.

Any software contained in this deliverable is provided "AS IS" with no warranties, express or implied, including but not limited to, the warranties of merchantability, fitness for a particular purpose and non-infringement of intellectual property rights and ETSI shall not be held liable in any event for any damages whatsoever (including, without limitation, damages for loss of profits, business interruption, loss of information, or any other pecuniary loss) arising out of or related to the use of or inability to use the software.

Copyright Notification

No part may be reproduced or utilized in any form or by any means, electronic or mechanical, including photocopying and microfilm except as authorized by written permission of ETSI.
The content of the PDF version shall not be modified without the written authorization of ETSI.
The copyright and the foregoing restriction extend to reproduction in all media.

© ETSI 2025.
All rights reserved.

Contents

Intellectual Property Rights

Essential patents

IPRs essential or potentially essential to normative deliverables may have been declared to ETSI. The declarations pertaining to these essential IPRs, if any, are publicly available for **ETSI members and non-members**, and can be found in ETSI SR 000 314: *"Intellectual Property Rights (IPRs); Essential, or potentially Essential, IPRs notified to ETSI in respect of ETSI standards"*, which is available from the ETSI Secretariat. Latest updates are available on the ETSI IPR online database.

Pursuant to the ETSI Directives including the ETSI IPR Policy, no investigation regarding the essentiality of IPRs, including IPR searches, has been carried out by ETSI. No guarantee can be given as to the existence of other IPRs not referenced in ETSI SR 000 314 (or the updates on the ETSI Web server) which are, or may be, or may become, essential to the present document.

Trademarks

The present document may include trademarks and/or tradenames which are asserted and/or registered by their owners. ETSI claims no ownership of these except for any which are indicated as being the property of ETSI, and conveys no right to use or reproduce any trademark and/or tradename. Mention of those trademarks in the present document does not constitute an endorsement by ETSI of products, services or organizations associated with those trademarks.

DECT™, **PLUGTESTS™**, **UMTS™** and the ETSI logo are trademarks of ETSI registered for the benefit of its Members. **3GPP™**, **LTE™** and **5G™** logo are trademarks of ETSI registered for the benefit of its Members and of the 3GPP Organizational Partners. **oneM2M™** logo is a trademark of ETSI registered for the benefit of its Members and of the oneM2M Partners. **GSM**® and the GSM logo are trademarks registered and owned by the GSM Association.

Foreword

This Group Report (GR) has been produced by ETSI Industry Specification Group (ISG) Reconfigurable Intelligent Surfaces (RIS).

Modal verbs terminology

In the present document "**should**", "**should not**", "**may**", "**need not**", "**will**", "**will not**", "**can**" and "**cannot**" are to be interpreted as described in clause 3.2 of the ETSI Drafting Rules (Verbal forms for the expression of provisions).

"**must**" and "**must not**" are **NOT** allowed in ETSI deliverables except when used in direct citation.

1 Scope

The present document identifies Reconfigurable Intelligent Surfaces (RIS) relevant use cases with corresponding general Key-Performance-Indicators (KPIs), deployment scenarios operational requirements for each identified use case. KPIs and operational requirements will include system/link performance, spectrum, co-existence and security.

2 References

2.1 Normative references

Normative references are not applicable in the present document.

2.2 Informative references

References are either specific (identified by date of publication and/or edition number or version number) or non-specific. For specific references, only the cited version applies. For non-specific references, the latest version of the referenced document (including any amendments) applies.

NOTE: While any hyperlinks included in this clause were valid at the time of publication, ETSI cannot guarantee their long term validity.

The following referenced documents are not necessary for the application of the present document but they assist the user with regard to a particular subject area.

[i.1] ETSI GR RIS 001: "Reconfigurable Intelligent Surfaces (RIS); Use Cases, Deployment Scenarios and Requirements".

[i.2] ETSI GR RIS 002: "Reconfigurable Intelligent Surfaces (RIS); Technological challenges, architecture and impact on standardization".

[i.3] ETSI GR RIS 003: "Reconfigurable Intelligent Surfaces (RIS); Communication Models, Channel Models, Channel Estimation and Evaluation Methodology".

[i.4] George C. Alexandropoulos, et. all: "RIS-Enabled Smart Wireless Environments: Deployment Scenarios, Network Architecture, Bandwidth and Area of Influence", submitted to EURASIP Journal.

[i.5] Directive 2014/53/EU of the European Parliament and of the Council of 16 April 2014.

[i.6] A. Haskou, and H. Khaleghi: "On the effect of RIS phase quantization on communications system performances", 2023 International Wireless Communications and Mobile Computing (IWCMC), Marrakesh, Morocco, pp. 1406-1411, 2023.

[i.7] ETSI TS 138 101-1: "5G; NR; User Equipment (UE) radio transmission and reception; Part 1: Range 1 Standalone (3GPP TS 38.101-1 Release 17)".

[i.8] A. Tishchenko, A. Ali, A. Araghi, P. Botham, F. Burton and M. Khalily: "Autonomous Reconfigurable Intelligent Surface based on Highly-Efficient Solar Cells," 2023 17th European Conference on Antennas and Propagation (EuCAP), Florence, Italy, pp. 1-5, 2023.

[i.9] A. Haskou and H. Khaleghi: "An Efficient and Easy-to-Implement Method for SLL Reduction in RIS-Aided Systems". TechRxiv, 31-August-2023.

[i.10] H. Taghvaee et al.: "Scalability Analysis of Programmable Metasurfaces for Beam Steering", in IEEE Access, vol. 8, pp. 105320-105334, 2020.

[i.11] Fangzhou Wang, and A. Lee Swindlehurst: "Applications of Absorptive Reconfigurable Intelligent Surfaces in Interference Mitigation and Physical Layer Security", 2023.

[i.12] S. Zeng et al.: "Intelligent Omni-Surfaces: Reflection-Refraction Circuit Model, Full-Dimensional Beamforming, and System Implementation", in IEEE Transactions on Communications, vol. 70, no. 11, pp. 7711-7727, November. 2022.

[i.13] Recommendation ITU-R SM.329: "Unwanted emissions in the spurious domain".

[i.14] ETSI GR RIS 006: "Reconfigurable Intelligent Surfaces (RIS); Multi-functional Reconfigurable Intelligent Surfaces (RIS): Modelling, Optimisation, and Operation".

[i.15] R. Liu, J. Dou, P. Li, J. Wu and Y. Cui: "Simulation and Field Trial Results of Reconfigurable Intelligent Surfaces in 5G Networks", in IEEE Access, vol. 10, pp. 122786-122795, 2022.

[i.16] M. Rossanese, P. Mursia, A. Garcia-Saavedra, V. Sciancalepore, A. Asadi, and X. Costa-Perez: "Design and validation of scalable reconfigurable intelligent surfaces", Computer Networks, vol. 241, no.110208, 2024.

[i.17] H. Rajabalipanah, K. Rouhi, A. Abdolali, S. Iqbal, L. Zhang and S. Liu: "Real-time terahertz meta-cryptography using polarization-multiplexed graphene-based computer-generated holograms", in Nanophotonics, vol. 9, no. 9, pp. 2861-2877, 2020.

[i.18] J. B. Gros, V. Popov, M. A. Odit, V. Lenets, G. Lerosey: "A Reconfigurable Intelligent Surface at mmWave Based on a Binary Phase Tunable Metasurface", IEEE Open Journal of the Communications Society, vol. 2, pp. 1055–1064, May 2021.

[i.19] ETSI GR RIS 007: "Reconfigurable Intelligent Surfaces (RIS); Near-field Channel Modeling and Mechanics".

[i.20] C.-L. Liao, Y.-H. Lin, I. Lin, and C.-F. Yang: "Performance Evaluation of RU and RIS Based on OTA Mode Near Field and Bistatic Measurement Systems", Antenna Measurement Techniques Association Symposium (AMTA), October 2023.

[i.21] T.-H. Lee and W. D. Burnside: "Compact Range Reflector Edge Treatment Impact on Antenna and Scattering Measurements", IEEE Trans. Antennas Propagat., vol. 45, no. 1, pp. 57-65, January 1997.

[i.22] Kitayama D, Hama Y, Goto K, Miyachi K, Motegi T, Kagaya O.: "Transparent dynamic metasurface for a visually unaffected reconfigurable intelligent surface: controlling transmission/reflection and making a window into an RF lens", in Opt. Express, 29(18):29292-29307, 2021.

3 Definition of terms, symbols and abbreviations

3.1 Terms

For the purposes of the present document, the following terms given in ETSI GR RIS 001 [i.1], in ETSI GR RIS 002 [i.2] and ETSI GR RIS 003 [i.3] apply.

3.2 Symbols

Void.

3.3 Abbreviations

For the purposes of the present document, the following abbreviations apply:

FPGA	Field Programmable Gate Array
KPI	Key Performance Index
RIS	Reconfigurable Intelligent Surfaces

4 General hardware aspects of RIS

4.0 Unit-cell principle of operation

The number of states of a unit-cell may be represented by a number of bits used based on the RIS implementation. RIS, when built using locally switchable elements, can be described as a bit or state matrix and digitally controlled through reconfigurable devices such as Field-Programmable Gate Arrays (FPGAs). Consequently, discretizing the electromagnetic characteristics of the unit-cell (amplitude and phase) realizes simple wave manipulation with straightforward tunability.

4.1 Quantized Phase Shifts

An ideal RIS unit cell is supposed to provide continuous phase shift values with infinite resolutions. However, in real-world implementations, the resolutions of phase shifters/diodes/varactors are generally limited, resulting in quantized phase shifts and degraded beamforming performances. The degradation of beamforming gains with different phase quantization, imperfection, and RIS implementation constraints need to be thoroughly investigated. Figure 4.1.1-1 and Figure 4.1.1-2 show the beamforming gain of RIS when a RIS aims to re-radiate the incident signals into different steering directions for different number of RIS elements respectively. With 1-bit quantization, the beamforming gain is generally about 3-4 dB less than the scenario with ideal phase shift control, which does not change significantly with the number of elements on the RIS panel. The beamforming gain loss caused by phase quantization can only be minimized in some certain re-radiating directions (e.g. when the re-radiation is subject to Snell's law), and such re-radiating directions correspond to peaks in Figure 4.1.1-1 and Figure 4.1.1-2.

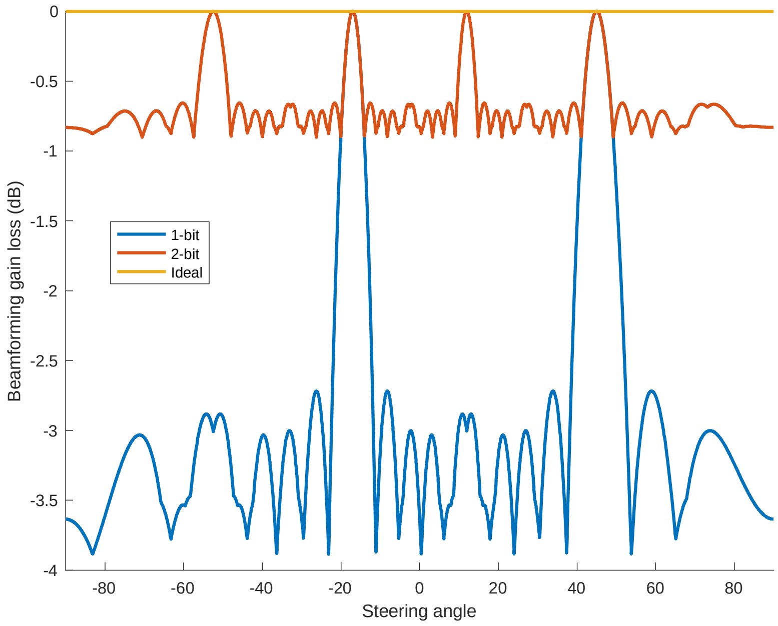

Figure 4.1.1-1: 10 × 10 RIS beamforming gain for varying steering angle obtained by using different phase shift control resolutions

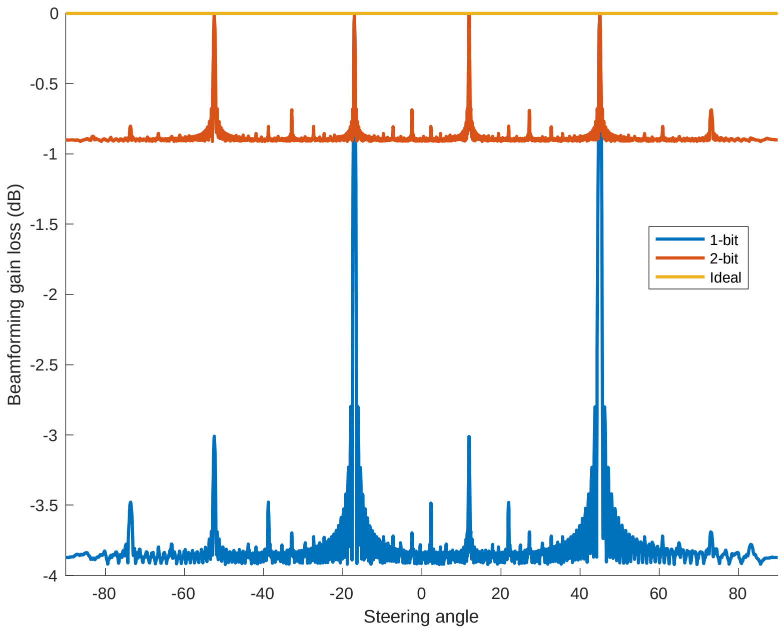

NOTE: The incident angle is assumed to be -45 degrees in both examples. The yellow curve represents phase shift control with infinite resolution. Blue and red curves represent phase shift controls with 1-bit and 2-bit quantization, respectively.

Figure 4.1.1-2: 100 × 100 RIS beamforming gain for varying steering angle obtained by using different phase shift control resolutions

An RIS unit cell can also provide phase shift values quantized with multiple bits. The function can be realized by using phase shifters with higher resolution or multiple diodes in the same RIS unit. Figure 4.1.1-1 and Figure 4.1.1-2 show the beamforming gain of RIS with 2-bit quantization, and the beamforming gain loss is generally less than 1 dB. Therefore, the resolution of 2-bit quantization might be sufficient for RIS fabrication.

In some scenarios, the total number of control bits can be a constraint of RIS fabrication, which implies that the RIS can be larger with low phase resolution per unit. Although the gain improvement of 2-bit quantization over 1-bit quantization is around 3 dB, using 1-bit quantization leads to double RIS elements, which can provide around 6 dB gain. Therefore, with constraints on the total control bits, multi-bit quantization may not be an optimal solution for RIS fabrication. Generally, the requirement in terms of phase quantization can be determined depending on use-cases, deployment scenarios, accuracy requirements, etc. Therefore, in certain cases, a finer phase quantization, while in other cases coarser phase quantization may be needed.

Assuming an RIS with a large number of elements N, using far-field approximations, it can be shown that in absence of a direct Tx-Rx path, using i-bit phase quantization leads to a uniform phase quantization error $\psi_{m,n} \sim U\left(-\frac{\pi}{2^i}, \frac{\pi}{2^i}\right)$. Then, the relative received signal level, i.e. the ratio between the received signal with phase quantization and the received signal without phase quantization, is given by [i.9]:

$$S_{relative} = \frac{E_{\psi m,n}\left(s_{rx_q}\right)}{s_{rx}} = sinc\left(\frac{\pi}{2^i}\right)$$

where $s_{rx_q}$is the received signal using phase quantization, s_{rx} is the received signal without phase quantization and $\psi_{m,n}$ is the difference between the optimal phase and the quantized phase.

Figure 4.1.1-3 shows the effect of the phase quantization on the relative received power (calculated as $P_{relative}$=$20\ log(S_{relative})$). As it can be seen, using 1-bit and 2-bit quantization lead to around 3,9 dB and 0,9 dB loss in the received power.

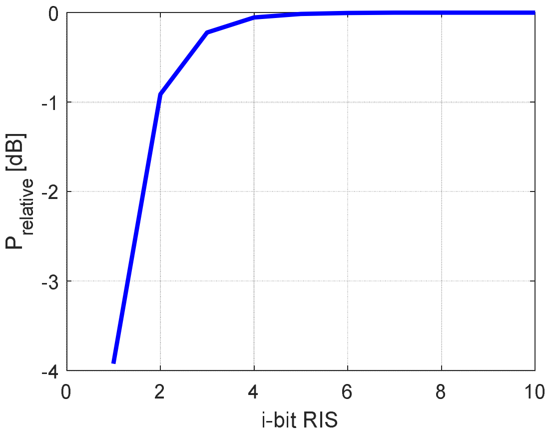

Figure 4.1.1-3: Effect of the quantization step on relative received power

In the case there is also a direct Tx-Rx path, the relative received signal is given by:

$$S_{relative} = \frac{\frac{\sqrt{G_d}}{d_d} + \frac{N\sqrt{G}\lambda}{4\pi d_{tx} d_{rx}} sinc\left(\frac{\pi}{2^i}\right)}{\frac{\sqrt{G_d}}{d_d} + \frac{N\sqrt{G}\lambda}{4\pi d_{tx} d_{rx}}}$$

where λ is the free-space wavelength; d_{tx}, d_{rx} are respectively the distance from the RIS central element to Tx and Rx; G represents the overall gain between Tx and Rx through RIS; d_d is the direct distance between Tx and Rx and G_d is the overall direct path gain.

As it can be seen, in this case, the relative received signal is highly dependant on the direct path gain and distance, and it is always higher than the case without direct path. Indeed, in the case where the direct path is the dominant one, i.e. $\frac{\sqrt{G_d}}{d_d} \gg \frac{N\sqrt{G}\lambda}{4\pi d_{tx} d_{rx}}$, this equation reduces to $S_{relative} \approx 1$. And in the case where the indirect path is the dominant one, i.e. $\frac{N\sqrt{G}\lambda}{4\pi d_{tx} d_{rx}} \gg \frac{\sqrt{G_d}}{d_d}$, this equation reduces to $S_{relative} \approx sinc\left(\frac{\pi}{2^i}\right)$. This means that, for example, in the case of a 1-bit RIS the relative loss in the received power can vary from 0 dB to 3,9 dB depending on the RIS position (relative to Tx and Rx).

4.2 Metasurface designs

RISs are composed of certain arrangement controllable resonators (unit-cells). These unit-cells can be implemented based on the deployment scenarios and requirements. For instance, in the Frequency Range 1 (FR1) regime they are typically metallic patches stacked on top of a dielectric. If the unit-cells are in the scale of subwavelength, they will form a composite called metasurface. The subwavelength granularity of these unit-cells confers metasurfaces with exceptional control of EM waves, that can even realize some unnatural EM properties such as negative permittivity (ϵ_r) or permeability (μ_r). With this feature, EM characteristics of impinging waves can be engineered.

One of the many challenges posed by this approach concerns the design and development of metasurfaces. This task is largely hindered by the unique combination of resource constraints and communication requirements of this new networking scenario, which prevents the use of conventional techniques and requires radically new solutions instead. The performance of RIS metasurface depends on the size of the unit-cells, the number of unit-cell states, and its overall size. On the other hand, there are costs and energy overheads associated with the fabrication and operation of metasurfaces that also scale with the aforementioned factors. Hence, to build an RIS capable of satisfying a set of application-specific requirements with the minimum cost, it becomes necessary to quantify the main scaling trends and trade-offs of the underlying metasurface design.

4.3 Switching element

RIS reconfiguration can be achieved through element inclusion (PIN diodes, varactors, etc.) within unit-cells. The tuning factor can be applied to unit-cells individually and to select the unit-cell state (each unit-cell can acquire different state from a selective number of states N_s). The tuning factor can be used for frequency tuning or function adjustment.

Realization of reconfigurable metasurfaces requires a network of wires or vias to convey the command signal from the control unit (i.e. RIS controller) to the surface.

The intensity and phase of reflecting EM waves are controlled by the variation of impedance Z_m in the unit cells through the switching element inclusion (PIN diodes, varactors, etc.). The conductive layer of the RIS can be described as a penetrable equivalent impedance surface $\mathbf{Z}$, which relates the tangential electric field $\boldsymbol{E_t}$ to the discontinuity of the average tangential magnetic field $\boldsymbol{H_t}$ across the conductive layer. The incident EM plane wave is characterized in terms of transverse wavenumber k_{y0} and the periodicity of RIS elements along the impedance profile d:

$$Z(y) = \sum_m Z_m e^{-j\frac{2\pi m}{d}y}$$

Then, the Floquet waves expansion of the currents induced in the equivalent impedance boundary in the $\hat{\boldsymbol{y}}$ direction can be expressed as:

$$I(y)\hat{\boldsymbol{y}} = \hat{\boldsymbol{z}} \times \boldsymbol{H_t} = \sum_n I_n e^{-jk_{yn}y}\hat{\boldsymbol{y}}$$

where the Floquet wavenumbers are defined as $k_{yn} = k_{y0} + \frac{2\pi}{d_z}n$,

m is a constant denoting the number of unit cells, and n represents individual reflecting coefficients for propagating diffracting harmonics of index $n = 0, \mp 1, \mp 2, \ldots$. The sum of n-induced currents on the equivalent impedance boundary provides the accurate description of RIS, with the dispersion characteristics given in terms of frequency dispersion diagrams showing the transverse wavenumber as a function of the propagation direction for different frequencies. This relationship is illustrated in Figure 4.3-1.

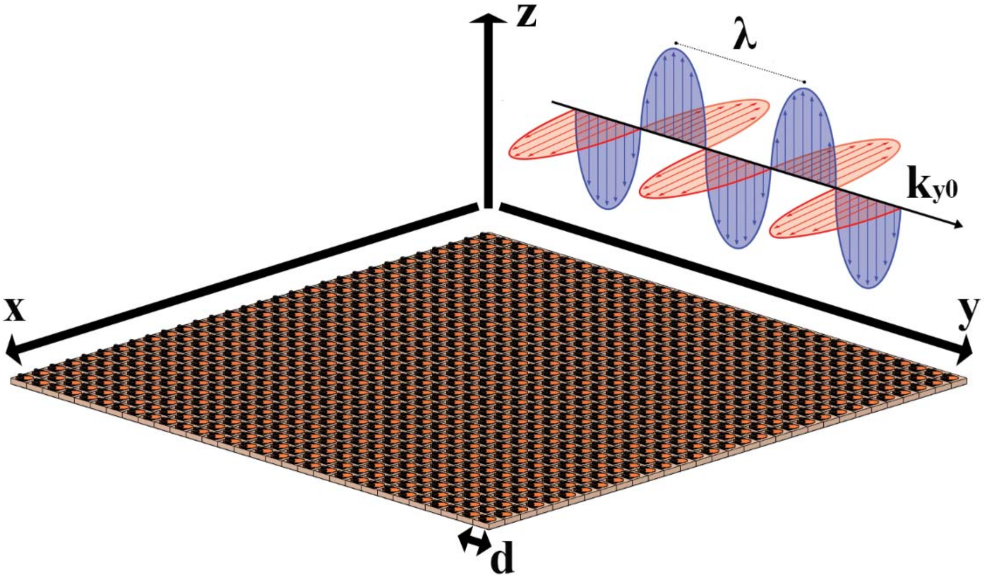

Figure 4.3-1: RIS modeled as an impedance boundary characterized by a transverse wavenumber k_{y0}

RIS can be realized by using various phase switching methods, where each method has its own advantages and disadvantages as summarized in Table 5.3.1-1 of ETSI GR RIS 002 [i.2]. As outlined in the table, the selection of the switching element is typically based on the following:

- Frequency of operation
- Switching speed
- Power consumption
- Insertion loss
- Size
- Cost

Out of the items outlined, only varactor diodes and liquid crystals can provide continuous phase switching as a function of the applied voltage that is typically regulated with Digital to Analogue Converters (DACs). This method of control is called "Analogue" because any phase value can be realized on such RIS. Other phase switching methods such as PIN diodes can only represent the value of 0 or 1, and this method is called "1-bit Digital", because only the pre-defined phase values can be realized on such RIS. However, if one unit cell features several switching elements, an "N-bit Digital" switching method can be realized, where N corresponds to the amount of switching elements within the unit cell. The design process of multi-bit digital RISs becomes progressively more complex with the amount of added switching elements. Additionally, this increases the number of control signals from the RIS controller.

The switching speed of unit cell elements needs to be fast enough to realize Time Division Duplexing (TDD) framework for operation in multi-user environments, which is described in clause 7.2.1 of ETSI GR RIS 002 [i.2]. For varactor diodes, PIN diodes and FETs it is typically in the region of nanoseconds, but the switching speed of liquid crystals and MEMS switches is in the region of milliseconds.

Although varactor diodes have negligible power consumption across the diode itself (< 1 mW), their application in analogue mode requires the use of DACs and operational amplifiers, which increases the overall power consumption of such RIS. Multiple unit cells can share the same control channel on an analogue RIS, for example in a diagonal RIS each column can be driven by a single DAC channel. However, this restricts beam steering to a single plane.

In case of a digital RIS, PIN diodes have higher power consumption across the diode itself (~5 mW) but can be driven directly from the microcontroller with CMOS logic. Digital RIS can also be implemented with multiple varactor diodes on the same unit cell that are switching between two or more voltage levels, but it requires the addition of voltage boosters and increases complexity of the unit cell design.

Most base stations are equipped with orthogonal and dual-polarized antenna arrays and most mobile user terminals are integrated with impurely polarized internal antennas. Hence, the unit cells of a RIS array should be designed with dual-polarization functionality in order to control any incoming EM wave with a random polarization successfully. The described scenarios below illustrate two RIS examples for the single- and dual-polarization RIS configurations, respectively. As shown in Figure 4.3-2, when the RIS design is specific to supporting merely one polarization orientation, only the polarized incident signals fit for the designed polarization are able to enhance the beamforming gain, whereas those whose polarization is orthogonal to the designed one cannot see any EM-field reconfigurability. By contrast, if a dual-polarized RIS is deployed instead, as shown in Figure 4.3-3, it will gain considerable advantage such that the orthogonally polarized signals simultaneously showcase an improvement in focusing the reflected waves on an aimed direction. This holds effective too when the EM-fields rotate by some inclination angle, which is further set forth in Figure 4.3-4 and Figure 4.3-5. Suppose that the radio wave groups propagate towards a unipolarised RIS at an incident angle of either 45 degrees or -45 degrees in Figure 4.3-3, both the radio wave groups of orthogonal polarizations sustain a roughly 3 dB polarization mismatch loss as compared to a dual-polarized RIS in Figure 4.3-5.

To support dual-polarized unit cell design for a RIS, it may need to integrate more than one phase switching elements for phase control of the incoming orthogonally polarized EM waves. On the other hand, this may increase the overall power consumption and the complexity of control signalling and circuit designs.

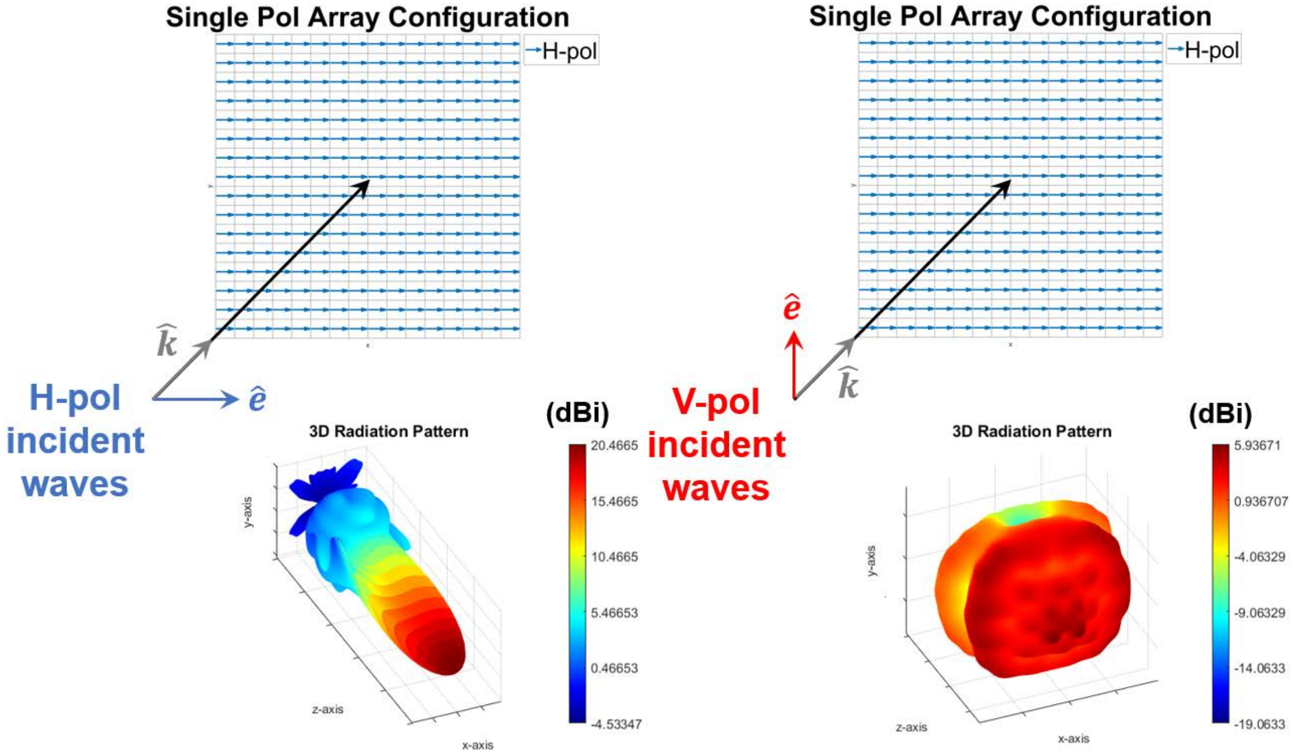

Figure 4.3-2: Scenarios of orthogonally polarized EM waves impinging on a RIS which only support specific polarization control and their corresponding radiation characteristics

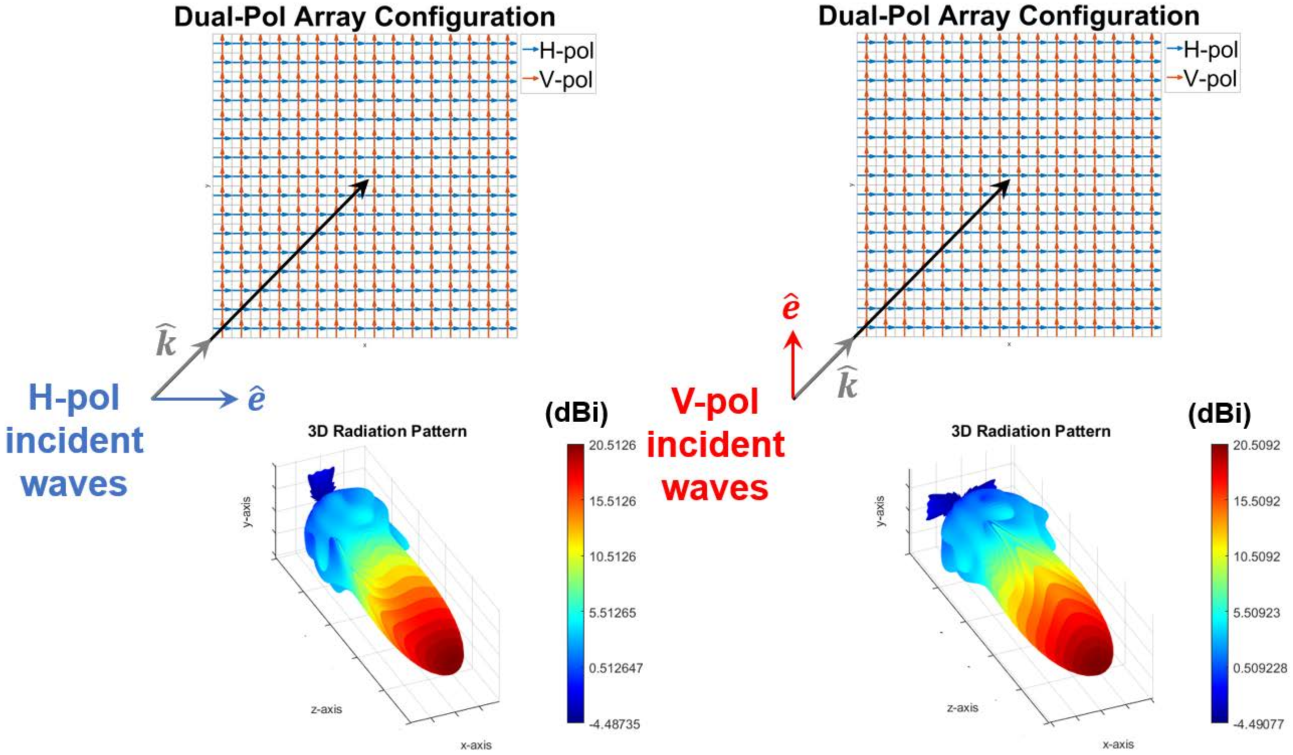

Figure 4.3-3: Scenarios of orthogonally polarized EM waves impinging on a RIS which fully support dual polarization control and their corresponding radiation characteristics

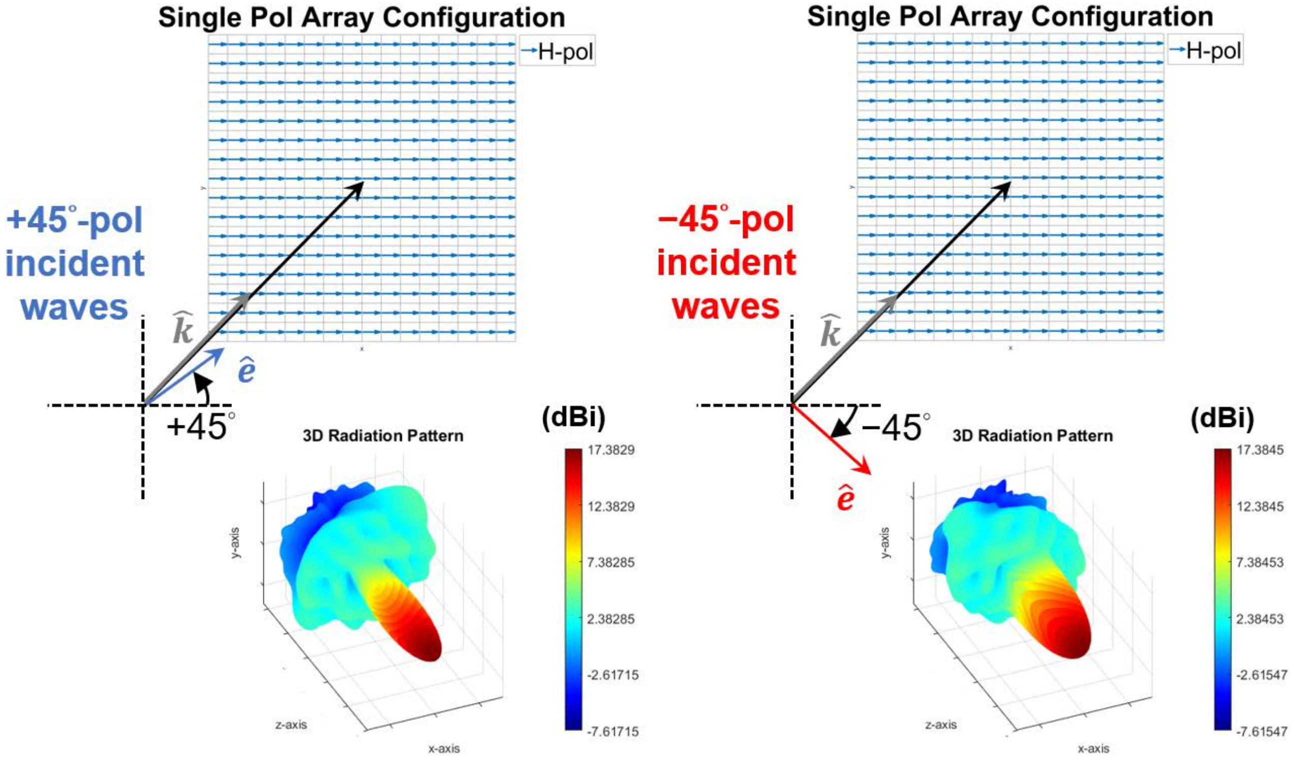

Figure 4.3-4: Unipolarised RIS illumination scenarios and radiation characteristics of orthogonally polarized EM waves impinging on a RIS at a slant angle of 45 degrees and -45 degrees with respect to the RIS arrangement

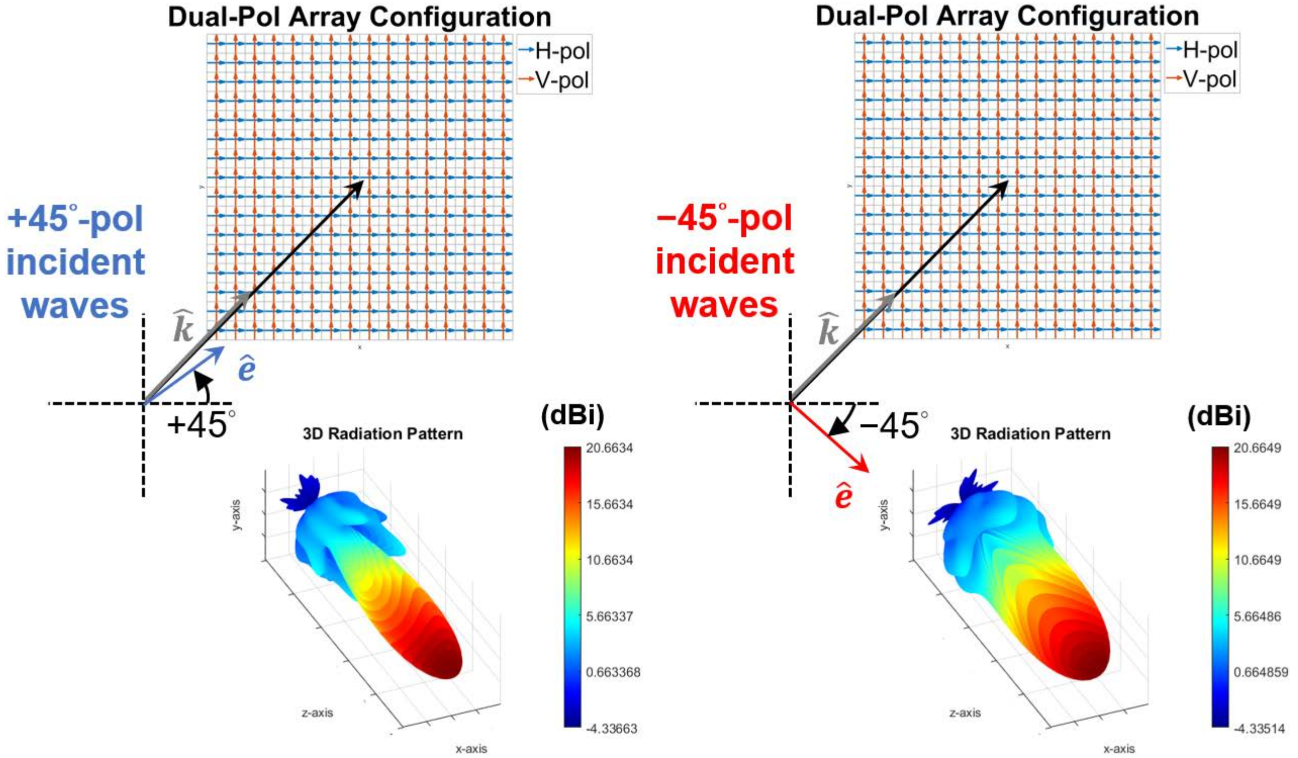

Figure 4.3-5: Dual-polarized RIS illumination scenarios and radiation characteristics of orthogonally polarized EM waves impinging on a RIS at a slant angle of 45 degrees and -45 degrees with respect to the RIS arrangement

4.4 RIS controller

Critical design aspects for RIS controller typically include:

- Power consumption
- Switching speed
- Cost

The selection of electronic components will vary depending on the phase switching mode, which could be either analogue or digital. The power consumption of the RIS controller is largely shaped by the number of required control lines and GPIO pins, which drastically increases in case of 2-Dimensional beam steering mode of operation. Digital logic expanders and transistor switching matrices can be used to reduce the number of utilized GPIO pins on the microcontroller/FPGA, but inevitably they add to the total system delay, which can be expressed as follows:

$$d_T = d_{sw} + d_{CPU} + d_{DAC} + \sum_{m=1}^{M} d_g + \sum_{m=1}^{M} d_p$$

where d_{sw} is the switching delay of the unit cell switching element, d_{CPU} is the microcontroller time delay that includes the rise/fall time, d_{DAC} is the time delay of the DAC in case of analogue switching method, M indicates the number of logic elements in the chain, d_g is the time delay of each additional logic gate in the chain and d_p is the propagation delay for each path in the dielectric material.

It can be experimentally shown that the total system delay is largely dominated by the d_{DAC} in an analogue RIS, therefore a digital RIS has the benefit of faster switching speed. However, the actual requirement for d_T will be dictated by the operational environment, which is subject to the 5G NR frame structure. This requirement can be calculated based on the Subcarrier Spacings (SCSs) specified in Table 5.3.2-1 of ETSI TS 138 101-1 [i.7], which are different for FR1 and FR2. For example, in a downlink dominated scenario, the entire Channel State Information (CSI) from the UE could be contained within a single time slot. Assuming FR1 frequency band and 15 kHz SCS, the d_T should be less than 1 ms to prevent packet loss during UE movement.

4.5 RIS interfaces

The RIS as a whole can be modelled as the combination of RIS controller and RIS panel (see Figure 4.5-1). The RIS panel comprises a group of elements, which can reflect, refract, or absorb incident radio waves. The various types of RIS will be detailed in later clauses of the present document. The RIS controller refers to a component of RIS, responsible for configuring the RIS elements to achieve a wanted way of manipulating the incident radio wave, potentially processing any signalling received from another network node. The configuration of the RIS element by the microcontroller is conveyed through control signalling from the RIS controller. Inside RIS, one interface is the interface between the RIS microcontroller and RIS panel to transmit the control signals.

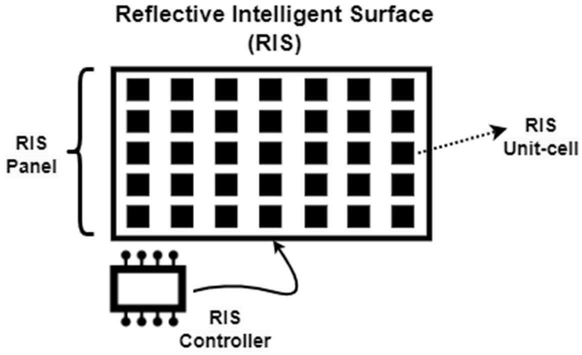

Figure 4.5-1: Illustration of a RIS comprising a RIS controller and a RIS panel

Integration of RIS into the network facilitates various applications, extending beyond the coverage-focused roles of integrated access and backhaul and network-controlled repeaters. The RIS multi-functionality allows the use range to expand from improving coverage to enabling wireless power transfer, supporting ambient backscatter communications, enhancing positioning accuracy, and strengthening secure communication.

RIS controlling strategies may include BS/AP-controlled (through one or more BS/AP) and UE-controlled (one or more UEs), see Figure 4.5-2. This illustration follows closely the methods of controlling RIS that have been previously detailed in ETSI GR RIS 002 [i.2].

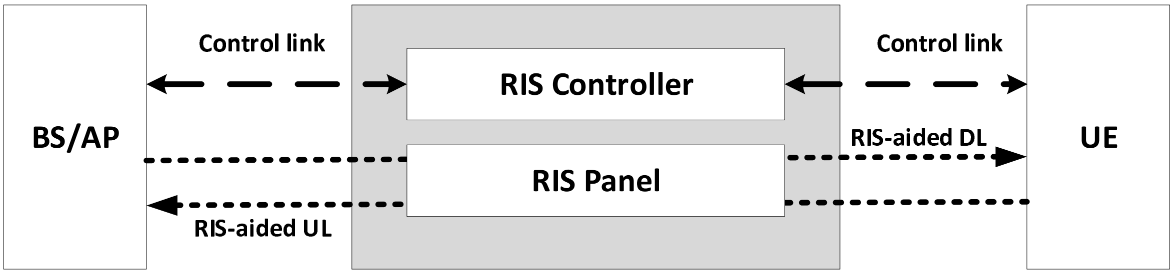

Figure 4.5-2: RIS architecture where RIS is configured from the BS/AP or UE using control signalling

In the downlink (e.g. BS/AP-controlled RIS), the control information can be transmitted from the BS to the RIS via the air interface, such as the Physical Downlink Control Channel (PDCCH) or the Physical Downlink Shared Channel (PDSCH) in the 5G NR architecture. In the uplink (e.g. UE-controlled RIS), the control information can be transmitted from the UE to the RIS via a direct communication interface, such as the Physical Sidelink Control Channel (PSCCH) or Physical Sidelink Shared Channel (PSSCH) in the 5G NR architecture. Moreover, for a RIS with UL transmission capability, the feedback information (e.g. ACK-NACK) for the received control information can be transmitted from the RIS to the BS via the air interface or transmitted from the RIS to the UE via a direct communication interface.

The application of back-scattering communication via digital coding on RIS and the meta-cryptography proposed in [i.17] may be also considered. Encoded patterns may be transferred between various network devices over short distances, allowing continuous network probing and authentication, as well as a secure RIS configuration data transfer. Therefore, increasing the overall security of the network and allowing it to dynamically configure RIS.

4.6 RIS power source

When considering the power source requirements for RIS, the power consumption evaluation of all components of the RIS is needed. Typically, for a passive RIS, the following components are considered:

- RIS controller/interface: RIS controller is responsible for processing any control information that it may receive from the controlling node. Power consumption of the RIS controller primarily depends on the frequency of control information, i.e. how frequent the control information is received for updating the RIS configuration. The processed information is then applied to the unit cells via the RIS interface that generates the required voltage/current to adjust the state of the switching elements for changing properties of the metamaterial.

- RIS unit cells: Power consumption of the unit cells depends on factors including the type of switching elements to change the state of unit cells, number of unit cells, bit resolution for phase shifts and polarization mode i.e. single or dual polarization. As described in clause 4.3, there can be different types of switching elements and the selection of particular switching element is dependent on a number of factors including power consumption.

For illustration, the total power consumption for a PIN diode based RIS can be determined as follows (considering each unit cell has a dedicated set of PIN diodes as switching elements):

$$P_{total} = P_{control/interface} + P_{metasurface,}$$

where:

$P_{control/interface}$ $is\ the\ power\ required\ for\ receiving\ and\ processing\ information\ at\ controller$

$$P_{metasurface} = \sum^{M} \sum^{N} \sum^{L} P_{unit-cell}^{m,n,l}$$

$M\ =\ number\ of\ rows\ of\ unit\ cells$

$N\ =\ number\ of\ columns\ of\ unit\ cells$

$L = 1\ or\ 2, for\ single\ or\ dual\ polarization\ mode$

$$P_{unit-cell}^{m,n,l} = \sum^{(X_{m,n,l}-Y_{m,n,l})} P_{diode}^{ON}$$

$X_{m,n,l} = number\ of\ PIN\ diodes\ connected\ to\ unit\ cell\ in\ row\ "m", column\ "n"\ \&\ for\ polarization\ "l"$

$Y_{m,n,l} = number\ of\ PIN\ diodes\ connected\ to\ unit\ cell\ that\ have\ "OFF"\ state\ \&\ don't\ require\ power$

$X_{m,n,l} - Y_{m,n,l} = number\ of\ PIN\ diodes\ connected\ to\ unit\ cell\ that\ have\ "ON"\ state\ \&\ require\ power$

$P_{diode}^{ON} = power\ required\ for\ a\ PIN\ diode\ in\ "ON"\ state$

For RIS with other switching elements, the power consumption may be calculated differently, depending on the number of switching elements may be required for achieving same level of phase quantization.

Existing RIS prototypes are powered by traditional means such as the Mains electrical grid, Power over Ethernet (PoE) or Direct Current (DC). In general terms, the power consumption of RIS can be expressed as:

$$P_{RIS} = P_{MCU\_st} + N_t P_{UC\_st} + \frac{N_t E_{UC}}{T_{fr}}$$

where N_t is the number of unit cells, P_{MCU_st} is the static power consumption of the RIS controller, P_{UC_st} is the static power consumption of each unit cell, T_{fr} is the frame duration, and E_{UC} is the additional energy required to reconfigure each unit cell, which is assumed to be the same for all unit cells. This formulation shows that the rate at which RIS performs phase updates does not affect the power consumption.

The use of electrical grid or PoE restricts implementation of RISs only to areas with readily available electric power. Instead, alternative methods for power generation with EH elements placed directly on the metasurface have been proposed by a) integrating solar cells on RIS or b) recycling Radio Frequency (RF) energy as illustrated in Figure 4.6-1 and Figure 4.6-2.

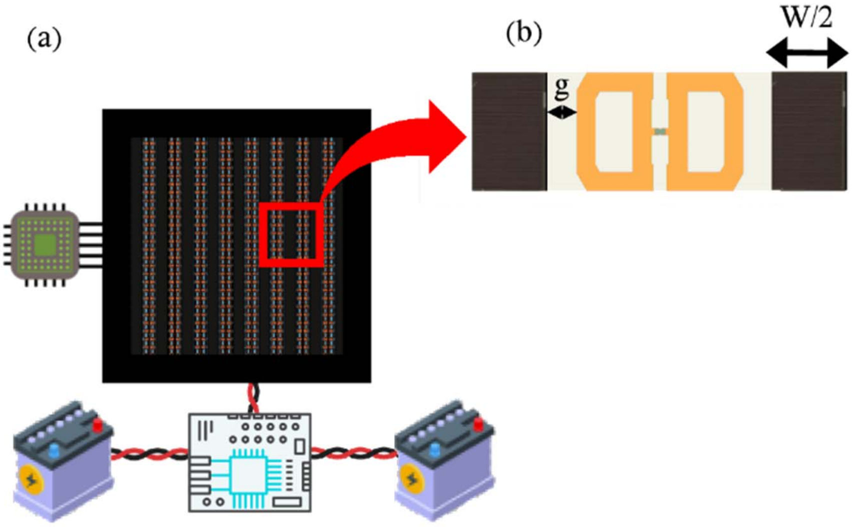

Figure 4.6-1: Integration of multi-junction solar cells on RIS operating in the FR1
a) A metasurface with interleaving solar cells and reflective unit cells
b) A unit cell with combined solar and RF elements, where W is the width of solar cell and g is the gap between solar cell and RF element

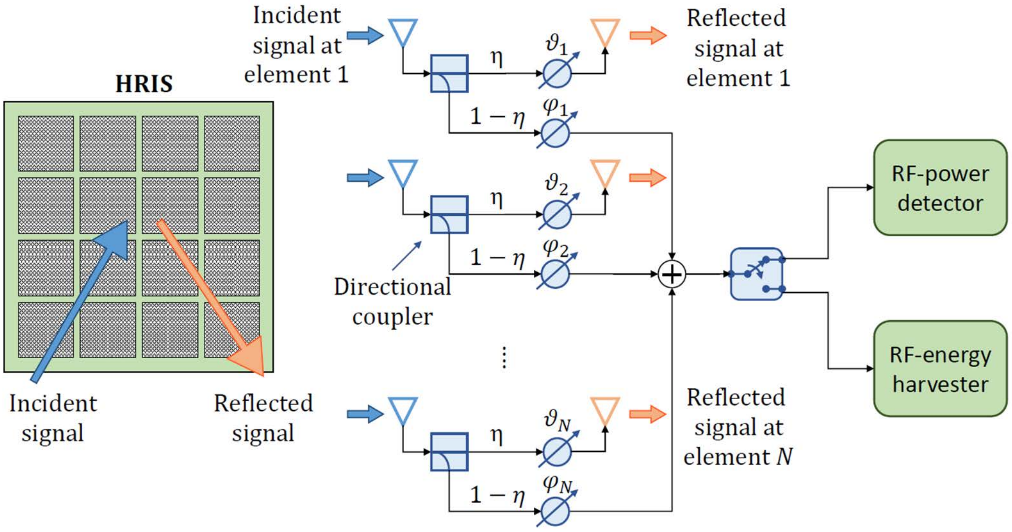

Figure 4.6-2: Integration of RF energy harvesting on RIS in a hybrid operation where a part of radio signal is absorbed to generate power and maintain the RIS operation

Energy harvesting can be performed separately from phase optimization and the amount of harvested energy in DC at a specific time slot can be expressed as:

$$P_{DC}(\mathrm{A}_h) = \frac{\frac{P_{max}}{1+e^{-a(P_{RF}(A_h)-b)}} - \frac{P_{max}}{1+e^{ab}}}{1-\frac{1}{1+e^{ab}}}$$

where $P_{RF}(A_h)$ is the harvested power that is received by the DC rectifier, P_{max} is a constant denoting the maximum harvested power when the harvesting circuit at the rectifier is saturated, and a, b are circuit-specific parameters, which are related to the resistance, capacitance, and turn-on voltage of the diode used for rectification. Experimental results in [i.8] show that up to 31,7 W of power can be generated with the configuration shown at Figure 4.5-1 on a 1,2 x 1,2 m RIS designed for 5G FR1 frequency band without increasing its size, while the measured power consumption of that RIS is just 3,6 W. Therefore, the harvested solar energy is sufficient to maintain RIS operation for 72 hours with a 252 Wh battery pack.

4.7 Design of RIS control circuit

4.7.0 Introduction

This clause will present different possible RIS layouts and control schemes, the design and fabrication of control board prototypes and briefly describe the current software and platform driving the RIS control.

4.7.1 General

The design of the RIS control circuit should consider:

a) the RIS itself, in terms of its physical layout and connection between tiles; and

b) the way data propagates between unit cells.

This physical disposition affects how data flows to the unit cells, and therefore how the software control should operate.

The software can be hosted in a microcontroller (MCU) or a Single-Board Computer (SBC). Its primary function is to compute phase patterns based on the desired reflection/transmission direction, and to drive the General Purpose Input Output (GPIO) pins that set the state of each unit cell or the control voltage level. The pin-driving method depends on the exact way in which each unit cell control is physically connected to the MCU or SBC. Besides this basic function, the MCU or SBC should allow the network developer a set of high-level methods for RIS control via one of the RIS interfacing methods described in clause 4.5 of the present document.

4.7.2 RIS serial communication control

Since controlling all unit cells in a RIS requires an immense amount of Input/Output (I/O) controls (even assuming 1 bit per unit cell, and a PIN diode-based design), the most straightforward manner to drive all control bits from one microcontroller is to resort to a chain (or chains) of shift-registers. Several variants of the propagation of the control flow can be designed, which are explained below.

The fully serial design shown in Figure 4.7.2-1 is the simplest. A tile of 8 x 8 unit cells is driven by one set of GPIO pins at the tile's periphery. The input pins are those required by the daisy chain of 8-bit Shift Registers (SRs), i.e. VDD, GND, a data clock and data line, and a *latch* signal.

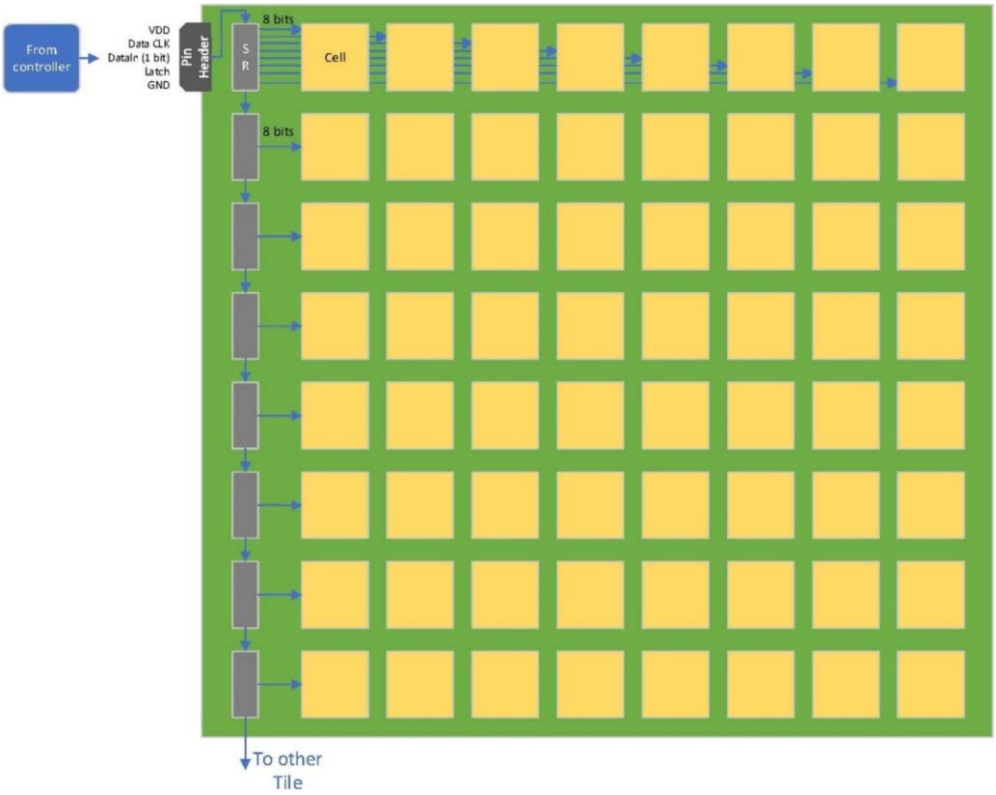

Figure 4.7.2-1: Full serial example assuming 1-bit PIN diode control per cell (details omitted for rows 2 to 8)

The shift-registers are 8-bit SIPO (serial-in-parallel-out) type. Eight clock cycles are required to shift 8 bits into a single SR, and only when the *latch* signal is asserted are those 8 bits driven to its parallel outputs. Thus, a single SR drives an entire row of 8 unit cells. Since SRs can be daisy chained, a long shift register of 64 bits is possible in a single tile. The end of the daisy chain may also connect to a following tile, making the design scalable.

This type of control (serial) requires only a Single Data Pin (SDA) and a Single Clock (SCK) GPIO pin from the microcontroller to command the Shift Registers (SR), thus making the circuit much simpler. However, despite the scalability, the time required to change the RIS configuration increases linearly with the RIS size, and the refresh rate may be, in general, slower than other configurations that feed control data in parallel. For a parallel control, more GPIOs and additional connections in the circuit are needed, making it slightly more complex. Two examples are shown below. However, this control scheme is apt for small RISs when a simple implementation is preferred.

4.7.3 RIS serial parallel communication control

Figure 4.7.3-1 shows an alternate "Row Parallel" configuration where each row of an 8x8 tile is connected to its own pin header, instead of having the SRs daisy chained. This design can provide a higher refresh rate than a fully serial solution, but only if the microcontroller can support N = 8 sets of I/O pins and drive them in parallel. Otherwise, the rows would be configured sequentially, leading to the same increase in refresh latency for larger designs. Given the requirement of a large number of I/O pins, devices like FPGAs are adequate for this purpose, especially since a hardware design can be deployed onto the FPGA to drive all the pin headers in true parallel.

This configuration requires that the software layer split the stream of control bits into the correct lanes, but also allows for a better physical distribution of the clock and latch signals, which otherwise suffer from a long route from the microcontroller output to all the SRs.

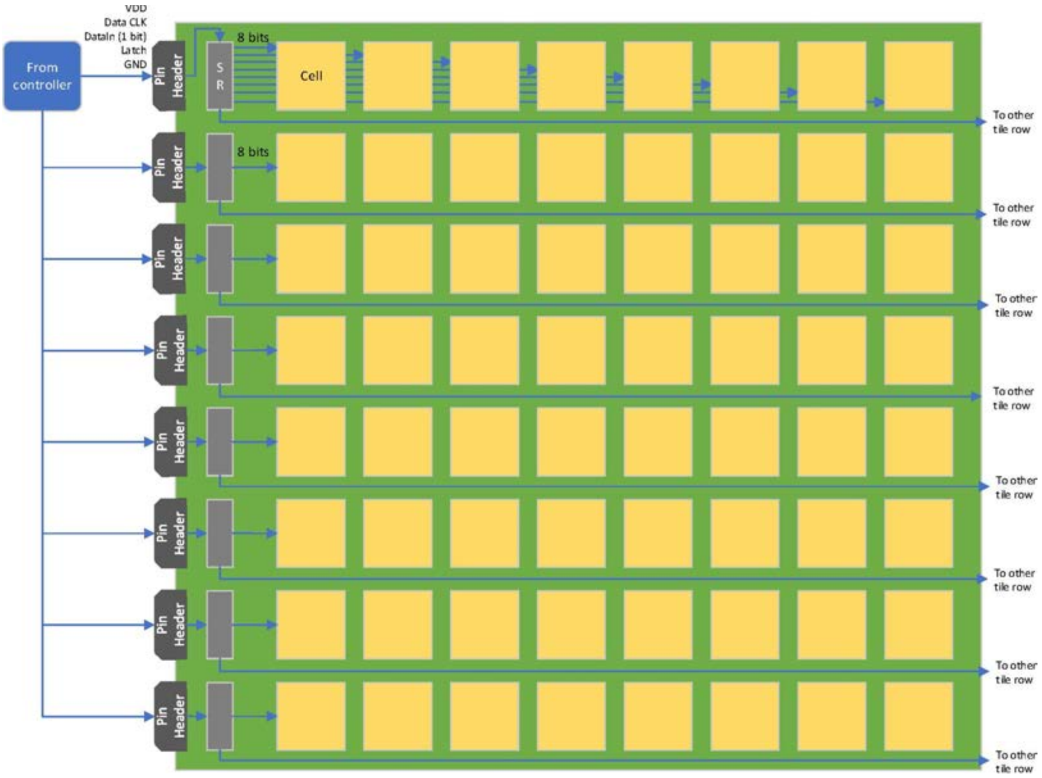

Figure 4.7.3-1: Row Parallel configuration with one data lane per row; SRs are not connected to each other but could propagate data to other tiles

Additionally, since the SRs are no longer daisy chained, each row can instead be connected to the input pin headers of an identical tile. This approach facilitates the control of a larger rectangular RIS, where the software merely controls a longer row of unit cells per lane. Adding rows can be achieved in two ways:

a) by using the same controller to drive another set of N pin headers (e.g. totalling 16 pin headers); or

b) use another controller to preserve modularity and scalability. This concept is illustrated in the next clause.

4.7.4 RIS multiple-tile control

Regardless of the tile-level architecture, control of a multi-tile setup can be implemented in several ways, depending on how data propagates between tiles, and how many controllers are used to drive each tile or set of tiles. Figure 4.7.4-1 shows two possibilities, considering the fully serial tile layout, and Figure 4.7.4-2 shows two possibilities considering the tile design with parallel pin headers.

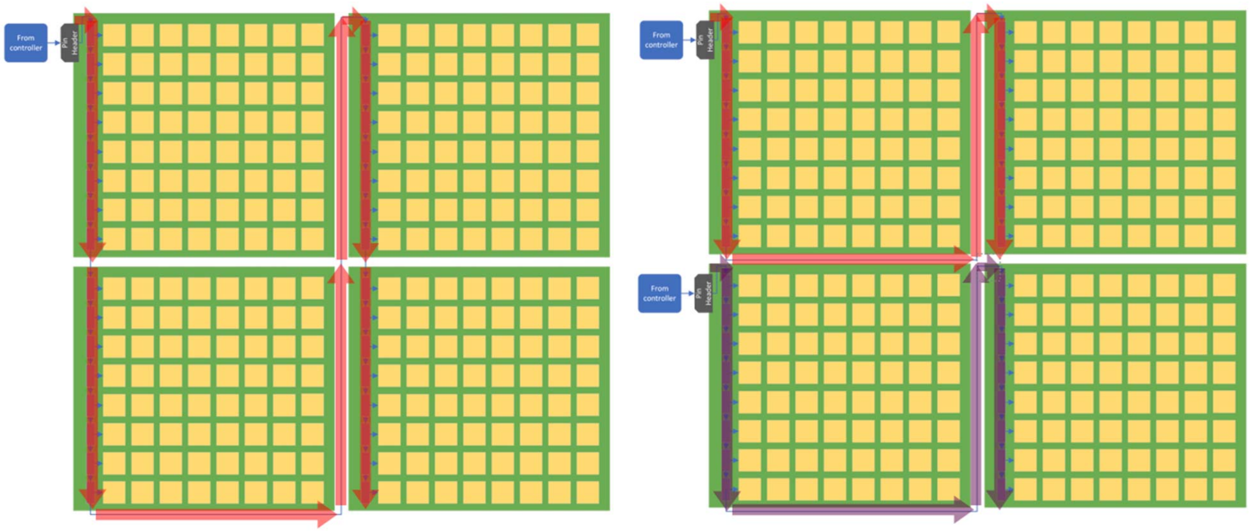

a) Tiles in full serial connection driven by a single controller.

b) Each full serial pair driven by one controller; a single controller could still be used, with enough I/O.

Figure 4.7.4-1: Possible inter-tile connections for a fully serial tile architecture (arrows show the direction of flow of control bits for the unit cells)

In Figure 4.7.4-1.a four tiles using the fully serial tile design are connected. This is the simplest regarding the control at the software level, as a single shift register daisy chain is used to set all 256 bits required for the four tiles. However, the previously mentioned refresh rate decrease, as well as the capacitive load for the latch and clock signals is more problematic. In Figure 4.7.4-1.b the problem is mitigated, by parallelizing two pairs of tiles using the same interconnection scheme between tiles. By adding more pairs of tiles in this way, larger RISs can be built at the cost of additional microcontrollers, and the need to orchestrate operation between microcontrollers.

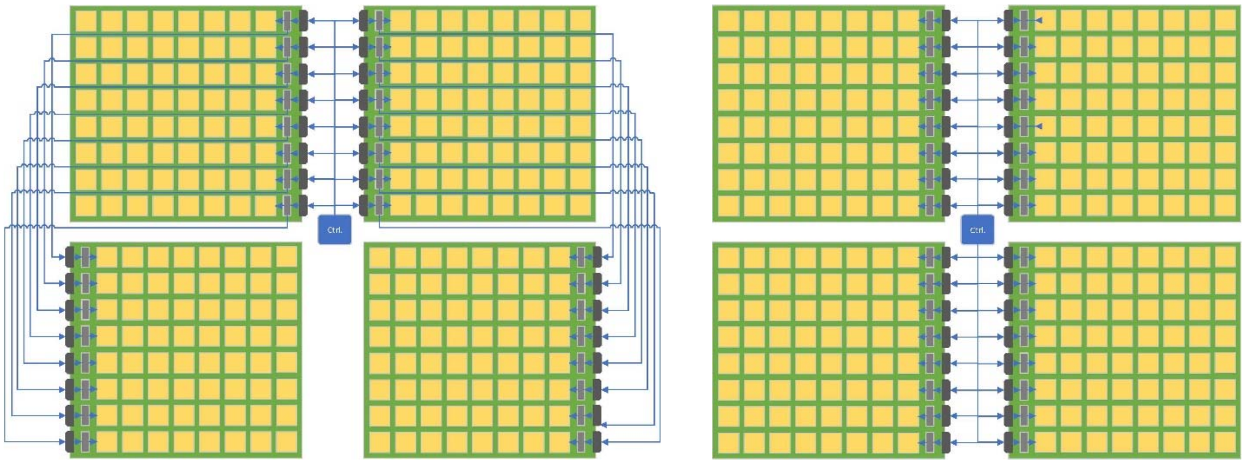

a) Two pairs in a series ("Serial Parallel"), driven by a single controller; two controllers could be used (one per pair).

b) One controller for four tiles in row parallel ("Row Parallel"); two per pair could be used, or one per tile.

Figure 4.7.4-2: Possible inter-tile connections for a "Row Parallel" tile architecture

In Figure 4.7.4-2, two alternatives analogous to Figure 4.7.4-1 are shown, based on the "Row Parallel" tile architecture. Both alternatives rely on a single controller, which controls either two rectangular RISs with longer rows (Figure 4.7.4-2a) or directly controls each tile at the cost of double the IO requirements (Figure 4.7.4-2b). Larger RISs can be built by either connecting more tiles in the series by resorting to more parallel connections or a combination of both.

However, even for a controller device capable of many GPIO outputs (such as an FPGA), it is not feasible to keep scaling the number of tiles (or unit cells) either due to this GPIO limitation or to other aspects mentioned before, such as the propagation of the clock and latch signals throughout all tiles. To address this, a hierarchical layout can help modularize the design and permit this scalability.

4.7.5 RIS multiple-tile hierarchical control

The amount of controllable elements in a single RIS is determined by the I/O capability of the chosen controller device. Scalability beyond this limit can be achieved by replicating this base design, as shown in Figure 4.7.5-1, where four groups of 4 tiles (16 x 16 unit cells per group for a global total of 32 x 32 unit cells) are each controlled by their own microcontroller (local controller). An additional central controller provides the previously mentioned orchestration between local controllers. Figure 4.7.5-1 shows a local control layout equivalent to Figure 4.7.4-2b as an example, but any layout could be supported, e.g. the fully serial 4 tile layout in Figure 4.7.4-2a.

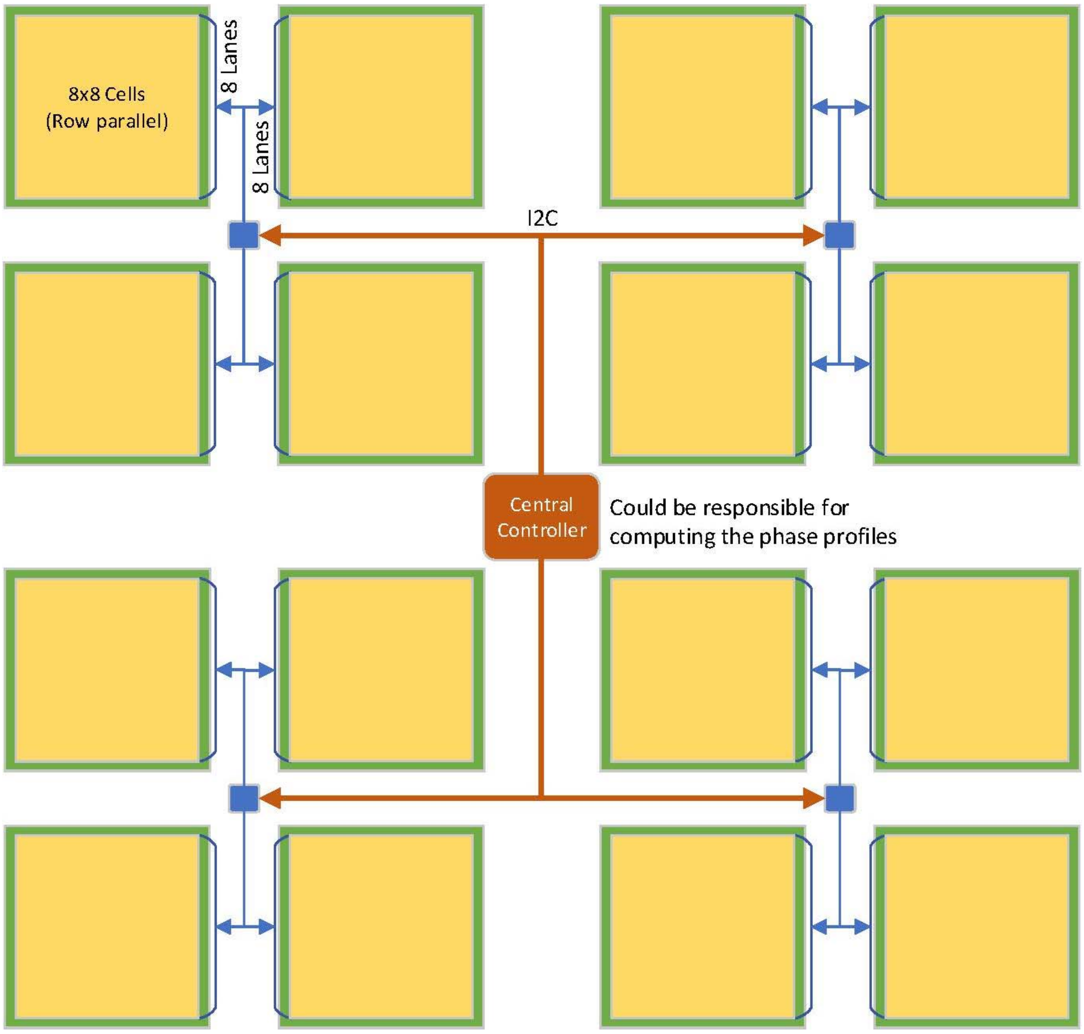

Figure 4.7.5-1: 32 x 32 RIS with 4 groups of 4 tiles. Each group is controlled by a single controller; each tile is configured in a "Row Parallel" configuration

The advantages of this layout include allowing for further scalability as mentioned, while separating the simpler low-level process of shifting bits to the unit cells from other higher level functions which can be supported by the central controller.

For instance, this central controller can be an SBC running an operating system, allowing for network access, a graphical interface to control the entire RIS assembly, or even re-programming all local controllers with any firmware updates. Furthermore, more demanding computations like phase pattern calculations, including experimental approaches, can be assigned to this central module.

The local controllers can instead host a simple protocol to provide low level features like responding to queries about the current configuration, configuring their entire tile group, or even only its own tiles. This can allow for several multi-beam configuration approaches. However, a synchronization mechanism needs to be introduced between groups of tiles.

For the central controller, the general requirements are persistent storage, ethernet or Wi-Fi access, Operating System (OS) capability, and capability to interface with the local controllers using SPI, I2C, or similar protocols. The local controller should have a small footprint, a sufficient number of I/O pins, and can be a bare-metal (no OS) device for faster response between a request from the central controller and a complete update of its tiles.

4.7.6 RIS transistor-based matrix control

As an alternative to SR-based control methods presented above, a transistor-based matrix control method can also used, depicted in Figure 4.7.6-1 illustrating a dynamic random memory access (DRAM)-inspired transistor matrix RIS, controlled by voltages in columns driven from a multi-channel Digital to Analogue Converter (DAC) and select signals in rows applied directly from the MCU or SBC. Each unit cell includes a holding charge capacitor beneath it, maintaining the applied voltage until updated. The application of a transistor matrix allows a dramatic reduction of control tracks. For example, a 30x30 RIS can be controlled with only 60 GPIOs (30 row select + 30 voltage select), instead of 900 GPIOs if using direct control.

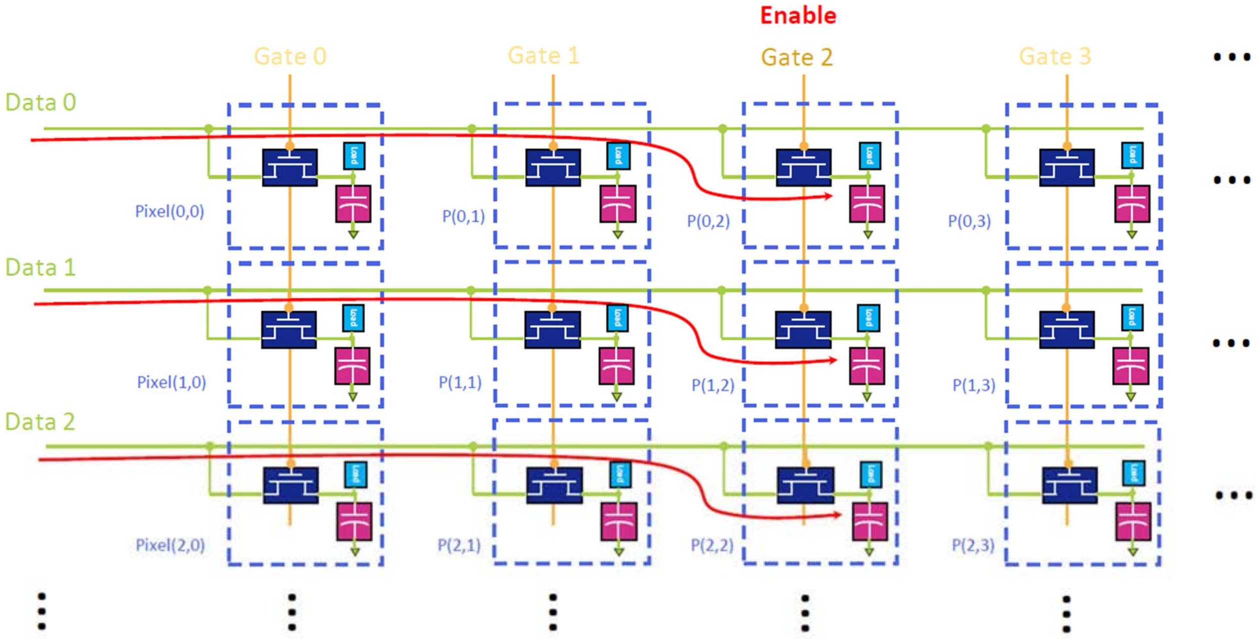

Figure 4.7.6-1: DRAM cell-inspired transistor matrix for RIS control

This method is particularly suitable for Liquid Crystal (LC)-based RISs that are fabricated by using a process similar to TFT displays. However, it can also be adapted for a varactor or a PIN diode-based RIS with a modification to the control circuit to accommodate conventional and readily available parts.

The key characteristic of this design is the RIS matrix update time, which is the time of the phase codebook update cycle. The cycle update time can be formulated as follows:

$$t_{cycle} = EEPROM_{read} + \sum_{r=1}^{R} t_{MCU} + t_{pd} + \sum_{c=1}^{C} t_{MCU} + t_{DAC} + t_{FET} + t_{pd}\ ,$$

where $EEPROM_{read}$ is the memory read time to extract a stored pattern that depends on the memory chip clock rate, R is the number of rows, C is the number of columns/voltages, t_{MCU} is the turn on/off time of the MCU or SBC, t_{FET} is the turn-on/off time of the Field Effect Transistor (FET), t_{DAC} is the DAC voltage set time for each column, which includes its serial control time and the buffering, and t_{pd} is the propagation delay on each PCB trace.

NOTE: t_{DAC} only applies to varactor or LC-based RISs.

It is also important to note that t_{cycle} should be longer than the capacitor charge time from V_{OFF} to V_{ON}, as otherwise, the capacitor may not be able to reach the required voltage level when the transition is sharp. Also, in this control method, the RIS unit cell update cycle is repeated continuously, unlike the conventional RIS designs that use set-and-forget architectures, which means that the RIS controller should be continuously running without interruptions.

5 Design requirements and practical implications for RIS types

5.1 General considerations including EE, EMF and coexistence

5.1.1 Regulatory requirements

From the hardware design perspective, RIS should comply with international standards for ElectroMagnetic Compatibility (EMC) and radio equipment regulations to be used in commercial and public settings, as summarized in Table 2 of ETSI GR RIS 002 [i.2]. These standards are designed to ensure that RIS does not emit excessive electromagnetic radiation that could interfere with other electronic devices or pose a health hazard to humans. Additionally, according to the Article 3.1a of Radio Equipment Directive (RED) 2014/53/EU, the electrical safety testing should be performed on all radio equipment regardless of operational voltage [i.5], which falls under EN IEC 62368-1 standard.

To assess the ElectroMagnetic Field (EMF) exposure limits compatibility of the RIS and to make its design compliant with the regulation standards, the following should be evaluated during the testing:

- Radiated emissions: This is the measurement of electromagnetic radiation that is emitted from the RIS. The level of radiated emissions should be below the limits specified in the applicable EMC standards for the operational environment.

- Spurious emissions: This is the measurement of electromagnetic emissions that may be unintentionally created by the RIS as a result of mutual coupling between transmit and receive radio signals on RIS, its Side Lobe Levels (SLL), and the carrier signal harmonics created by the structural resonance. The level of spurious emissions should be below the general case limits specified in Recommendation ITU-R SM.329 [i.13] as well as ERC 74-01 recommendations. Applicable product specific standards for passive RIS, active RIS and hybrid RIS should be determined per use case basis in accordance with RED 2014/53/EU.

- Specific Absorption Rate (SAR): This is the measurement of the rate at which electromagnetic energy is absorbed by the human body. The SAR should be assessed according to EN IEC 62311 standard, and the limit is 2.0 W/Kg in the EU/UK. The measurement of SAR is not required when RIS is placed > 20 cm away from human body or head during its normal operation.

It is important to ensure that practical RIS implementations comply with the regulatory EMC and radio standards for the following reasons:

- Improved safety: ensuring that the RIS does not emit excessive electromagnetic radiation that could pose a health hazard to humans.

- Reduced interference: reducing the risk of interference with other electronic devices.

- Increased compatibility: ensuring that RISs are compatible with a wider range of electronic devices and ready for integration into practical networks.

5.1.2 RIS bandwidth of influence

As per ETSI GR RIS 001 [i.1] clause 4.4.1 and ETSI GR RIS 003 [i.3] clause 6.7.1.3, an RIS has a working frequency bandwidth and a bandwidth of influence, with the bandwidth of influence being potentially larger than the working frequency bandwidth. To define practical requirements on the behaviour of RIS in the frequency domain, it is necessary to define and characterize this behaviour. For this purpose, the following concepts are introduced:

- Spectral Contrast in transmission (i.e. refraction).

- Minimum Spectral Mask in transmission (i.e. refraction).

- Maximum Spectral Mask in transmission (i.e. refraction).

- Spectral Contrast in reflection.

- Minimum Spectral Mask in reflection.
- Maximum Spectral Mask in reflection.

The spectral contrast in transmission (i.e. refraction) and in reception, $C^T(f)$ and $C^R(f)$, respectively, are functions of the frequency f, that quantify, to which extent, the RIS differs from a fixed surface, such as a wall or a window.

$C^T(f)$ and $C^R(f)$ have been defined and characterized for several prototypes of RIS in [i.4], with the following definitions:

$$C^T(f) = \max_{i,j \neq i \subset S} \left| S_{21}^i - S_{21}^j \right|,$$

$$C^R(f) = \max_{i,j \neq i \subset S} \left| S_{11}^i - S_{11}^j \right|,$$

where S is the set of states (this set can be discrete or continuous) of the unit-cell of the RIS (assuming that the RIS is a uniform set of unit cells). With these definitions $C^T(f)$ and $C^R(f)$ are lower-bounded by 0 and upper bounded by 2. When the contrast is close to 0, the RIS is close to a dumb surface. When the contrast is close to 2, the RIS is reconfigurable with the maximum possible contrast between two of its configurations.

By performing this analysis, it is possible to define a maximum spectral mask and a minimum spectral mask to set requirements on the contrast in reflection $C^R(f)$ and in transmission (i.e. refraction) $C^T(f)$, which will be shown in the following clauses.

5.1.3 Side Lobe Level (SLL) reduction techniques

The known approaches for RIS reflection coefficient design, such as using a DFT-based codebook often results in significant inter-beam interference due to the high Side Lobe Level (SLL). Indeed, using a DFT codebook leads to an SLL of around -13 dB. Hence, it is very important to consider methods for SLL reduction when associating RIS with wireless systems using spatial multiplexing as shown in Figure 5.1.3-1.

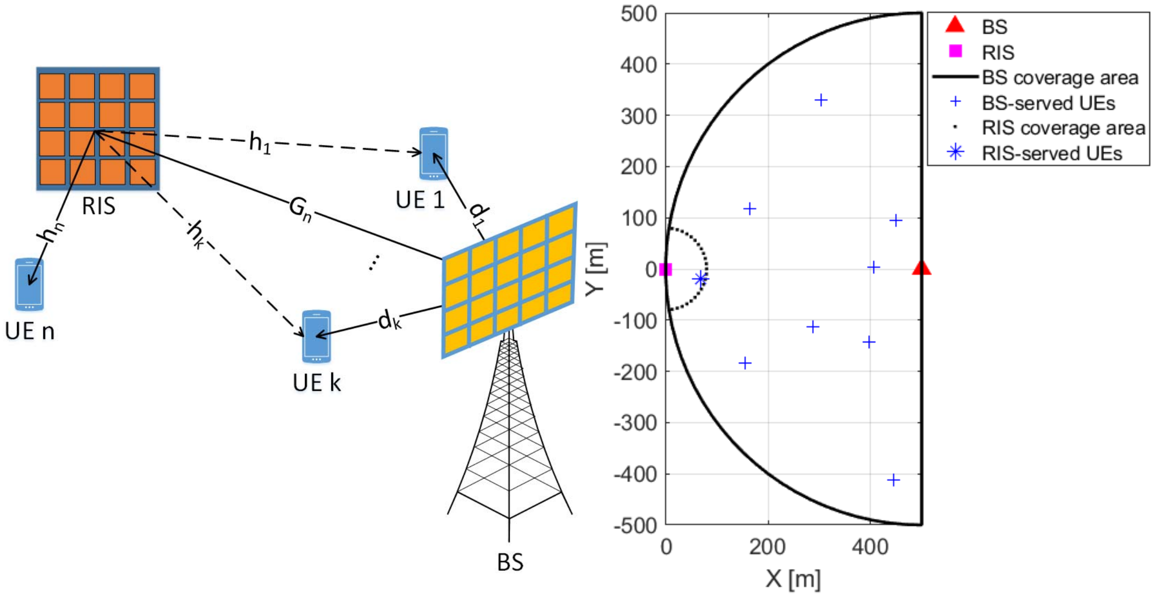

(a) (b)

Figure 5.1.3-1: Schematic representation of a RIS-assisted MU-MISO communication system: (a) Generic representation and (b) 2D depiction with real positions

One method for reducing RIS SLL, is to use amplitude tapering based on a known windowing function such as Chebyshev, Kaiser, etc. This alternative design has the potential to effectively reduce the SLLs, thereby significantly mitigating inter-beam interference while slightly reducing the Main Lobe Level (MLL) and widening its width. The implementation complexity of amplitude tapering remains relatively low, as the known window functions used for this purpose have a few, usually single, parameters to be adjusted.

To apply amplitude tapering, the RIS unit-element should allow for a separate control of the reflection magnitude and phase. This can be done, as described in [i.9], by loading the RIS element by both reactive and resistive loads as shown in Figure 5.1.3-2, maintaining a dual polarized operation. Then, Figure 5.1.3-3 shows reflection coefficients of these elements when fixing the resistor value to 0 Ω and varying the capacitance. Figure 5.1.3-4 shows reflection coefficients of these elements when fixing the capacitance to 0,8 pF and varying the resistor value. As can be seen, a quasi-independent control of the reflection magnitude and phase is achieved by respectively varying the resistor and the capacitor values.

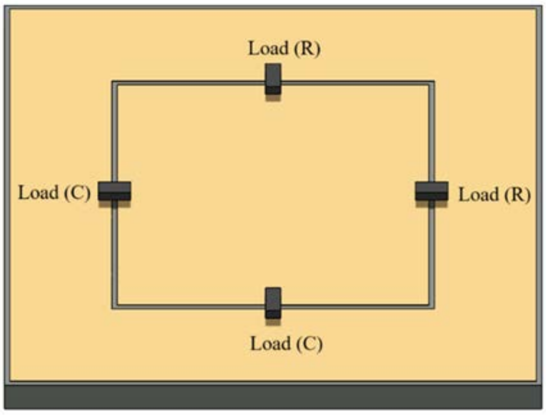

Figure 5.1.3-2: Example of a RIS element allowing separate control of the reflection phase and magnitude

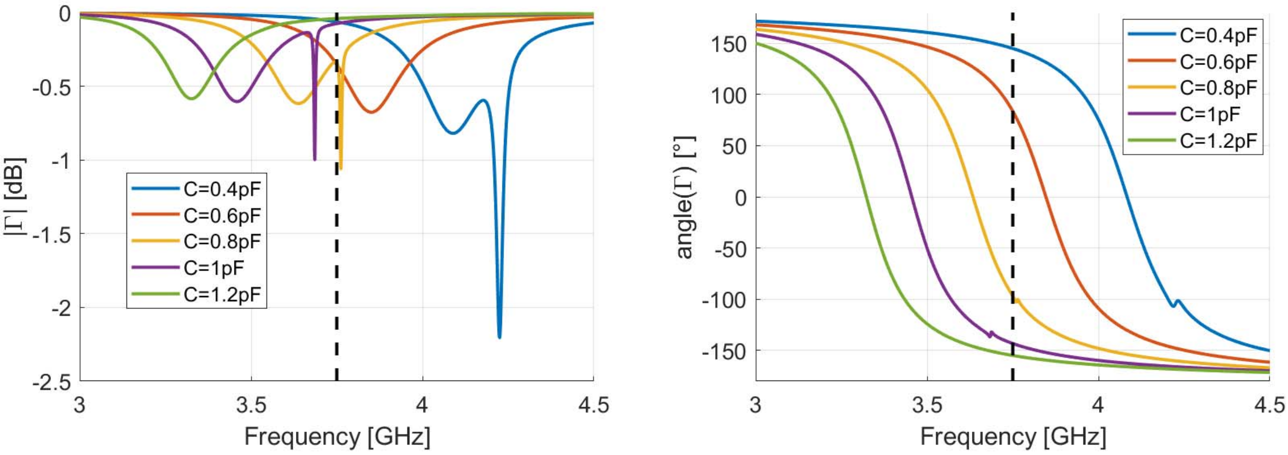

(a) (b)

Figure 5.1.3-3: RIS element's obtained reflection coefficient when setting R = 0 Ω varying the capacitance: (a) Reflection magnitude and (b) reflection phase

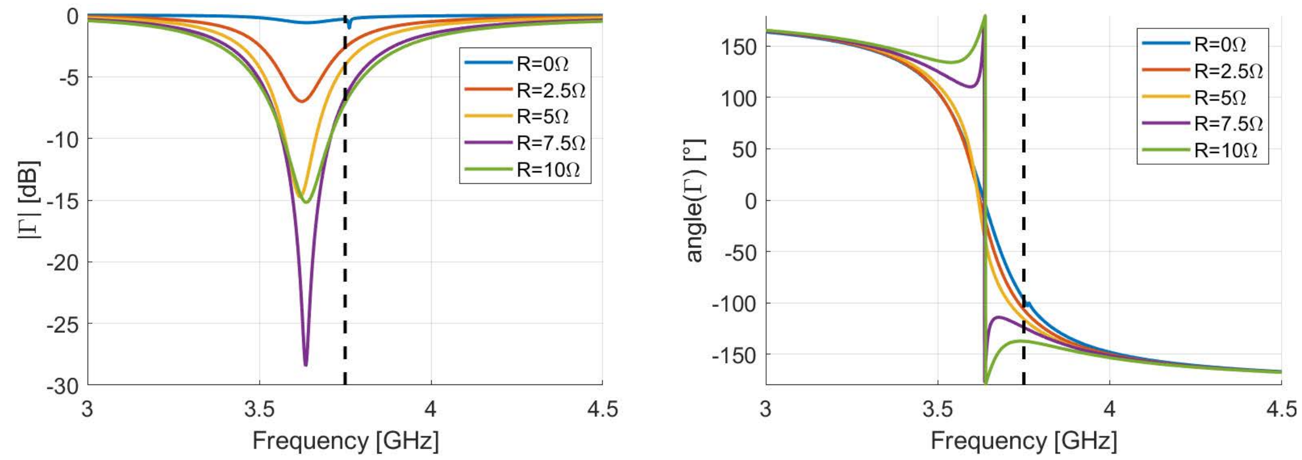

(a) (b)

Figure 5.1.3-4: RIS element's obtained reflection coefficient when setting C = 0,8 pF and varying the resistor; (a) Reflection magnitude and (b) reflection phase

Consider the scenario given in Figure 5.1.3-1 (b). Three cases are illustrated a) using DFT codebook with no windowing, b) using Chebyshev window with R=40, and c) using Kaiser window with β=5 to obtain an SLL of -40 dB in the last two cases. Figure 5.1.3-5 illustrates the RIS configuration amplitudes in the three approaches. As expected, the reflection amplitudes of the RIS elements are tapered to reduce the SLL. Figure 5.1.3-6 depicts the resulting RIS 3D normalized patterns (to have a maximum value of 0 dB) for the three aforementioned approaches. The data highlights that utilizing the windowing functions leads to a significant reduction of the SLL, while also causing a small degradation in the MLL and increases the main lobe Half Power Beamwidth (HPBW). Figure 5.1.3-7 displays the obtained sum rate in the three approaches. Unsurprisingly, when there are no users served by the BS, the absence of windowing yields the best performances. However, as the number of BS-served UEs increases, the importance of the filtering become more prominent to minimize the interference for all users.

To further analyze the impact of windowing, Figure 5.1.3-8 shows the rates of different users in a scenario involving eight BS-served UEs in three cases. As depicted in the windowing-free case, given in Figure 5.1.3-8 (a), UEs in close proximity to the BS exhibit higher rates compared to those situated at the cell edge. Also, as anticipated, UEs positioned at an equal distance from the BS show significantly lower rates when located within RIS sidelobes, in contrast to UEs situated within RIS nulls. This distinction is clearly observed through the alternating patterns of narrow red lines (representing the nulls) and wide green-yellow lines (representing the side lobes). Furthermore, the UEs located within the RIS main lobe experience the lowest data rates. Applying tapering to the reflection coefficient matrix Figure 5.1.3-8 (b), and Figure 5.1.3-8 (c), reduces the SLL. It also widens the main lobe while reducing its level. Consequently, the UEs positioned in the middle of the main lobe exhibit improved performance compared to their performance prior to tapering. However, some users who were originally close to the main lobe now find themselves within the widened main lobe, resulting in a decline in their performance.

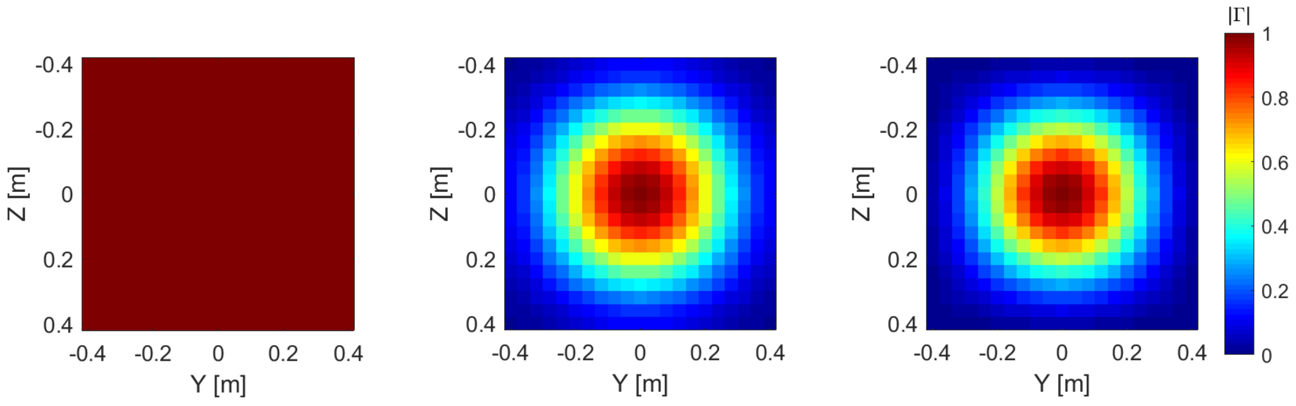

(a) (b) (c)

Figure 5.1.3-5: Required RIS reflection amplitudes in the three approaches: (a) None, (b) Chebyshev and (c) Kaiser

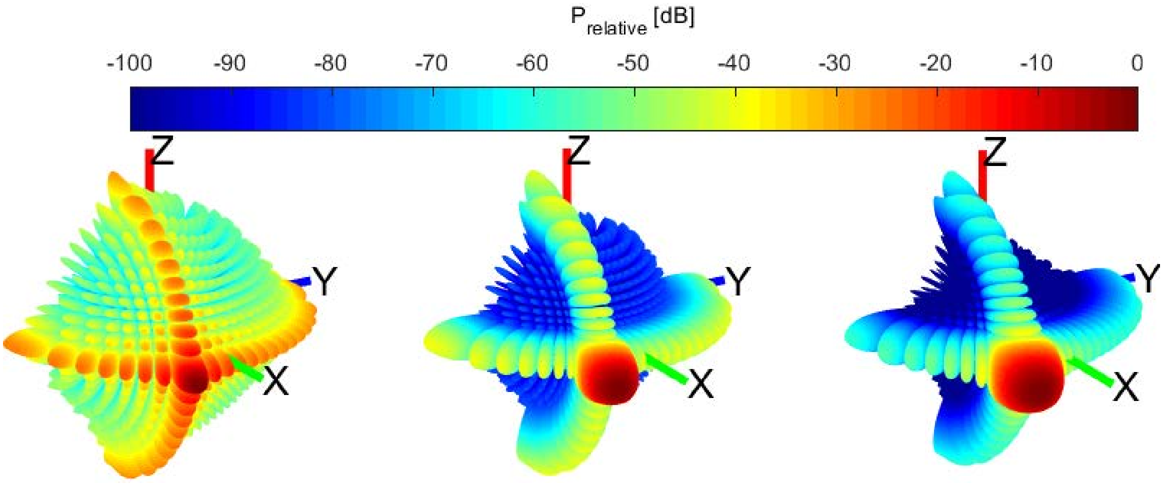

(a) (b) (c)

Figure 5.1.3-6: RIS 3D pattern in the three approaches: (a) None, (b) Chebyshev and (c) Kaiser

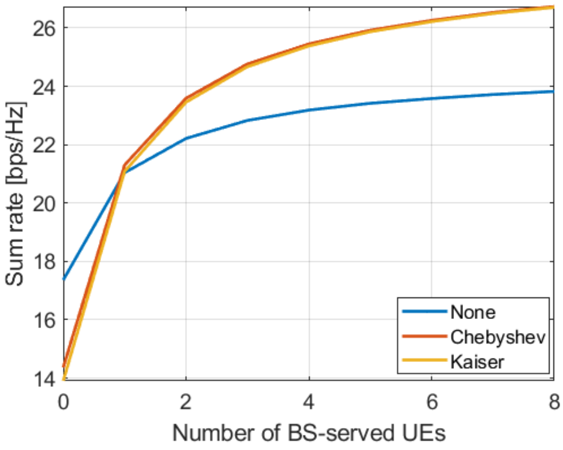

Figure 5.1.3-7: Sum rate as a function of the number of BS-served UEs

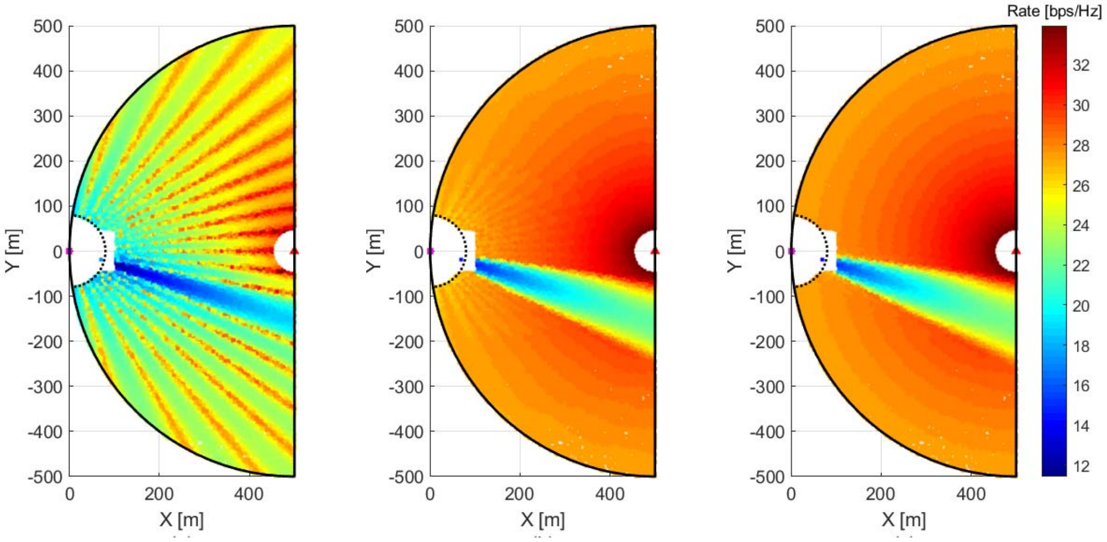

(a) (b) (c)

Figure 5.1.3-8: UE rate vs. position in the cell in the three approaches. (a) None, (b) Chebyshev and (c) Kaiser

5.2 Reflective RIS

The majority of RISs considered in the literature belong to the category of reflective RISs, which have the capability of reflecting incident EM waves toward reconfigurable angles that are different from the natural material's response. For example, a reflective RIS could be used to focus beams in a specific direction to cover a blind spot in network coverage. Alternatively, a reflective RIS could be used to create a diffused reflection pattern, boost the multi-path propagation, and allow a signal to be received from multiple directions simultaneously, therefore increasing the spatial diversity and multiplexing gains. Moreover, if the communication system is operating in an environment with a lot of interference, the RIS can be configured to reflect the incident waves in a way that minimizes the impact of the interference.

The dimensions and form factor of the unit cell are crucial considerations, particularly in applications with space constraints or where it is imperative for the RIS to remain inconspicuous. In theory, opting for a size less than $\lambda/2$ is advisable [i.10]; however, practical imperfections may render this choice suboptimal. For enhanced performance, it is recommended to choose a size even smaller than $\lambda/3$. To mitigate specular reflection mode, selecting super-small unit cells around $\lambda/8$ can be advantageous. Ideally, a reflective unit cell should efficiently reflect the entire incident wave without dissipation relative to the tuning factor. Also, it is desirable for the unit cell to offer a 360-degree reflection phase versus the tuning factor. For instance, in the scenario of two-bit coding, there are four distinct states evenly distributed across the $0–2\pi$ phase range represented by values {135, 45, -45, -135} degrees. They can be achieved with specific values of the capacitances or resistance. At the same time, the corresponding amplitudes should be high and quite uniform. However, it is unavoidable that certain values close to resonance frequency will be associated with smaller reflection amplitudes.

Ideally, a reflective unit cell should be homogeneous and independent of the incident angle. However, it is anticipated that the achieved reflection phase is contingent on the incident angle. This suggests that the selected tuning values may result in suboptimal reflection phases as the incidence angle varies. Having access to a distinct set of four phase states (in the case of two-bit coding) proves beneficial in maintaining excellent performance across different incidence angles [i.1]. This is illustrated in Figure 5.2-1, where the reflection phase is plotted against capacitance for incidence angles of 0,30 and 60 degrees, corresponding to TE and TM polarization, respectively. Selecting each time, the best four available states allows to retain almost perfect performance.

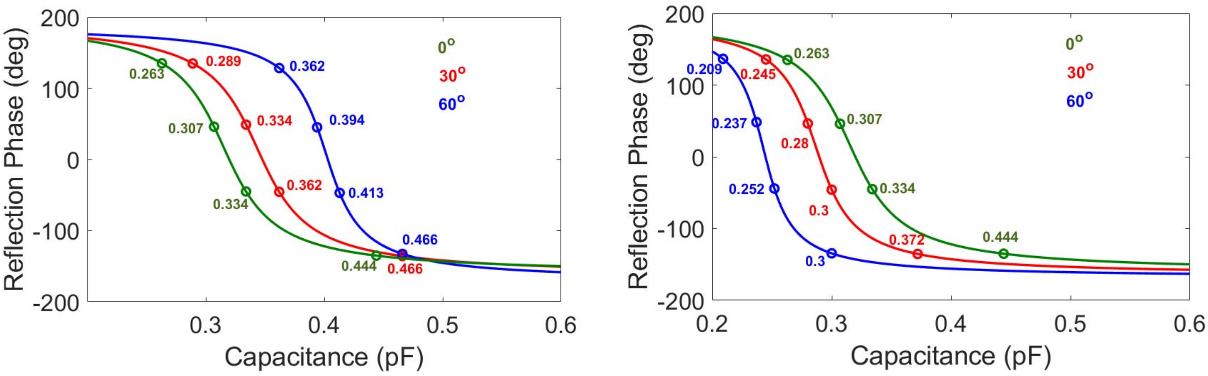

Figure 5.2-1: Reflection phase at 25 GHz for TE (left) and TM (right) polarization versus incidence angles 0, 30 and 60 degrees

With this technique it is possible to compensate the impact of incident angles to the phase reflection of the unit cell. Figures 5.2-2 and 5.2-3 show the reflection phase over the bandwidth of influence and compare the out of tune capacitances due to the impact of incident angle against 0,263 pF tuned for normal incident and the resulting compensation at 25 GHz for TE (with 0,289 and 0,362 pF, see Figure 5.2-1) and TM (with 0,245 and 0,209 pF, see Figure 5.2-1) polarizations.

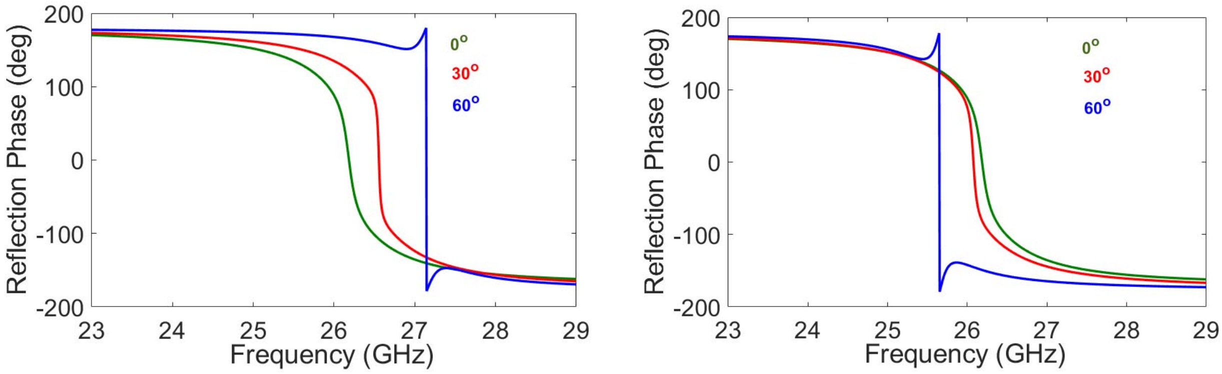

Figure 5.2-2: Reflection phase for TE polarization versus incidence angles 0, 30 and 60 degrees

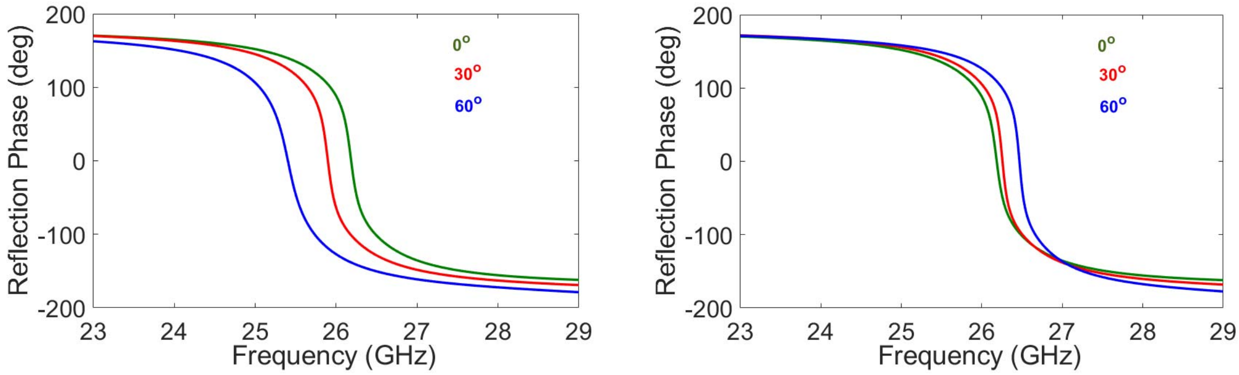

NOTE: The left figure shows the capacitance tuned (0,263 pF) for normal incident in both TE and TM polarization cases untuned with oblique incident angles, while the right figure shows the compensated misalignment with modified tuning 0,289pF and 0,362 pF corresponds to 30 and 60 incident angles.

Figure 5.2-3: Reflection phase for TM polarization versus incidence angles 0, 30 and 60 degrees

The spectral contrast shows how an RIS is different from a fixed surface (perfect reflector) and compared for TE and TM polarization versus incidence angles 0,30 and 60 degrees (see Figure 5.2-4).

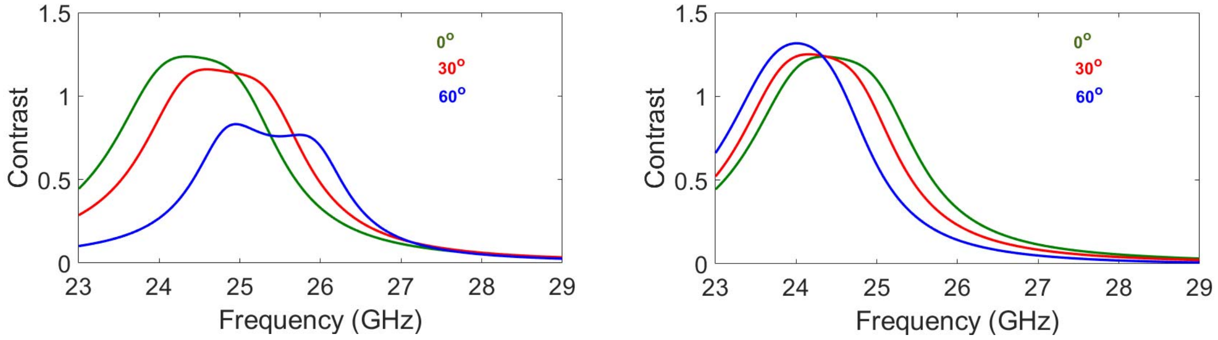

Figure 5.2-4: Comparison of contrast for TE (left) and TM (right) polarization versus incidence angles 0, 30 and 60 degrees

Furthermore, Figure 5.2-5 illustrates an example of spectral contrast and masks for a reflective RIS. The contrast in reflection is required to be:

- higher than 1 in the working frequency bandwidth;
- lower than 1 out of the bandwidth of influence.

The contrast in transmission (refraction) is required to be very low at all frequencies.

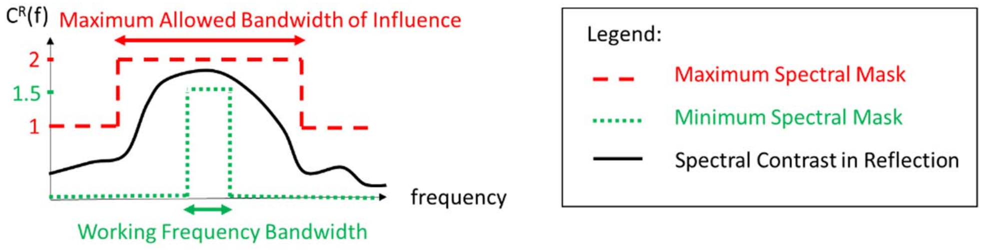

a) Spectral Contrast and Spectral Masks in Reflection

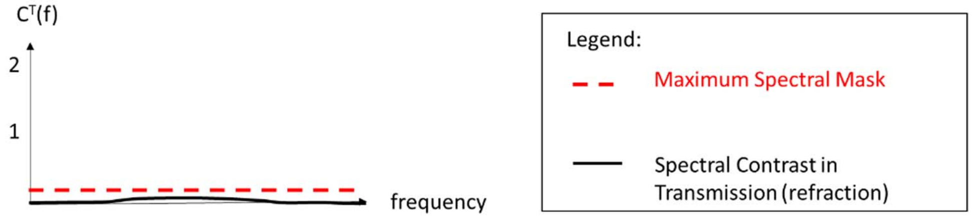

b) Spectral Contrast and Spectral Masks in Transmission (refraction)

Figure 5.2-5: Example of Spectral Contrast and Masks, in reflection (a) and transmission (b), for a reflective RIS

5.3 Refractive/Transmissive RIS

This category is the reverse of the reflective RIS and exploits the modified Snell's law of refraction, where the metasurface, instead of reflecting the EM waves to a specific direction outwards, refracts them inwards. Refractive RIS can also be referred to as Transmissive RIS, and in the context of the present document these terms are used interchangeably. Similarly to a reflective RIS, the dynamic control of the refraction angle can be achieved with active switching elements. For example, refractive RISs can be implemented on transparent structures, such as glass. An illustration of a practical refractive/transmissive RIS with dynamic control is shown in Figure 5.3-1 and described in [i.22]. Such structures can then be installed in buildings or on moving vehicles in public transportation systems to boost outdoor-to-indoor signal transfer.

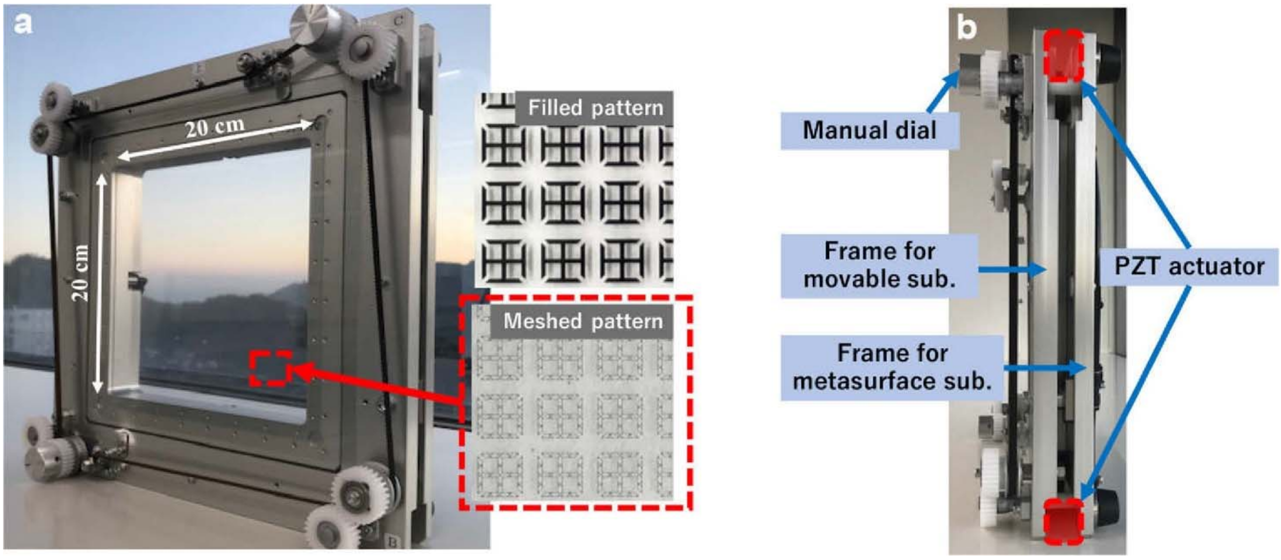

Figure 5.3-1: Transparent refractive RIS on glass with dynamic control [i.22]

Similarly to the previous clause, Figure 5.3-2 illustrates an example of spectral contrast and masks for a refractive/transmissive RIS. The contrast in refraction/transmission is required to be:

- higher than 1 in the working frequency bandwidth;
- lower than 1 out of the bandwidth of influence.

The contrast in reflection is required to be very low at all frequencies.

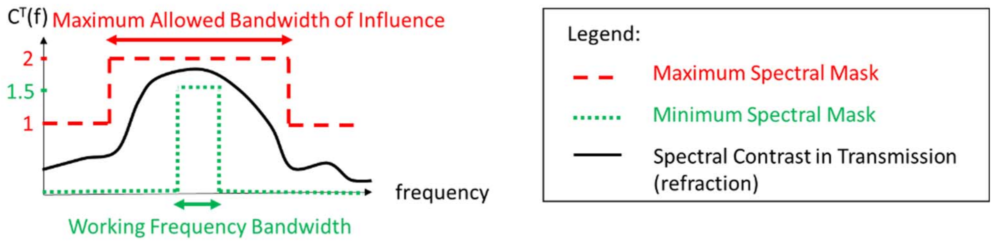

a) Spectral Contrast and Spectral Masks in Transmission (refraction)

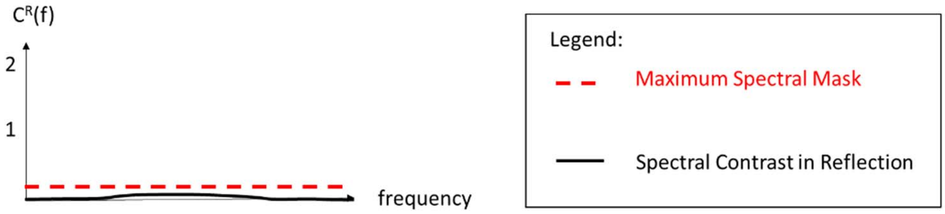

b) Spectral Contrast and Spectral Masks in Reflection

Figure 5.3-2: Example of Spectral Contrast and Masks, in reflection (a) and transmission (b), for a transmissive RIS

5.4 Absorptive RIS

Unlike reflective RIS or refractive RIS that can only adjust the phase of impinging radio waves, an Absorptive RIS (ARIS) relates to both phase and amplitude manipulation by absorbing a portion of the signal energy, which allows programmable control of the absorption. For example, ARIS can be programmed to absorb impinging radio waves only at a specific angle, while allowing radio waves impinging from other angles to propagate unaffected.

These advantages are well suited for applications where interference mitigation or enhancement are critical factors. For most of the RIS applications, where maximizing sum rate is the primary objective, using an RIS to absorb energy rather than increase signal power may seem counterintuitive. However, for applications where interference suppression or enhancing the secrecy of a given transmission is paramount, selective spatial absorption of the wavefield can be beneficial. As a trivial example, it may be desirable to completely absorb energy from strong interfering sources rather than further propagating their energy in the environment, or to suppress reflections of sensitive information in the direction of a potential eavesdropper. Consider a communication system illustrated on Figure 5.4-1, which consists of one BS (Alice), one legitimate user (Bob), one eavesdropper (Eve), and one ARIS and an additional antenna is deployed near Bob for the transmission of a jamming signal.

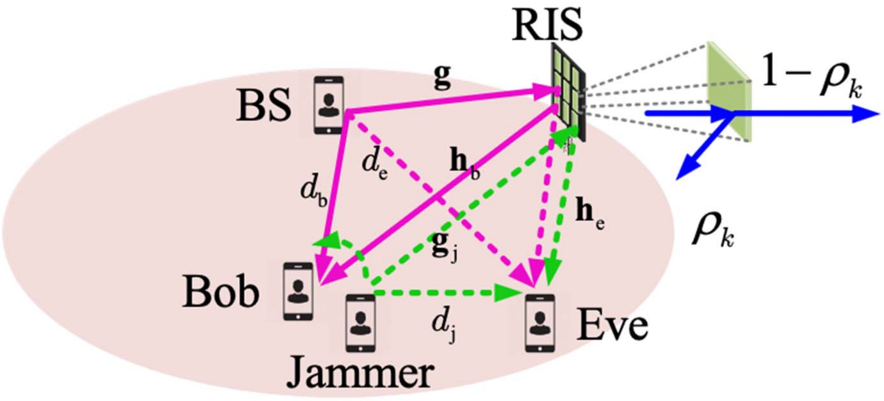

Figure 5.4-1: ARES-assisted communication system example

Figure 5.4-2 shows Performance of ARIS in the interference suppression application under various strengths of the direct channel between the Jammer and Eve. For a weak Jammer channel, the ARIS is the key to providing increased secrecy compared with the case of a conventional RIS As the strength of the Jammer channel increases, the impact of the Jammer becomes larger than that of the RIS, and the ARIS and conventional RIS converge to the same performance. An example of an algorithm for ARES phase configuration is considered in [i.11].

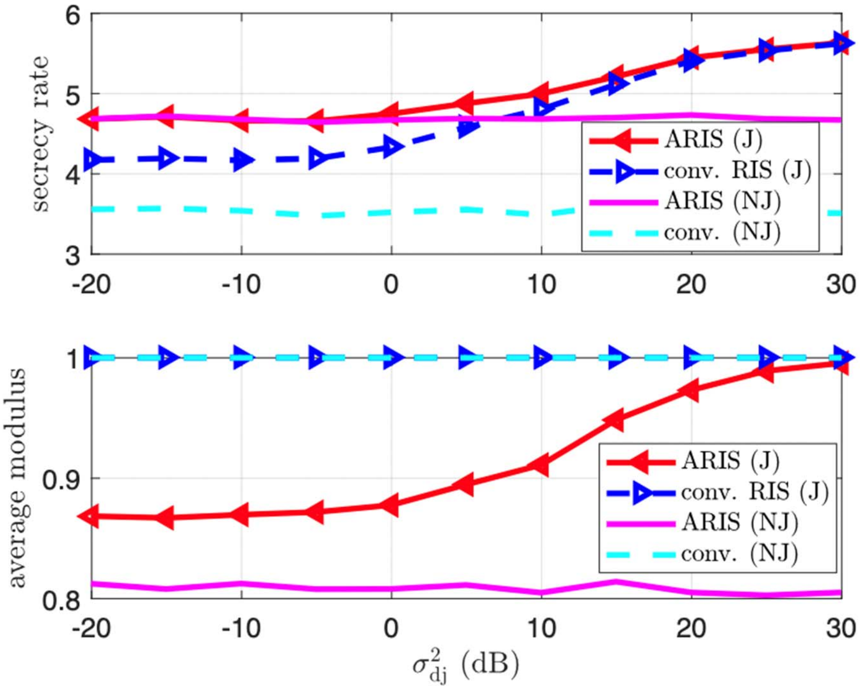

Figure 5.4-2: ARES (J) and conv. RIS (J) indicate performance with jamming antenna, where ARIS (NJ) and conv. (NJ) indicated performance without jamming antenna

ARIS architecture can be achieved by several means, for example by adding a variable resistive element to terminate the radial waveguide stub that might otherwise be used for power detection or sampling or placed in parallel with a varactor diode at each RIS element. The ARES performance is evaluated in Figure 5.4-3, where the refection coefficient is plotted for various angles of incidence as a function of frequency, considering the optimum resistive load for each case. At a normal incidence the refection coefficient is less than -50 dB. This degrades as the angle of incidence increases, as shown in Figure 5.4-3 (a) for TE polarization. However, it remains below -30 dB for incident angles up to 45 degrees. Similar behaviour is found for the TM polarization, depicted in Figure 5.4-3 (b). The refection coefficient at 5 GHz remains below -20 dB up to 25 degrees.

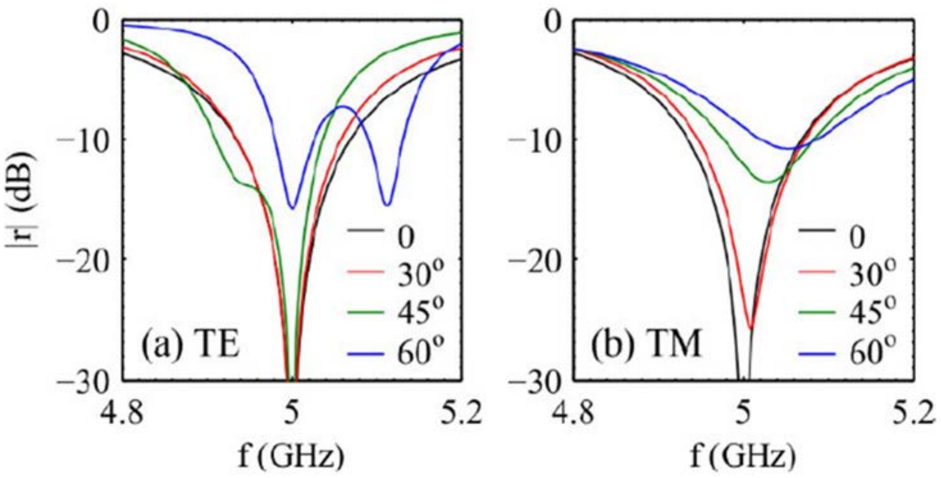

Figure 5.4-3: Reflection spectra for optimal RC values within the range provided by the ARES, for oblique incidence at the (a) TE and (b) TM polarizations

5.5 STAR-RIS

Simultaneous transmit and receive (STAR)-RIS is a combination of reflective and refractive RIS as illustrated in Figure 5.5-1. In this case, both transmission and reflection functions are integrated to offer the capability of manipulating the EM waves towards the 360° direction of interest without the blind zone. STAR-RIS can be designed in such a way as to have reflective properties in one frequency band and refractive properties in another. This is possible due to the application of holographic theory for metasurface design, where small unit cells can form larger unit cells and therefore have a different response at a different frequency. In an indoor-to-outdoor communication scenario, radio signals can be reflected and scattered inside the building at one frequency and transmitted out of the building at a different one. In other scenarios signals in different frequency bands can be reflected or refracted in different ways based on requirements.

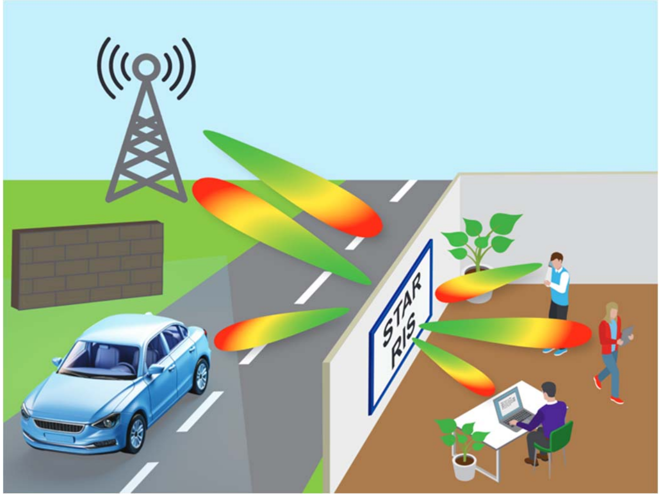

Figure 5.5-1: STAR-RIS indoor to outdoor communication scenario

Since each STAR-RIS element can be adaptively turned in pure transmission or pure reflection mode, the resulting adjustable aperture size of STAR-RIS will artificially control the near/far-field signal range and thus achieve the different beam pattern feature, e.g. beamsteering on the left side versus beamfocusing on the right side. This is shown in Figure 5.5-2.

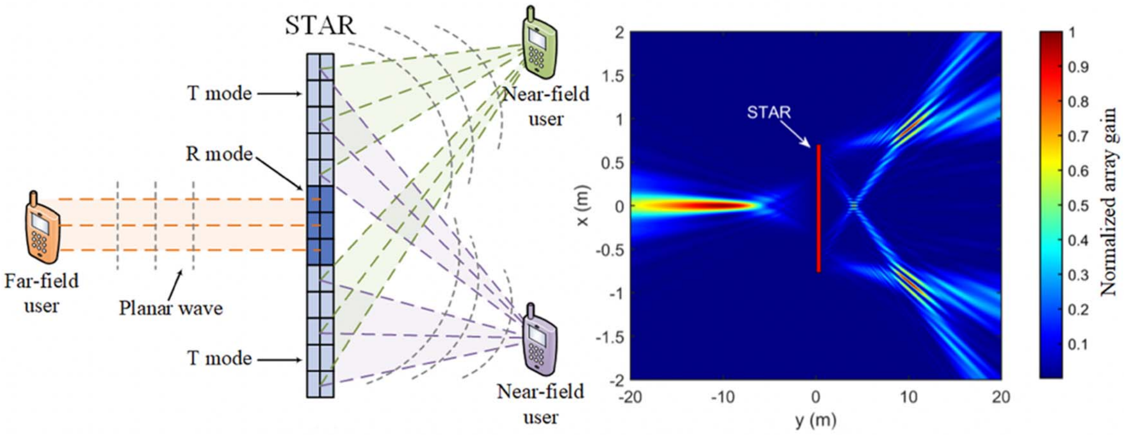

Figure 5.5-2: STAR-RIS aided near field/far field communication in transmissive (T) and reflective (R) modes

Additionally, polarization control of reflected and refracted waves can allow STAR-RIS to improve the energy efficiency losses caused by focusing all energy on a single refracting direction. This functionality allows to effectively split the incident spherical wavefront in two, and control transmissive and reflective waves independently with minimal energy efficiency losses. An example of a STAR-RIS unit cell is illustrated in Figure 5.5-3 and its amplitude and phase characteristics are illustrated in Figure 5.5-4.

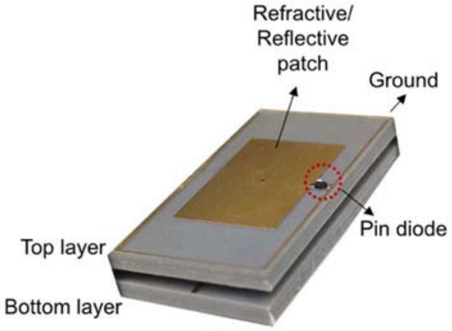

Figure 5.5-3: STAR-RIS unit cell prototype designed for 3,5 GHz [i.12]

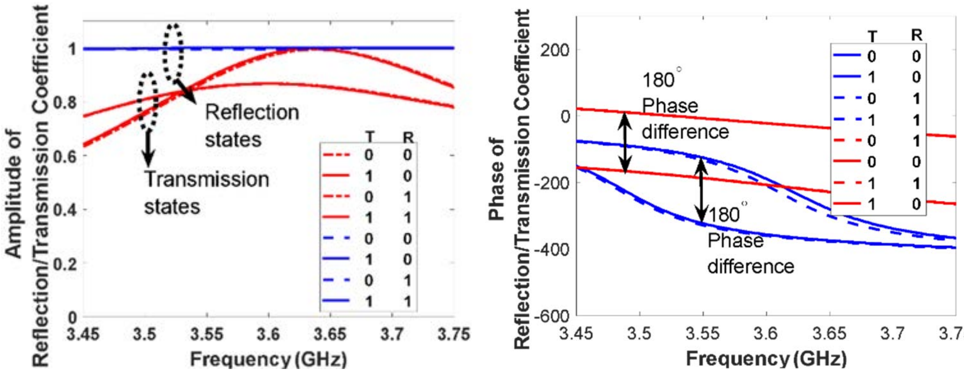

Figure 5.5-4: STAR-RIS unit cell simulation results show a) amplitude b) phase

To accomplish STAR-RIS beamforming there are two approaches: the optimization-based approach and the codebook-based approach. For the optimization-based approach, an element-wise STAR beamforming is performed, where the transmissive and reflective beamforming coefficients are optimized one by one. To simplify this method, beamforming coefficients can be grouped into tiles for optimization with the aid of successive convex approximation, monotonic optimization, and machine learning tools. In the codebook-based approach, specific codebooks are developed consisting of several pre-designed STAR-RIS beamforming vectors, which significantly reduces the complexity of the algorithm.

Detailed information about signal and channel models as well as the beamforming optimization of STAR-RIS is considered in clause 5 of ETSI GR RIS 006 [i.14].

5.6 Multi-functional RIS

Multi-functional RIS provides diversity of smart radio environment such as reconfigurable reflection, reconfigurable refraction, and absorption of impinging signal. A key consideration of designing multi-functional RIS element is using at least two tunable components (PIN or Varactor diodes) on a unit cell with defined states. In Figure 5.6-1(a) a design of multi-functional RIS that functions as switchable reflection and absorption is illustrated with two PIN diodes used for two-bit control and placed onto the unit cell. Two-bit control states with an ideal S-parameter (S_{11}) are defined in Table 5.6-1. The use of PIN diodes, noted D_1 and D_2, is dependent on functional modes, which are enabled via points V_1 and V_2, respectively.

Table 5.6-1: Two-bit control for use of multi-function RIS that functions as switchable reflection and absorption

Mode	State	Diode State		S-parameter	
		D_1	D_2	$\lvert S_{11}\rvert$	$\angle S11$
1-bit Reflection	R1	OFF	OFF	0 dB	0°
	R2	ON	OFF	0 dB	180°
Absorption	A1	ON	ON	$-\infty$ dB	
Not used		OFF	ON		

From Table 5.6-1, for 1-bit reflection mode which is enabled via point V_1, D_2 is switched OFF. Then, D_1 is used for controllable reflection phase states of 0° (D_1 is OFF, R1 state) and 180° (D_1 is ON, R2 state) with ideally full reflection ($|S_{11}|=0$ dB). The simulated results for reflection mode are shown in Figure 5.6-2. The phase bandwidth of 120 MHz (5,78 to 5,90 GHz) is defined as phase difference of 180° ± 20° between phases in ON and OFF states.

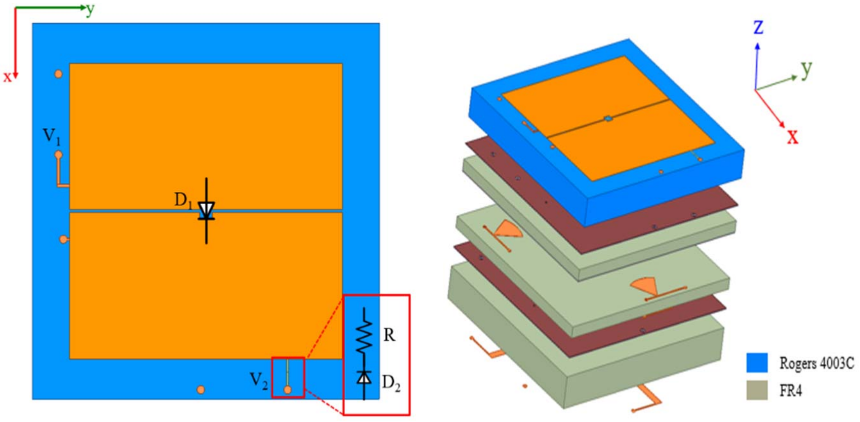

(a) (b)

NOTE: To realize good performance of absorption, resistor R is also considered, where Figure 5.6-1 (a) shows the top view of the element, and Figure 5.6-1 (b) shows the layered configuration including biasing design.

Figure 5.6-1: Example of multi-functional RIS element operating at 5,8 GHz that functions as switchable reflection and absorption using two PIN diodes (D_1 and D_2)

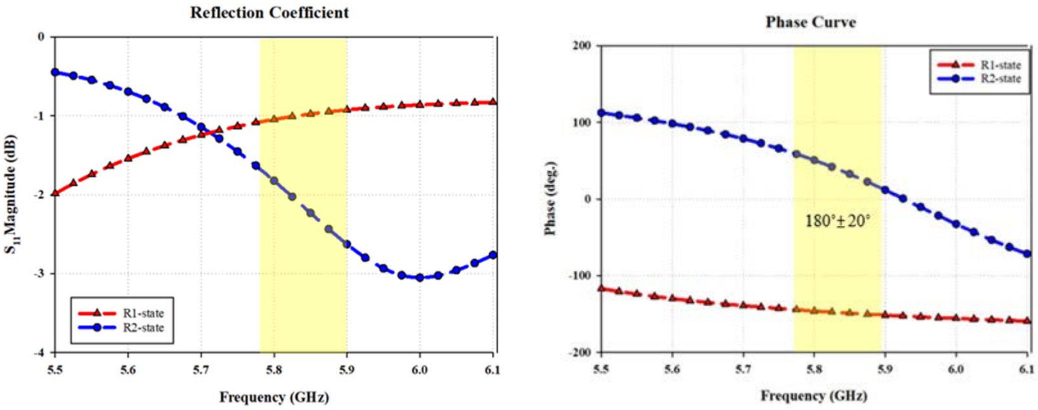

(a) (b)

NOTE: Red line shows the R1 state with 0° phase state (D_1 is OFF), blue line shows the R2 state with 180° phase state (D_1 is ON).

Figure 5.6-2: Simulated results for reflection mode (D_2 is switched OFF, D_1 is switched ON/OFF). (a) Reflection coefficient, (b) reflection phases with defined phase bandwidth of 120 MHz for phase difference 180° ±20°

For absorption mode, which is enabled via V_1 and V_2 for respectively biasing D_1 and D_2, D_1 is kept switched ON; D_2 is switched ON for full dissipation of impinging signal which means that $|S_{11}|$ is negative infinity and the phase is not needed to be considered. To evaluate the quality of absorption, absorptivity is defined as $1-\left|S_{11}\right|^2$ and it is unity for full absorption. Besides D_2, for the realization of good performance of absorption, resister R is considered to dissipate more impinging signal power. As such, reflection coefficient is reduced, and absorptivity is increased. The performance of reflection in absorption mode, for various R selection, is simulated as shown in Figure 5.6-3. As a result, the reflection coefficients are reduced with low resistance. The figure shows that the case of R = 33 Ω has the best absorptivity of more than 90 % within 5,80 to 6,05 GHz.

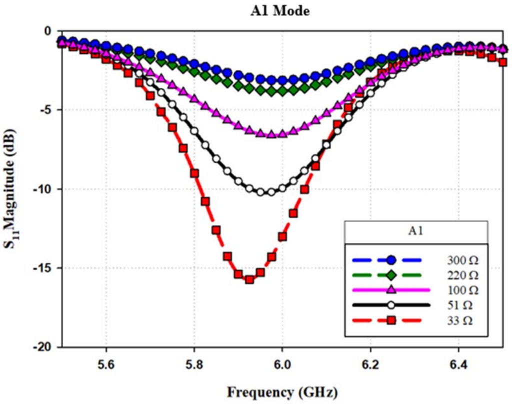

Figure 5.6-3: Simulated result for absorption mode (D_1 and D_2 are ON)

6 RIS prototypes, trials and measurements

6.1 Evaluation of spectral contrast in RIS prototypes

Figure 6.1-1 illustrates the contrast for 4 different existing RIS prototypes [i.4], as a function of the normalized frequency $\bar{f} = f/f_0$ (where f_0 is the central frequency, defined as the middle between the lowest and the highest frequencies at which the contrast equals 1):

- The contrast in reflection $C^R(\bar{f})$ for a varactor-based reflective RIS (R-RIS), with continuous phase shifting, at 5,8 GHz.
- The contrast in transmission $C^T(\bar{f})$ for a PIN-diode transmissionve RIS (T-RIS) at 27 GHz.
- The contrast in reflection $C^R(\bar{f})$ for a Pin Diode-based R-RIS, with discrete phase shifting, at 5,3 GHz.
- The contrast in reflection $C^R(\bar{f})$ for a RF switched-based R-RIS, with discrete phase shifting, at 5,2 GHz.

The normalized frequency is chosen instead of the plain frequency to plot contrasts of RIS operating at mmwaves and sub-6 GHz frequencies on the same figure.

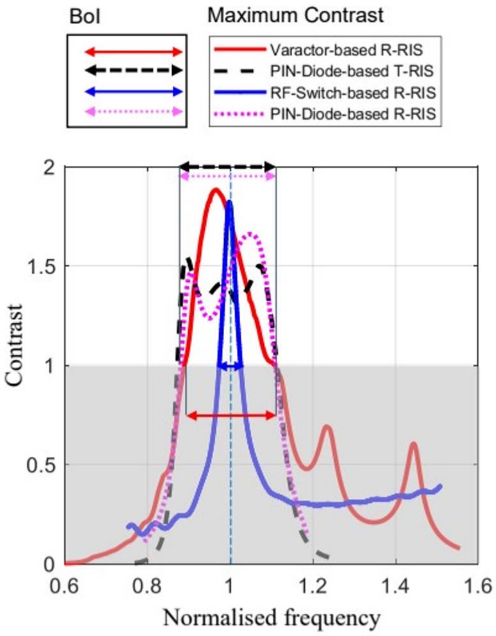

Figure 6.1-1: Extracted from [i.4], spectral contrasts for 4 different RIS prototypes

6.2 Trial results in typical deployment scenarios

One of the ISG members reported the following trial results obtained using an RIS prototype they manufactured. The trials were conducted in many different environments, with details below, and can be found in [i.15]. Before conducting field trials in practical environments, the RIS prototypes are tested in an RF anechoic chamber to ensure that the prototypes are able to perform according to the theoretical values calculated from selected codewords.

- **Indoor:** The test environment for the indoor test is shown in Figure 6.2-1, where the BS is placed at one end of the corridor, the RIS is placed in front of the door of one room and the UE is in that room. The distance between the BS and the RIS is approximately 20 meters and the distance between the RIS and the UE is around 10 meters. There is no LOS path between the UE and the BS. The test is conducted with a 1-bit single-polarized panel and a 4-bit dual-polarized panel. Both panels have 64 × 64 elements.

The working frequency is 26 GHz. It is observed that the 1-bit single-polarized RIS provides around 30 dB gain in Reference Signal Received Power (RSRP) for the target direction, and the gain provided by the 4-bit dual-polarized RIS is around 38 dB for the target beam direction.

Figure 6.2-1: The setup for the indoor test [i.15]

- **Outdoor:** As shown in Figure 6.2-2, the BS is on the rooftop of a 5-floor building and is able to cover the open area in front of the building. However, the UE in a small parking lot behind the building cannot receive signals from the BS due to a lack of propagation paths in between. In the test, a 1-bit single-polarized RIS with 1 024 elements is placed at the crossroad, which allows it to have LOS paths with the BS and the UE in the parking lot simultaneously. The distance from the RIS to the BS and the UE is around 120 meters and 20 meters, respectively. The working frequency of the communication system is 26 GHz. Compared to the case without RIS, the received RSRP increases over 30 dB.

Figure 6.2-2: The setup for the outdoor test [i.15]

- **Outdoor-to-Indoor:** Three trials are reported on different frequencies, namely, 2,6 GHz, 4,9 GHz and 26 GHz. The test environments are depicted in Figure 6.2-3, Figure 6.2-4 and Figure 6.2-5, respectively.

For the trial on 2,6 GHz, the height of the BS is 29 meters, while the distance from the RIS to the BS and the test UE is approximately 206 meters and 7 meters, respectively. The BS transmits signals in 60 MHz bandwidth using a transmission power of 120 W. The RIS used in this trial is single-polarized, with a total of 20 × 20 elements on the surface. The codebook is 1,6-bit, which means there are 3 available phase shifts on every element. The physical size of the RIS panel is 1 m × 1 m. Measurement results show that the RSRP increases 15 dB for the UE.

Figure 6.2-3: The setup for the O2I test at 2,6 GHz [i.15]

For the trial on 4,9 GHz, the BS transmits with a power of 200 W in a 100 MHz bandwidth. The distance from the RIS to the BS and the UE is approximately 145 meters and 45 meters, respectively. The RIS is 2-bit dual-polarized, with 32 × 32 reflective elements and the physical size is 1 m × 1 m. The test UE is inside the lobby of the building, which is a typical weak coverage area. The RSRP increases 21 dB after the RIS is placed.

Figure 6.2-4: The setup for the O2I test at 4,9 GHz [i.15]

For the trial on 26 GHz, the BS is located on the rooftop of a 3-floor building overlooking the site, and there is a long corridor extending from the entrance to the inside of the building. The bandwidth of the transmitted signal is 100 MHz. The distance from the BS to the RIS is around 45 meters, while in Figure 6.2-5 the RIS is not visible since the photo is taken at the location of the RIS. In the trial, a 1-bit dual-polarized RIS with 64 × 64 elements is used to reflect the beam from the BS into the corridor where the test UE is located. During the test, the UE moves from the entrance all the way into the building along the corridor. When there is no RIS deployed, within 30 meters into the corridor the received signal fades away and the RSRP drops to -105 dBm/RE. Comparatively, when RIS is deployed and a proper codebook is used, even at the end of the corridor, which is 106 meters inside the building, the received signal strength is still medium strong with a RSRP of -93 dBm/RE.

Figure 6.2-5: The setup for the O2I test at 26 GHz [i.15]

Another ISG member has reported similar trial results for an indoor E2E communication on 4,7 GHz.

This trial was conducted in a typical office building, and the setup is illustrated in Figure 6.2-6. In this setup, the Radio Unit (RU) is the base station's radio unit, and the UE is a standard commercial cell phone. The corridor, affected by Non-Line-Of-Sight (NLOS) propagation, is considered a blind zone. To overcome this, RIS with an oblique angle of 30° facing the RU were deployed in the corridor to simulate Line-Of-Sight (LOS) propagation. The RIS panel, operating for 4,7 GHz, reflects electromagnetic waves towards the UE. PIN diodes are used as the 1-bit control approach to reconfiguring the reflection feature, the designed unit cell with the PIN diode providing less than 1 dB loss and 0°/180° reflection from a horizontally polarized incidence. The implemented RIS panel is of array size 40 × 40, physical size 1,276 × 1,276 m^2 (considering half wavelength, 31,9 mm, to be the physical size of the unit cell), and the average radiation gain is 18,1 dB within the scanning range of ±50°. The specifications of the RIS prototype are summarized in Table 6.2-1. The UE was moved along the corridor and measurements were performed on positions labelled 0 - 8 in Figure 6.2-6. Two sets of experiments were performed, and the differences are outlined in Table 6.2-1.

Table 6.2-1: Specification of RIS panel used in the trials

Operating Frequency	4,7 GHz
RIS Type	Reflective RIS
Polarization Type	Single (Horizontal Polarization)
RIS Array Size (Number of Unit Cell)	40 × 40 (1 600)
Physical Dimension of the square RIS	1,276 × 1,276 m^2
Unit Cell Control	1-bit control (using PIN to control phase)
Reflection Phase Shifting	0° and 180°
Reflection Loss	< 1 dB
Beam Scanning Range	±50°
Averaged Gain of RIS	18,1 dB

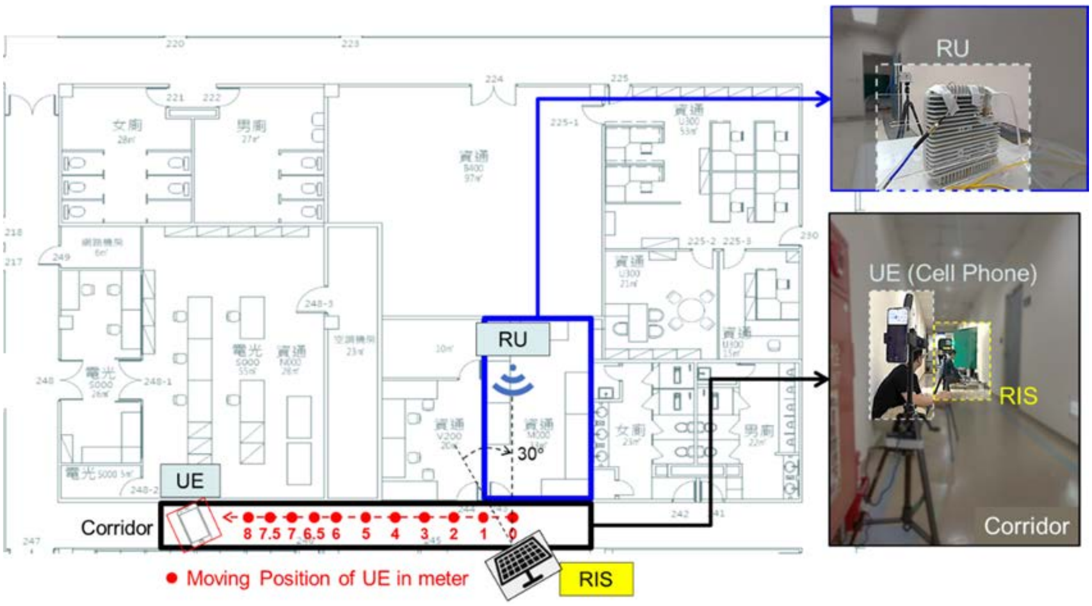

NOTE: Red points are the moving positions of UE during the test of UE receive performance (system throughput for which the measured result depends on the MCS index in Table 6.2.2). Trial results show a comparison of MCS indexes of UE with and without RIS.

Figure 6.2-6: Setup of field trail for indoor E2E communication

Table 6.2-2: Differences between the two experiments

	Experiment A	Experiment B
Tx antenna	Horn antenna	Omnidirectional antenna
Measurement	MCS Index	PDU session setup (Success/Fail)

Figure 6.2-7 shows the trial results of Experiment A. The MCS index value is the max MCS (Modulation Coding Scheme) index that a stable Block Error Rate (BLER) can be achieved. The MCS index can be translated to maximum throughput and a higher MCS index implies higher maximum throughput. The distances from RIS to RU and RIS to UE are 5 m and 8 m, respectively. In Figure 6.2-7(a), the case without RIS is illustrated, which shows that the MCS level decreases fast as UE moves away from the LOS position. Consequently, Figure 6.2-7(b) shows the case with RIS. It can be seen that the MCS index is enhanced at all locations.

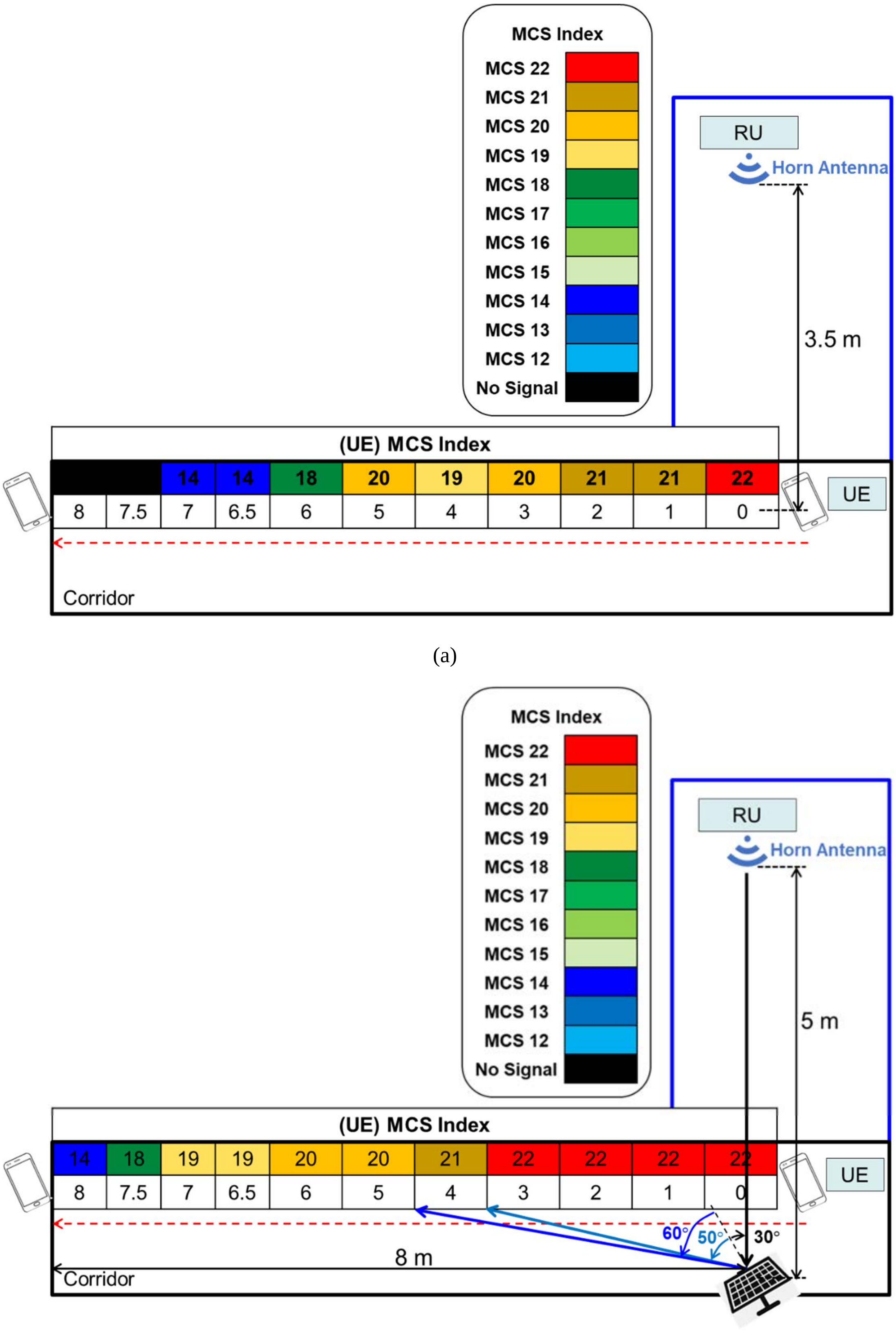

(UE) MCS Index

No Signal	No Signal	14	14	18	20	19	20	21	21	22
8	7.5	7	6.5	6	5	4	3	2	1	0

(a)

(UE) MCS Index

14	18	19	19	20	20	21	22	22	22	22
8	7.5	7	6.5	6	5	4	3	2	1	0

(b)

Figure 6.2-7: Experiment A results: (a) Without RIS, (b) With RIS

In Experiment B, an omnidirectional antenna was utilized in the testing scenario. This represents a more realistic scenario. Unlike Experiment A where the MCS index is measured, in Experiment B, the PDU session setup was used as a KPI. When compared to the MCS index, the successful setup of a PDU session requires more uplink/downlink messages to be exchanged between RU and UE than the receiving of the MCS index. Therefore, it can be used as an indication that uplink/downlink data transmission can be completed. The trial results are captured in Figure 6.2-8. The results in Figure 6.2-8(a) show that, without RIS, the PDU session setup is successful only at the LOS position. In Figure 6.2-8(b), the PDU session setup is successful by the RIS reflection angle within the 50-degree range. With the trial results, it can be seen that RIS can help to extend coverage in the blind zone/coverage hole.

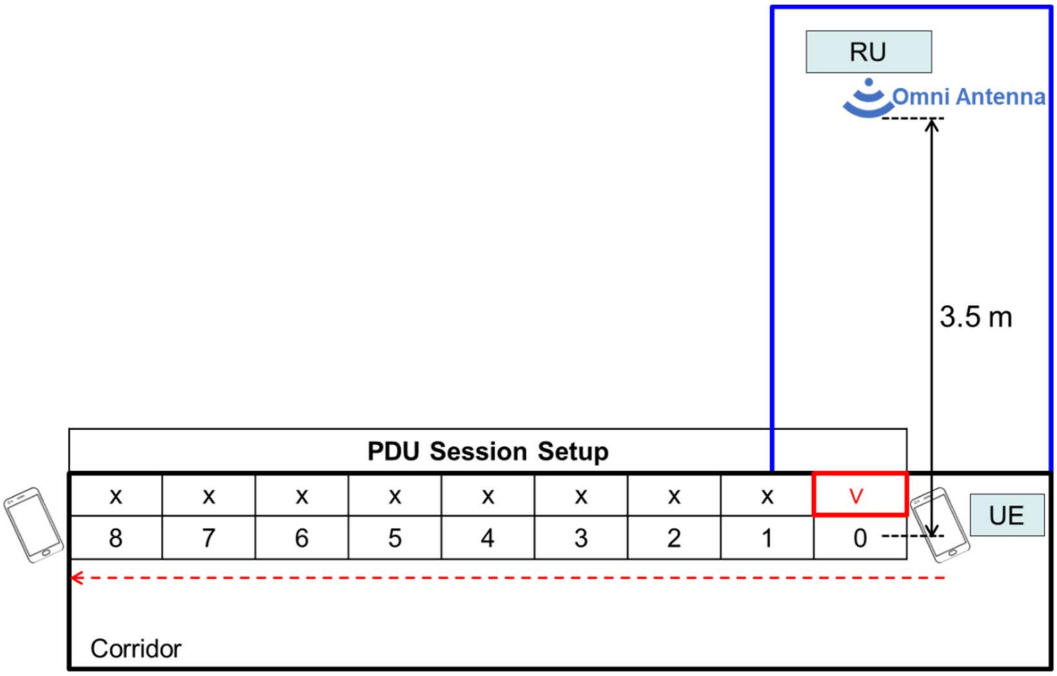

(a)

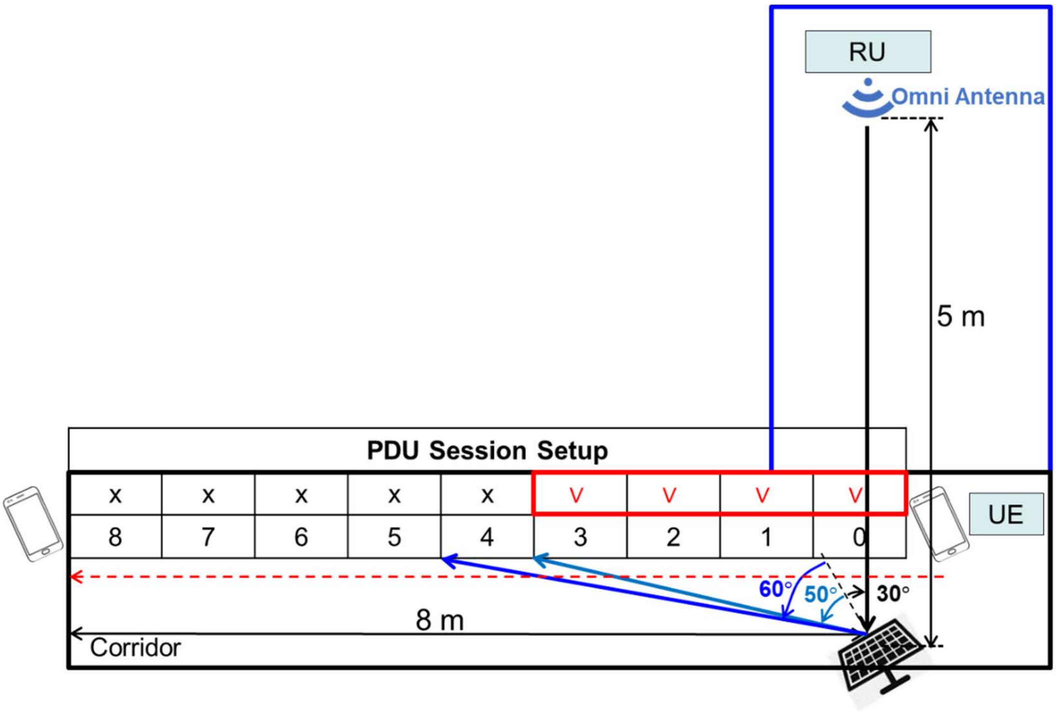

(b)

Figure 6.2-8: Experiment B results: (a) Without RIS, (b) With RIS

Finally, another ISG member performed a field test with 5G mmWave RIS in a typical real-world environment and reported successful results. The trials were conducted using commercial infrastructure and equipment that are deployed by operators for public usage as part of their 5G network. The used RIS was previously tested and validated in both anechoic chambers and in a controlled environment.

Use Case and Objective

This study investigates the typical operation of a Reconfigurable Intelligent Surfaces (RIS) to extend the coverage area of a 5G mmWave base station. Specifically, it aims to enhance the received signal strength at locations obstructed by physical barriers. The primary objective is to demonstrate how RIS can improve connectivity in environments with significant obstructions, such as an open train station. This setting, characterized by varying levels of human traffic and physical obstacles, provides a realistic and challenging scenario for evaluating the effectiveness of RIS technology.

Setup Description

The tests were conducted at an open train station over three days during regular working hours to account for fluctuating traffic levels and other environmental factors. The equipment used for the tests included a RIS designed for mmWave operation with 1 600 individual cells with parameters specified in Table 6.2-3, a 5G mmWave access point installed by the network operator, and a 5G mmWave capable smartphone equipped with software to display received signal power and beam index.

Table 6.2-3: 5G mmWave RIS used in the field trial

Parameter	Value
Operational frequency	27 GHz
Number of elements	1 600 (40 x 40)
Number of states	1-bit, 2 states
Polarization	V and H
Beam scanning range	±60°
Panel size	20 x 20 cm

Procedure

The procedure began by selecting locations within the train station that were shadowed from the access point by obstacles such as walls or large equipment. The RIS was then placed in a position where it had a clear line of sight to both the access point and the shadowed location. Measurements of received signal power and data rate for general internet access were taken at the shadowed location, both with and without the RIS in operation. The RIS was set to beamform optimally at the beam covering the shadowed location. This process was repeated at multiple shadowed locations to ensure consistency and reliability of the results. At the first location, the RIS was placed 21 m away from the access point, and at the second location, the RIS was placed 30 m away from the access point. In both tests, the user equipment was a few meters away from the RIS. Figure 6.2-9 shows the setup at location 1 and Figure 6.2-10 shows the setup at location 2.

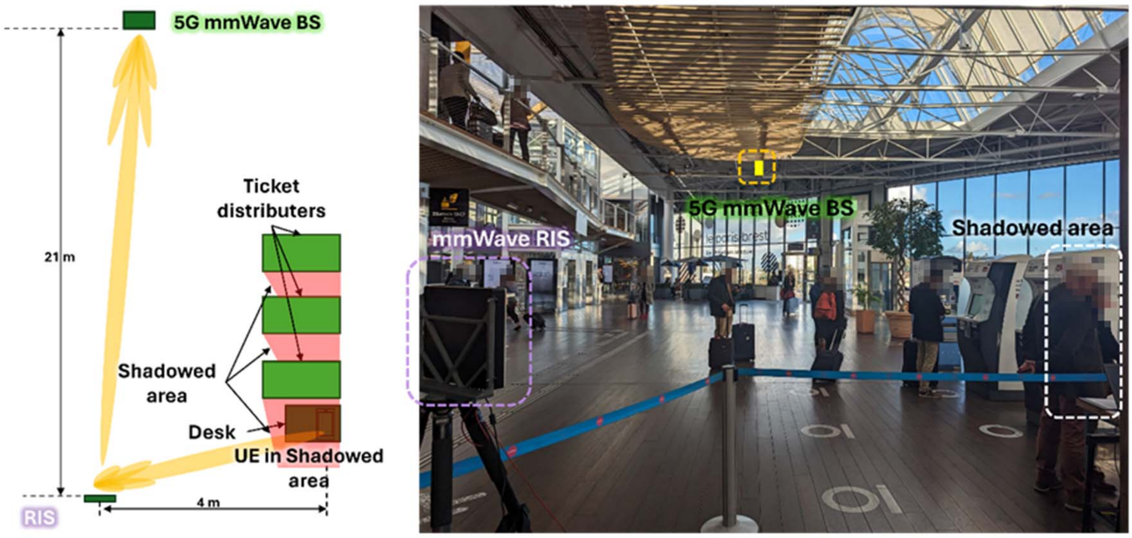

(a) The setup plan (b) The setup location

Figure 6.2-9: The first test location setup

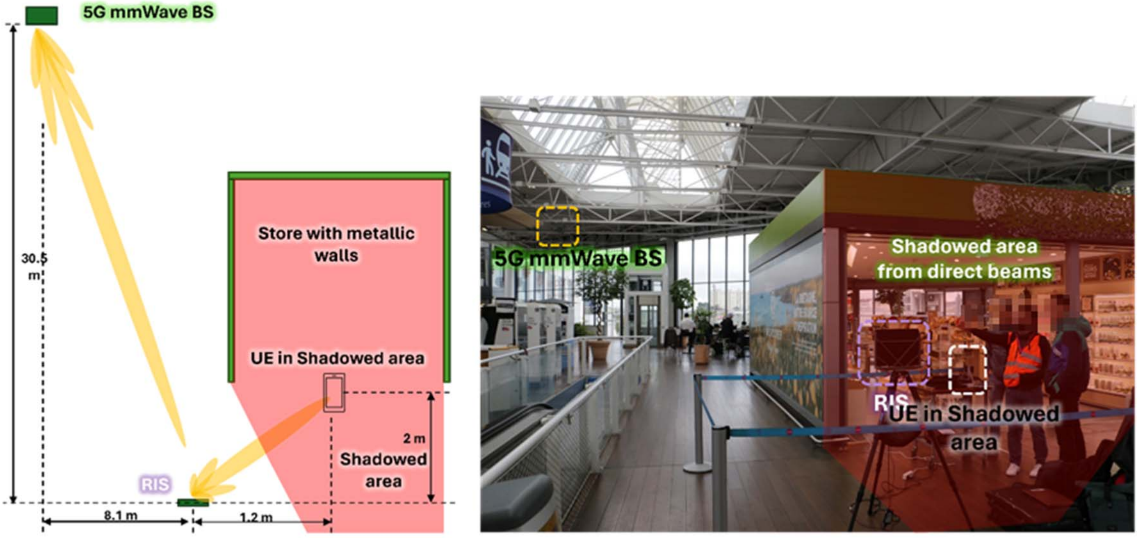

(a) The setup plan (b) The setup location

Figure 6.2-10: The second test location setup

Results

The deployment of the RIS in the train station significantly improved signal strength and data rate at the shadowed locations. Without the RIS, the received signal power was around -94 dBm. With the RIS, the signal power increased to approximately -72 dBm, demonstrating a gain of over 20 dB. Additionally, the data rate experienced an increase exceeding 50 % with the RIS in operation. Figures 6.2-11 and 6.2-12 show the received power and beam index at locations 1 and 2 respectively, with and without the RIS beamforming.

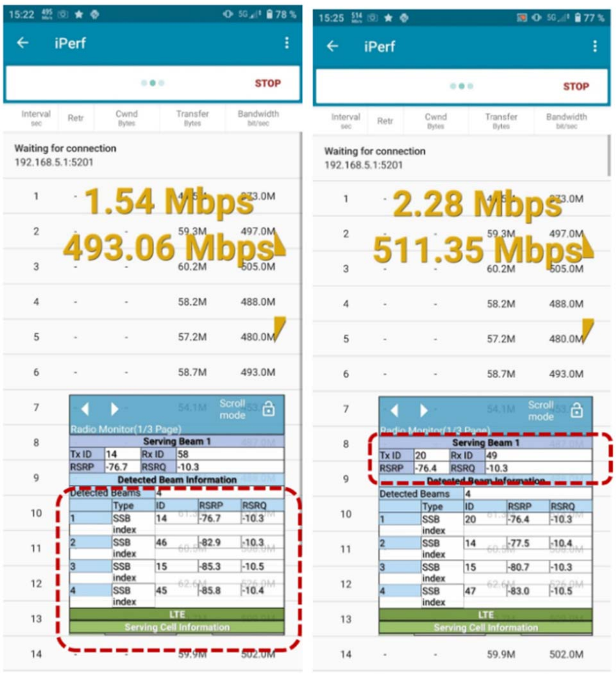

Waiting for connection
192.168.5.1:5201

Radio Monitor(1/3 Page)

Serving Beam 1			
Tx ID	14	Rx ID	58
RSRP	-76.7	RSRQ	-10.3

Detected Beam Information

Detected Beams 4

	Type	ID	RSRP	RSRQ
1	SSB index	14	-76.7	-10.3
2	SSB index	46	-82.9	-10.3
3	SSB index	15	-85.3	-10.5
4	SSB index	45	-85.8	-10.4

(a) Without RIS

Waiting for connection
192.168.5.1:5201

Radio Monitor(1/3 Page)

Serving Beam 1			
Tx ID	20	Rx ID	49
RSRP	-76.4	RSRQ	-10.3

Detected Beam Information

Detected Beams 4

	Type	ID	RSRP	RSRQ
1	SSB index	20	-76.4	-10.3
2	SSB index	14	-77.5	-10.4
3	SSB index	15	-80.7	-10.3
4	SSB index	47	-83.0	-10.5

(b) With RIS

Figure 6.2-11: The first test location data rate and RSRP comparison

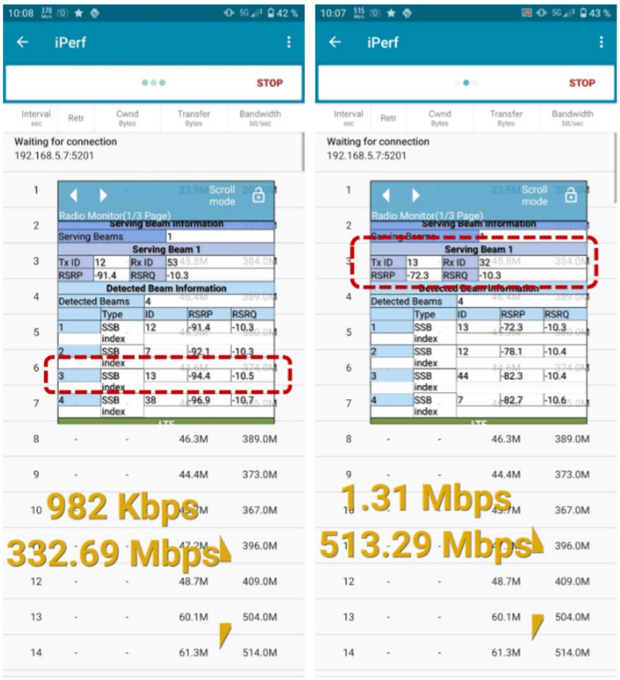

Waiting for connection
192.168.5.7:5201

Radio Monitor(1/3 Page)

Serving Beam Information

Serving Beams 1

Serving Beam 1			
Tx ID	12	Rx ID	53
RSRP	-91.4	RSRQ	-10.3

Detected Beam Information

Detected Beams 4

	Type	ID	RSRP	RSRQ
1	SSB index	12	-91.4	-10.3
2	SSB index	7	-92.1	-10.3
3	SSB index	13	-94.4	-10.5
4	SSB index	38	-96.9	-10.7

(a) Without RIS

Waiting for connection
192.168.5.7:5201

Radio Monitor(1/3 Page)

Serving Beam Information

Serving Beams 1

Serving Beam 1			
Tx ID	13	Rx ID	32
RSRP	-72.3	RSRQ	-10.3

Detected Beam Information

Detected Beams 4

	Type	ID	RSRP	RSRQ
1	SSB index	13	-72.3	-10.3
2	SSB index	12	-78.1	-10.4
3	SSB index	44	-82.3	-10.4
4	SSB index	7	-82.7	-10.6

(b) With RIS

Figure 6.2-12: The second test location data rate and RSRP comparison

The analysis of interference revealed that the RIS's beam had a narrow reflected beamwidth of 3 degrees, which minimized interference. The received power dropped by 12 dB just 10 cm away from the intended receiver, indicating highly localized beamforming and reduced spillover. Figure 6.2-13 shows the variation of the Received Signal Power (RSRP) with respect to the relative position from the targeted receiver. This figure shows how much the RSRP will drop at the receiver actual position when it is offset from the targeted focal point with a certain distance (relative location in cm) and considers two settings of RIS beamwidth set as 3° and 6°.

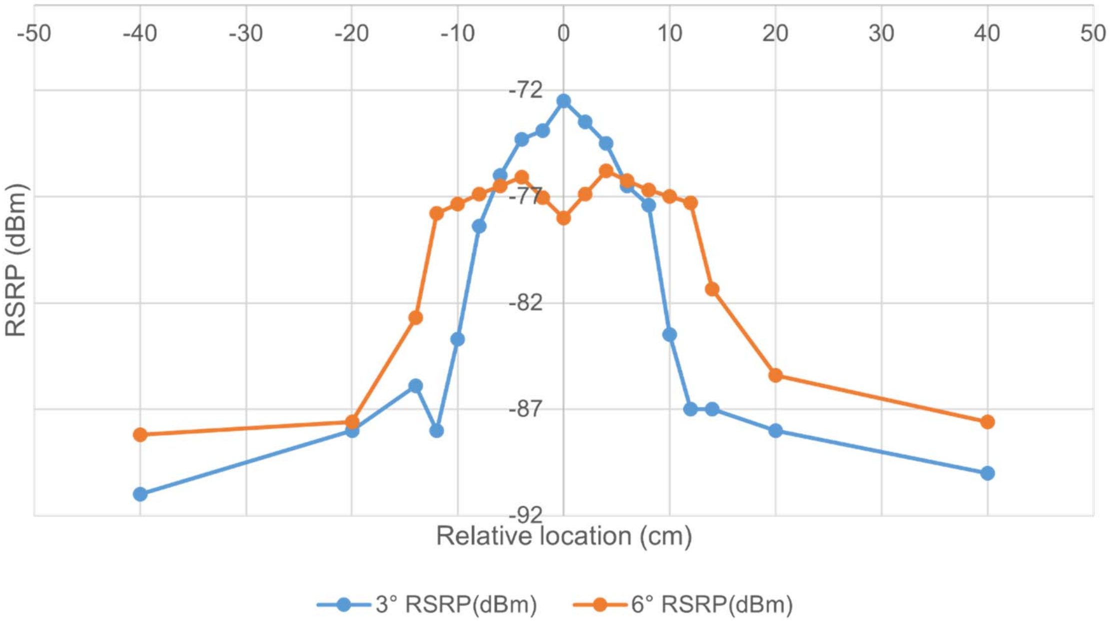

Figure 6.2-13: The achieved RSRP around the focal point with respect to the distance from the centre of the target in cm with the RIS beamwidth set as 3° and 6°

6.3 RIS Bistatic RCS Measurements

Typical physical scenarios of the RIS, as mentioned in [i.18], include:

i) a spherical wave; and

ii) a plane wave impinging on the RIS, which correspond to obtaining near-to-far (the BTS is close to the RIS and the UE is far from the RIS) and far-to-far (both the BTS and UE are far from the RIS) field distributions, respectively.

However, the near-to-far configuration is similar to reflectarray scenarios, and the distributions of the reflective fields can be verified in typical anechoic antenna test ranges. Besides, the far-to-far configuration should represent the majority of the RIS operation scenarios in practical applications, where both the BTS and UE are far from the RIS, interacting under far field conditions. Therefore, it is essential to establish reliable test environments to evaluate the scattering characteristics of the plane waves incident on the RIS from different angles to obtain the reflection and transmission field distributions caused by the RIS. This will allow a more precise analysis of the potential scattering behaviours when using RIS platforms for proper deployment and to compare signal distributions from field tests for coverage verifications. Below are discussed the three typical usage scenarios for the RIS:

i) Near-to-Far;

ii) Far-to-Far, and

iii) Far-to-Near:

Near-to-Far Scenario: In this scenario, the BTS is close to the RIS, while the UE is in the far-field region of the RIS. Since the BTS is in the near zone of the RIS, the RIS operates similarly to the conventional reflectarray antenna in term of the physical scenario.

Far-to-Far Scenario: This is a common application scenario for the RIS. Here, both the BTS and UE are far from the RIS with a local plane wave impinging on the RIS. The RIS then redirects the incident wave into other directions. Both d_1 and d_2 satisfy the far-field conditions of the RIS. Field distribution tests can be conducted in a bistatic RCS mode.

Far-to-Near Scenario: In this scenario, the BTS is in the far-field region of the RIS, while the UE is in the near zone of the RIS. Near-field distributions scattered from the RIS may be obtained by applying near-field scans with holographic imaging processing for a plane wave illumination on the RIS under bistatic operation scenes. Measurements of the near-field propagation characteristics are important for RIS-aided near-field system applications, and further guidance is provided in ETSI GR RIS 007 [i.19].

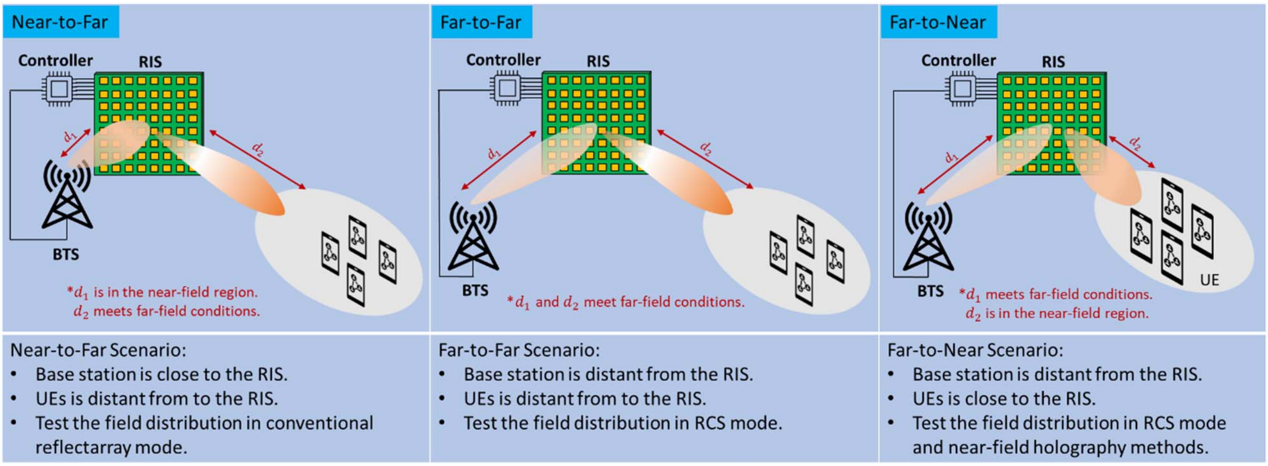

Near-to-Far Scenario:

- Base station is close to the RIS.
- UEs is distant from to the RIS.
- Test the field distribution in conventional reflectarray mode.

Far-to-Far Scenario:

- Base station is distant from the RIS.
- UEs is distant from to the RIS.
- Test the field distribution in RCS mode.

Far-to-Near Scenario:

- Base station is distant from the RIS.
- UEs is close to the RIS.
- Test the field distribution in RCS mode and near-field holography methods.

Figure 6.3-1: Illustration of the scenarios considered for the RIS measurement

As depicted in Figure 6.3-2, a sample schematic of the implemented hybrid measurement system for RIS bistatic RCS pattern verifications illustrates a Compact Antenna Test Range (CATR) integrated with a side-deployed Planar Near Field Scanner (PNFS) for the bistatic scattering tests [i.20]. The CATR system comprises a feed antenna and a roll-edged parabolic reflector. The feed antenna is positioned at the focal point of the reflector, where it generates a spherical wavefront directed toward the reflector. The reflector then produces a collimated beam (plane wave) aimed at the RIS. The scattering field is subsequently measured by the side-deployed PNFS. The near field probe scans the radiating near field region of the RIS, capturing the amplitude and phase distributions of the scattered fields. Then, near-field to far-field transformation techniques are applied to derive the far field scattering patterns. Additionally, near-field holographic imaging can be employed to evaluate the field distributions in the near zone of the RIS. This bistatic measurement system is particularly useful for creating far-to-far and far-to-near scenarios for the RIS bistatic scattering tests. Specifically, the plane wave generated by the CATR effectively emulates base station signals incident at a specific angle onto the RIS aperture from a far distance. The near-field scanner measures the RIS scattering in the radiating near-field zone and processes to obtain the bistatic RCS patterns of the RIS for the far-to-far scenario to be discussed further in the following. As for the far-to-near scenario, this bistatic measurement system may also be applied for characterizing the near-field propagation of the RIS-aided near-field communication system discussed in ETSI GR RIS 007 [i.19].

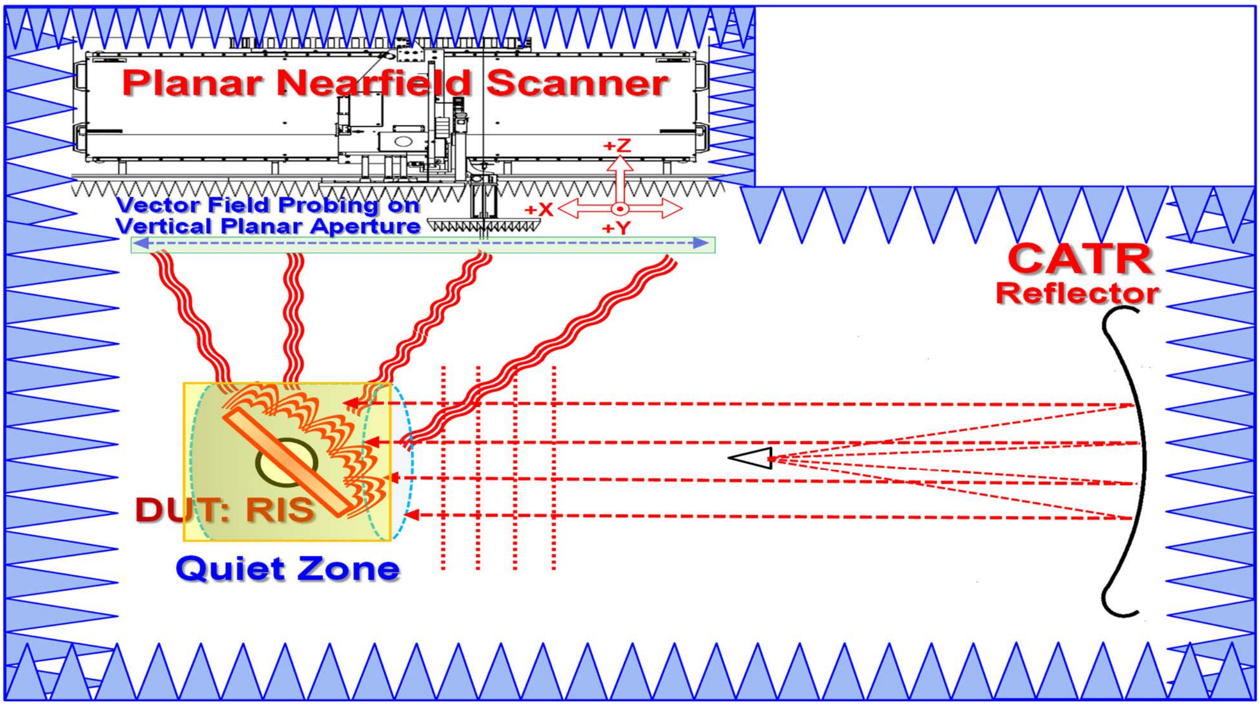

Figure 6.3-2: A sample schematic of the bistatic scattering characterization test for the RIS

Bistatic RCS refers to the measurement of scattering when the transmitter and receiver are located in different directions in the far regions. For the RIS, the energy transfer effects can be analysed and evaluated properly through bistatic RCS measurements. As shown in Figure 6.3-2, the bistatic RCS patterns of the aluminium plates are determined by applying a full wave simulation software for the plane wave incident at 30° and 45° angle on the metal surface, respectively. Also, the maximum bistatic RCS of the flat metal plate can be approximated with the Physical Optics (PO) method by the following equation in the specular reflection direction:

$$\sigma_{oi} = \frac{4\pi {A_{eff}}^2}{\lambda^2} = \frac{4\pi (A \times cos\theta_{inc})^2}{\lambda^2}$$

where σ_{oi} is the specular bistatic RCS for oblique wave incidence, A_{eff} is the effective illuminated area, A is the physical area of the metal plate, θ_{inc} is the oblique angle of incidence, and λ is the wavelength of the incident wave. This equation assumes that the plate dimensions are significantly larger than the wavelength of the incident wave. Therefore, the effective illuminated area of the incident wave can be calculated by multiplying the physical area of the plate with the cosine of the angle of incidence. Figure 6.3-3 illustrates respectively the bistatic RCS patterns of 10 × 10, 30 × 30, and 60 × 60 (cm^2) aluminium plates with a thickness of 3 mm at a frequency of 28 GHz, as detailed in [i.20]. The simulation results, σ_{sim} are obtained by using the full-wave simulation software. The σ_{PO} values are the specular bistatic RCS values calculated with the PO method. However, for more accurate results, full-wave simulations should be employed.

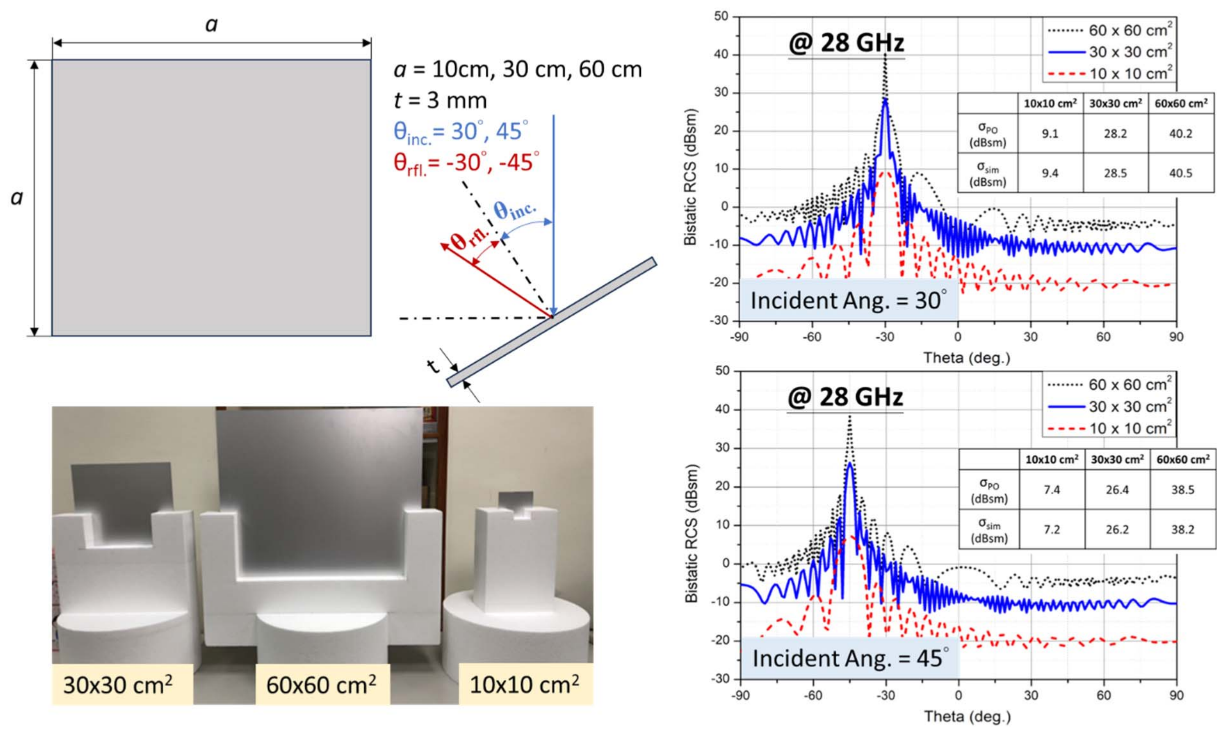

Figure 6.3-3: Bistatic RCS simulations for metal plates

Figure 6.3-4 illustrates an implemented hybrid measurement range for the bistatic test shown in Figure 6.3-2, which integrates the CATR with the side-deployed PNFS detailed in [i.20]. The planar wavefront is generated by a parabolic reflector with a roll-edge design, so that qualified test range performance through a validated Quiet Zone (QZ) certification procedure can be obtained, such as controlling cross-polarization to -30 dB on-axis, amplitude taper to 1 dB, amplitude ripple to ± 0,5 dB, and phase variation to ± 5° within a reasonably large QZ for the 5G NR FR2 band. This wavefront emulates the actual RF waves emitted by a distant BTS illuminating the RIS. Then, the scattered fields from the RIS are obtained through 3D pattern measurements using the PNFS, deployed at the side wall for planar near-field scanning. Thus, the bistatic RCS patterns in directions covered by the side-deployed PNFS can be measured. Other configurations of the near-field scanner may be employed, such as cylindrical scanning on a fixed Device Under Test (DUT) with its linear-scan axis coinciding with the CATR broadside axis going symmetrically through the centre of QZ. Thus, a nearly full coverage of the bistatic RCS patterns from the DUT may be obtained.

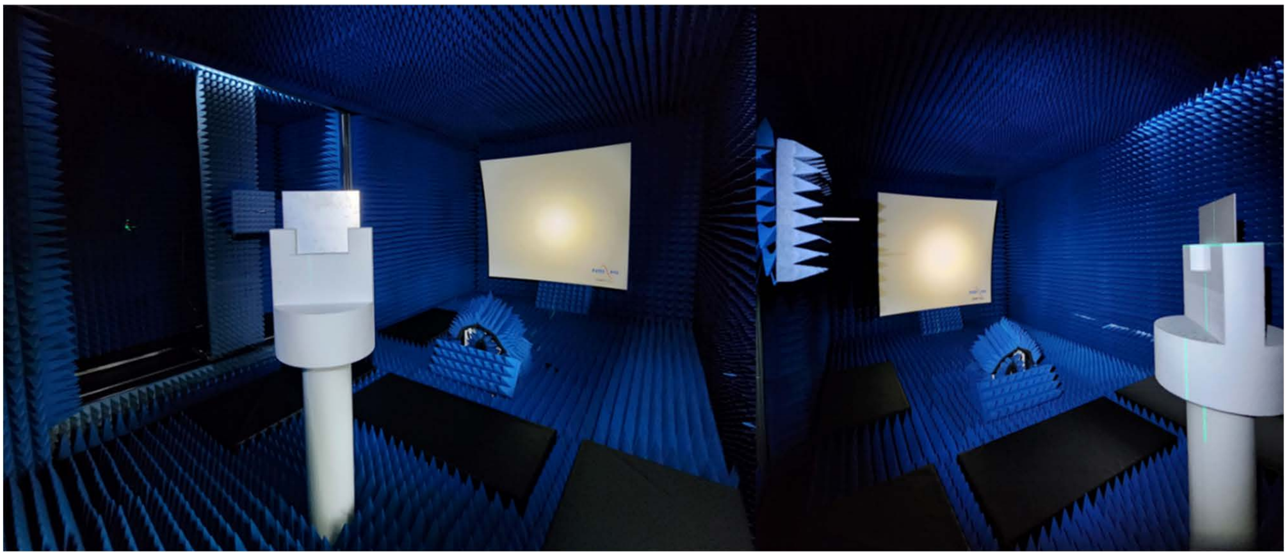

Figure 6.3-4: A plane-wave scene emulation range
for measuring the bistatic scattering performance of the DUT

The measured bistatic RCS patterns for different metal plate sizes at 30° and 45° incident angles under vertical and horizontal polarization conditions are shown in Figure 6.3-5, which are highly consistent with those obtained by using the full-wave simulation software, regarding the RCS offsets for different metal plates. Since the specular RCS values of the metal plates can be determined accurately, the metal plates may serve as the bistatic RCS calibration references of the RIS. Additionally, in Figure 6.3-5, a strong scattering at an angle greater than 80 degrees occurs, which is caused by a reflection from the rolled edge of the reflector. Due to the large angle away from those of the DUT, it will not interfere with the bistatic RCS of the DUT and, on the other hand, may provide an alternative and stable reference for the bistatic RCS tests. However, if a serrated edge reflector is used in the compact range, the scattering from the serrations will result in wide-spreading scattering, which could potentially interfere with the measured bistatic RCS patterns of the RIS, as per [i.21].

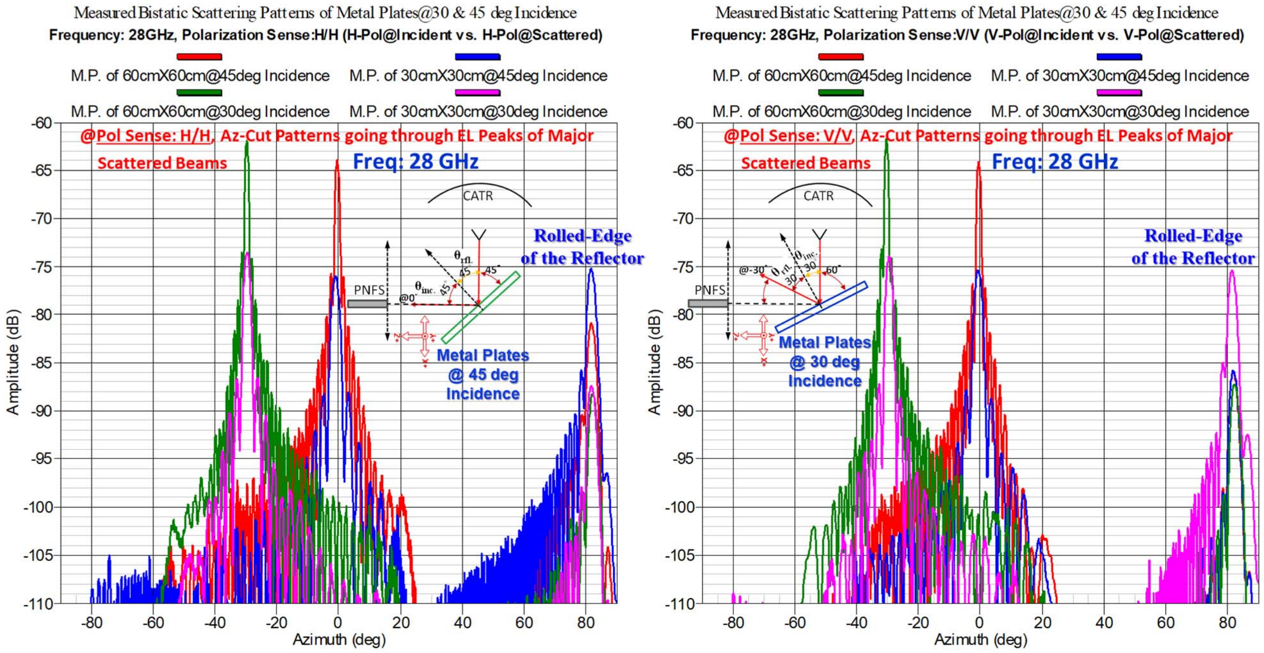

Figure 6.3-5: Measured bistatic scattering patterns in the azimuth cut for the metal plates deployed at 30° and 45° incident angles

A passive RIS structure with 73 × 73 elements is placed within the quiet zone of the CATR, as shown in Figure 6.3-6. The passive RIS is constructed using a low-loss dielectric substrate (RO4003C) with dimensions of 40 × 40 cm^2 in length and width, and 1,5 mm in thickness. This design exhibits a reflection characteristic with a 30° incidence angle and a -10° reflection angle. The measured far-field bistatic scattering pattern of the passive RIS is represented by the blue line and that of the 30 × 30 cm^2 metal plate used for calibration is represented by the pink line, as shown in Figure 6.3-6. To keep the incidence angle consistent with that of the passive RIS, the metal plate is oriented with the 30° incidence angle too. Due to the coordinate system of the PNFS, the peak of the bistatic RCS pattern for the RIS appears at an azimuth angle of -50° and that for the metal plate is -30°, as expected. Calibrated with the specular RCS value of the 30 × 30 cm^2 metal plate, this passive RIS achieves an RCS value of approximately 30 dBsm in the reflected angle -10° from the normal at a frequency of 28 GHz. The measured 3D bistatic RCS patterns of the RIS can be applied in a ray tracing simulation tool for determining the field distributions from the RIS illuminated by the BTS far from the RIS to enhance the deployment of the RIS in the far-to-far scenario. Besides, those bistatic RCS patterns may be used for link budget calculations in RIS-aided communication systems.

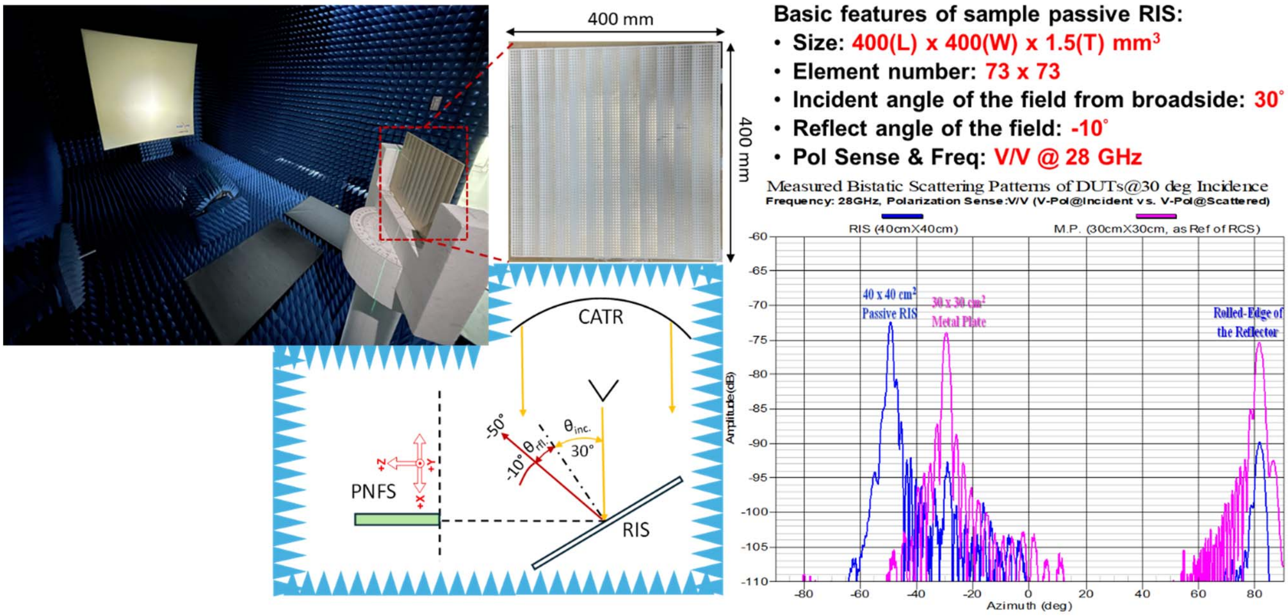

Figure 6.3-6: Measured bistatic scattering patterns in the azimuth cut for the RIS and metal plate deployed at a 30° incident angle

6.4 RIS Radiation Pattern Measurement

Radiation patterns for a RIS can be measured according to its spherical coordinates $RIS_{(\theta,\varphi)}$. The radiation pattern measurement allows to evaluate the Effective Isotropic Re-Radiated Power (EIRRP) of reflective/refractive waves from the RIS, its Side Lobe Levels (SLLs), directivity, and the Integrated Re-Radiated Power (IRRP). Under the far field conditions, the power density incident upon the RIS from T_x can be calculated as follows:

$$S_{inc} = P_{Tx} + G_{Tx} - L_{Tx} + 10\log_{10}\frac{1}{4\pi\, {d_{Tx}}^2}$$

Then, the unmeasured $EIRRP_{RIS_{(\theta,\varphi)}}$ radiated by the RIS is defined as follows:

$$EIRRP_{RIS_{(\theta,\varphi)}} = S_{inc} + (\sigma_{RIS})_{dB}$$

Finally, the $EIRRP_{RIS_{(\theta,\varphi)}}$ can be measured, assuming far field conditions are met, based upon the measured received power P_{rx} at the R_x as follows:

$$EIRRP_{RIS_{(\theta,\varphi)}} = P_{rx} - G_{Rx} + L_{Rx} - 20\log_{10}\frac{\lambda}{4\pi\, d_{Rx}}$$

In the equations presented above, σ_{RIS} is the bistatic RCS of the RIS previously defined in clause 6.3, P_{Tx} is the transmit power, G_{Tx} and G_{Rx} are the gains of the transmit and the receive antennas, L_{Tx} and L_{Rx} (greater than 0 dB) are the cable losses, including the antenna mismatch, λ is the wavelength, d_{Tx} is the distance between the RIS and T_x antenna, and d_{Rx} is the distance between the RIS and R_x antenna.

The radiation pattern measurement setup is illustrated in Figure 6.4-1 with the test equipment specified in Table 6.4-1 and the RIS under test described in Table 6.4-2. In this setup, a single polarized unmodulated carrier wave is excited with a horn antenna T_x towards the RIS, and its reflection was measured from the RIS by another horn antenna R_x. The transmit power was set to 1 dBm. The first step in the measurement is to estimate the loss terms L_{Tx} and L_{Rx}, as well as the path loss, so that they can be taken out of the equation, followed by a time delay gating to remove the direct coupling path between the antennas. Then, the R_x antenna attached to a DC servo motor is moved to realize azimuth pattern scanning, collecting EIRRP values across the portion of the virtual sphere of interest around the RIS under test. A Vector Network Analyser (VNA) is used to record the intensity and phase, which construct radiation patterns for TE and TM modes that are achieved by rotating both antennas.

Ideally, the radiation pattern measurement should be performed with the far-field conditions satisfied for both R_x and T_x antennas, however, due to space constraints it is not always permissible, and the near-field to far-field transformation of the measured EIRRP values may be performed. Also, to achieve sufficient accuracy, the pattern measurement angular step should be based on the Nyquist sampling theorem. For example, in the 3,5 GHz RIS measurement illustrated in Figure 6.4-1, the 2° angular step was set in the VNA.

From the analysis of the RIS radiation patterns, it is possible to determine:

- The directivity and the EIRRP of the reflected wave from the RIS for evaluated reflection/refraction angles.
- The SLLs that may contribute to the spurious emissions of the RIS and its interference to other users. The evaluation of spurious emissions and RF interference is necessary to confirm that the RIS is compatible with the requirements specified in clause 5.1 of the present document and in Table 2 of ETSI GR RIS 002 [i.2].
- The specular reflection lobe level or in other words, the normal reflection of the RIS.
- Reflected/refracted beam widths for evaluated reflection/refraction angles.

Following the measurement of radiation pattern for each RIS configuration angle (θ,φ), its directivity at the angle $D_{RIS(\theta,\varphi)}$ can be expressed as follows:

$$D_{RIS(\theta,\varphi)} = \frac{EIRRP_{RIS(\theta,\varphi)}}{\frac{1}{4\pi}\int_0^{2\pi}\int_0^{\pi} EIRRP_{RIS(\theta,\varphi)} \sin\theta \, d\theta \, d\varphi} = \frac{EIRRP_{RIS(\theta,\varphi)}}{IRRP_{RIS}}$$

The above equation equates to the ratio of the power density radiated in the far field at $RIS_{(\theta,\varphi)}$ relative to the power density assumed to be from an isotropic source radiation equating to the IRRP. This ratio can also be expressed as:

$$IRRP_{RIS}(\text{dBm}) = EIRRP_{RIS_{(\theta,\varphi)}}(\text{dBm}) - D_{RIS(\theta,\varphi)}(\text{dBi})$$

However, when the RIS pattern has many side lobes, it may be difficult to measure them all individually. If this is the case, and also in the case of a multi-beam reflective/transmissive RIS or a STAR-RIS, the IRRP from the RIS can be numerically approximated from a set of sampled $EIRRP_{RIS_{(\theta,\varphi)}}$ values in a sphere, by applying the following formula, and considering both polarizations:

$$IRRP_{RIS} \approx \frac{\pi}{2NM} \sum_{n=1}^{N-1} \sum_{m=0}^{M-1} \Big(EIRRP_{\theta}(\theta_n,\varphi_m) + EIRRP_{\varphi}(\theta_n,\varphi_m) \Big) \sin\theta_n,$$

where N are the $EIRRP_{RIS_{(\theta,\varphi)}}$ values along the θ-axis, and M are the EIRRP values along the φ-axis for a total of $N \times M$ measurements in a full sphere. This formula only works for constant angular spacing or the trapezoidal approximation as the integral cannot be made to reduce the formula in this manner.

Where appropriate, the full sphere $IRRP_{RIS}$ measurement can be reduced to a Partial Re-Radiated Power (PRRP) measurement. For example, for a reflective RIS measurement with a solid ground plane that acts as an impenetrable impedance for RF signals along the θ-axis with halved number of $EIRRP_{RIS_{(\theta,\varphi)}}$ samples in the semi-sphere. Note that the number of EIRRP samples in the φ-axis is still taken from a full sphere, since $\varphi \in [0,2\pi]$.

$$\text{PRRP}_{RIS} \approx$$

$$\frac{\pi}{NM} \sum_{n=1}^{N-1} \sum_{m=0}^{M-1} \Big(EIRRP_{\theta}(\theta_n,\varphi_m) + EIRRP_{\varphi}(\theta_n,\varphi_m) \Big) \sin\theta_n + \frac{1}{2} \sum_{m=0}^{M-1} \Big(EIRRP_{\theta}(\theta_n,\varphi_m) + EIRRP_{\varphi}(\theta_n,\varphi_m) \Big)$$

The PRRP_{RIS} measurement setup in a semi-sphere and its results are illustrated in Figure 6.4-1.

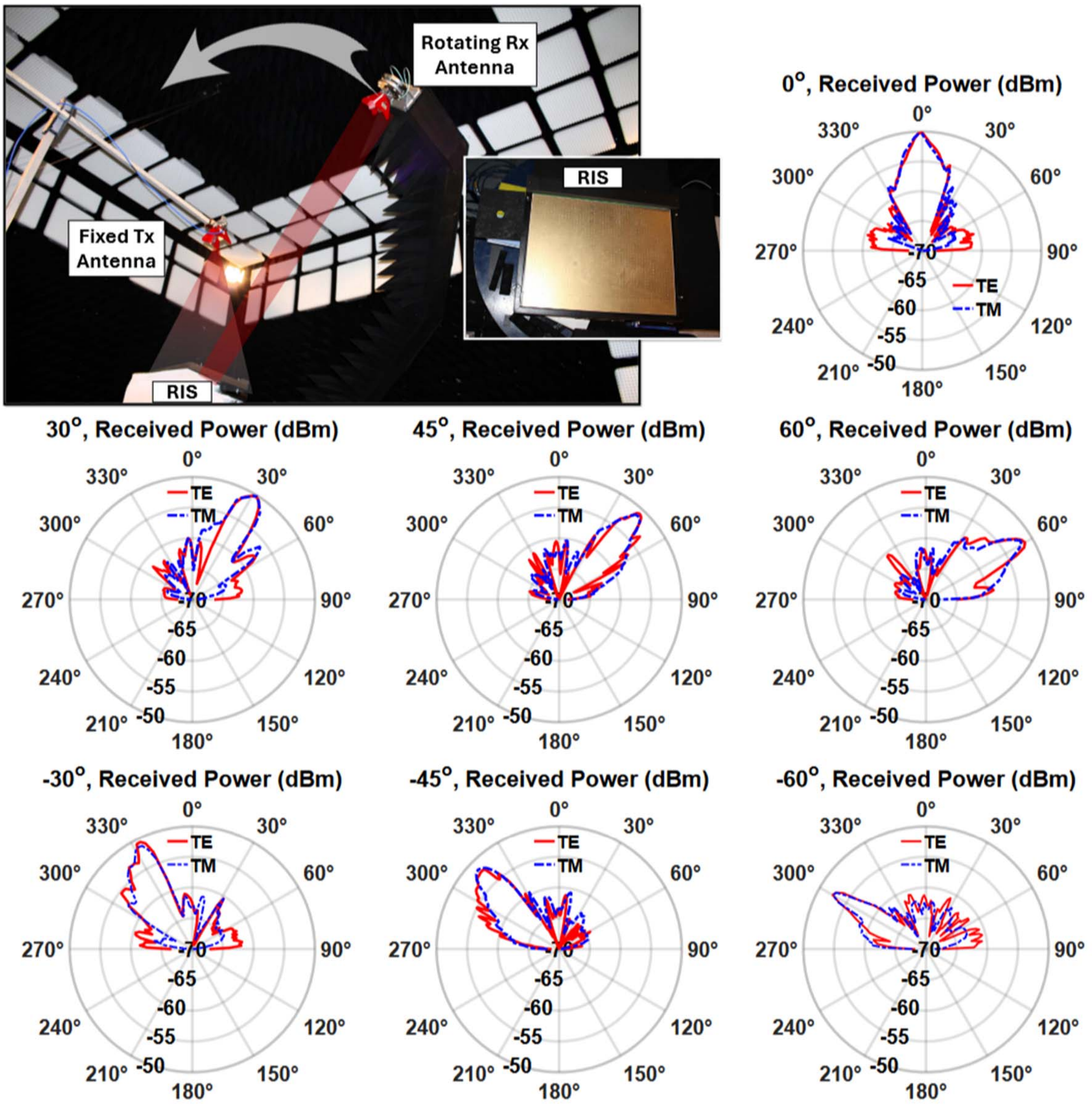

NOTE: Subfigures depict the radiation patterns of the received power for different target angles. Each pattern illustrates the effectiveness of the metasurface in modifying electromagnetic wave propagation in the set direction.

Figure 6.4-1: RIS radiation patterns of received power at various target angles at 3,5 GHz

Table 6.4-1: Test equipment

Part number	Description	Function
ETS Lindgren model 3117	Double-Ridged Guide Antenna	Transmit antenna (Tx)
ETS Lindgren model 3117	Double-Ridged Guide Antenna	Receive antenna (Rx)
Siglent SSG5060X	RF signal generator	RF signal transmitter
Keysight N5227B PNA	Vector network analyzer	RF signal receiver

Table 6.4-2: RIS specification

Operating Frequency	3,5 GHz
Type	Reflective
Polarization	Dual-polarized
Size	570 mm x 420 mm (1,850 unit cells, $\lambda/8$)
Unit cell control	2-bit digital
Switching element	Varactor diode

7 Cost, complexity and energy-efficiency analysis of RIS

7.1 RIS device cost and complexity

The introduction of RISs provides a cost- and energy-efficient solution to enabling advanced wave manipulation capabilities. However, the choice of a cost-effective switching element is critical to achieve a low overall cost for RIS. For the visual context of the RIS device, see Figure 7.1-1.

RF PIN diodes or varactor diodes tend to be expensive in relatively low volumes and their cost increases exponentially in higher frequencies such as FR2 and above. One design approach is to have RF switches connected to microstrip delay lines of different lengths to realize the phase shift, as well as the necessary control circuitry such as the MCU and control buses, where each 16 x 16 board comprises 768 flip-flops, i.e. 3 per each unit cell, 256 AND gates, 256 RF switches and 1 MCU [i.16]. The scalable design of RIS allows the construction of large apertures to suit various application scenarios while maintaining the low cost of individual parts.

Based on this example, it can be concluded that for RIS cost efficiency, there are three main sources of manufacturing costs:

1) Printed Circuit Board (PCB) production, which includes the patch antennas and the microstrips for both the delay lines and the control buses;

2) electronic components including RF switches, MCU, flip-flops, AND gates, etc.;

3) assembly of all components onto the PCB.

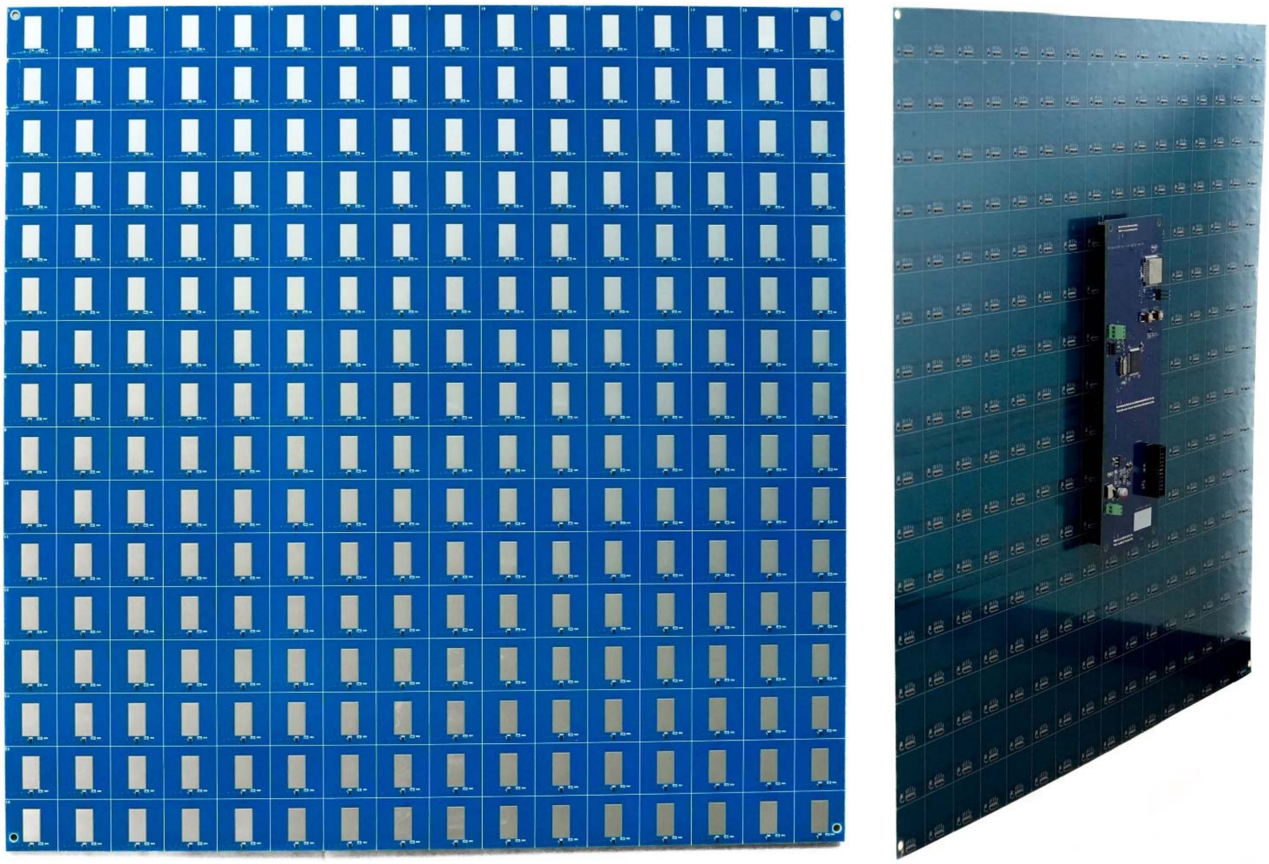

Figure 7.1-1: a) RF switch 16 x 16 and the front of the RIS b) Back of the RIS and the controller

7.2 RIS deployment costs

In this clause, a sample cost value associated with deploying RIS under existing technological advances is considered. As a measure of cost performance metric is used the Cost Performance Index (CPI), which is a frequently used project management tool and is expressed as a ratio calculated by dividing the budgeted cost of work completed (EV) by the actual cost of the work performed (AC).

$$CPI = EV/AC$$

If the calculated CPI is equal to 1, this means that the project has performed exactly on budget. If the calculated CPI is above 1, this means that the project is below budget and generates profit. Finally, if the calculated CPI is below 1, this means that the project has exceeded the budget and is likely causing a loss.

For example, RIS deployment costs can be estimated based on the 3,5 GHz RIS design from [i.16]. First, the AC costs can be easily estimated since this is a known figure. The total RIS manufacturing cost, as outlined in clause 7.1, is composed of the production cost, the assembly cost and the components cost. In this example, AC is illustrated in Figure 7.2-1 and contains cost estimations that are valid at the time of writing. The costs are estimated per RIS unit cell, because the actual number of RIS unit cells may vary, depending on the application and the available budget.

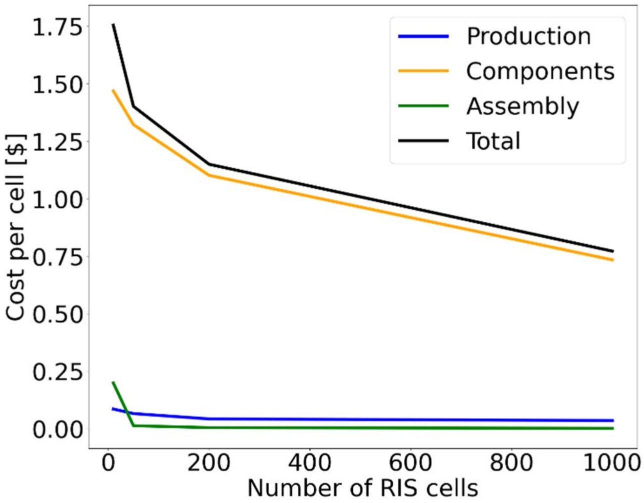

Figure 7.2-1: The Actual Cost (AC) of the work performed for the RIS design in [i.16]

The advantage of using passive components is twofold as it also significantly reduces the power consumption of the RIS. In the design featured in [i.16], nearly all the input power is devoted to the MCU, which has been measured as 62 mW, while all other components require a negligible amount of power (e.g. to keep the state of the flip-flops). Additionally, a typical MCU possesses a so-called deep sleep mode, which allows conserving power when the RIS is idle. Indeed, the MCU needs to be activated only when a change in the configuration of at least one of the unit cells is required. Such operation mode might be exploited to further reduce the power consumption of RISs in wireless networks, where the required reconfiguration rate varies dynamically depending on the instantaneous user density, speed, and other environmental conditions. The power consumption of the ARM-based MCU in sleep mode can be significantly reduced to approximately 1 μW, thus allowing deploying RISs independently of the power grid through wireless power harvesting.

Based on Figure 7.2-1 and assuming a high production volume, the total cost per unit is estimated as $1,75 per unit cell and $448 for a 16 x 16 RIS in [i.16]. Since this RIS is self-adaptive and can be powered wirelessly, the installation and maintenance costs can be considered negligible. Then, the AC becomes approximately equal to the total cost of RIS manufacturing. Finally, for the EV value, the average cost of a fiber optic-connected 5G wireless router is considered, which is at the time of writing is approximately equal to $700. Then, the calculated CPI equals 1,36, which is a great project management result and shows that RIS can be a competitive solution for 5G wireless networks, especially given that RIS does not require fiber optic connectivity to operate.

7.3 Comparative analysis

High directivity enabled by RIS offers increased efficiency and may be essential in certain scenarios, however, even slight deviations from the target can result in connectivity loss. Wider beams, on the other hand, are less efficient but more resilient to disruption. It is important to provide insights for various design decisions, effectively defining the feasible design space by considering different performance metrics and user requirements. For example, in the context of beam steering for 5G communications, achieving a low beamwidth with minimal side-lobe level is crucial to minimize interference to other network users.

In a practical scenario where the desired quality of experience is attained with a half-power beamwidth (HPBW) of 20 degrees with a tolerance of ±5 degrees and a Sidelobe level (SLL) of -13 dB with a tolerance of ±2 dB. In such a scenario, a figure of merit that encompasses both requirements can be defined as follows:

$$\mathrm{FoM1} = 1 - \mathrm{w} \cdot \delta(\mathrm{HPBW}) - (1 - \mathrm{w}) \cdot \delta(\mathrm{SLL})$$

where w∈[0,1] represents the weight assigned to the HPBW, and δ(·) denotes the distance of a metric from its nominal required value, normalized to the tolerance range. FoM1 is defined as 0 if the value falls outside the tolerance interval. Therefore, a value of 1 indicates maximum suitability, whereas a value of 0 indicates poor design. An example is shown in Figure 7.3-1 (a), which shows FoM1 for the specified conditions, with a 2-bit RIS and assuming normal incidence of impinging radio waves. In this scenario, metasurface size Dm = 4λ (Dm represents the lateral dimension of the square shaped RIS) with unit cell size Du<2λ/5 (Du represents the lateral dimension of the square shape unit cell) are the most suitable for the proposed application.

It can be seen from the formula that to satisfy a narrower HPBW requirement, the ideal RIS size will need to increase, which will shift the figure of merit to the other part of the graph. However, it should be noted that a metasurface with a size larger than Dm > 4λ will still be able to realize the ideal case for 20 degrees HPBW by switching the unused unit cells off and only engaging the unit cells in the desired lateral dimension. By doing this, engineered control of HPBW can be achieved. It is also important to note that by assuming equal importance for both metrics (w = 0,5), engineers have the flexibility to define the weights based on the specific application requirements.

Optimal performance is achieved in asymptotic cases of very large RISs with very small unit cells and a high number of states, which is impractical in real-world scenarios. Defining the application's requirements and tolerance intervals helps delineate the design space but importantly practical design guidelines should consider cost and complexity. To address this challenge, parameterized models incorporating the cost or power consumption associated with integrated circuitry can be considered for a joint performance-cost analysis. This would enable system architects to quantify different trade-offs with performance-cost figures of merit. By assigning weights to each metric, engineers can identify the optimal design space for a specific budget. In another example, shown in Figure 7.3-1 (b) an additional cost metric is added into consideration. It is assumed that the cost of the RIS scales linearly with the number of unit cells per dimension. This assumption is supported by recent studies analyzing the complexity of RIS with individually addressable unit cells. Then, the performance-cost figure of merit, named FoM2, is obtained by dividing FoM1 from the equation above by the number of unit cells per dimension and normalizing the result. It can be seen that the configurations with fewer unit cells within the range yield good performance within the tolerance range, aligning with intuitive expectations.

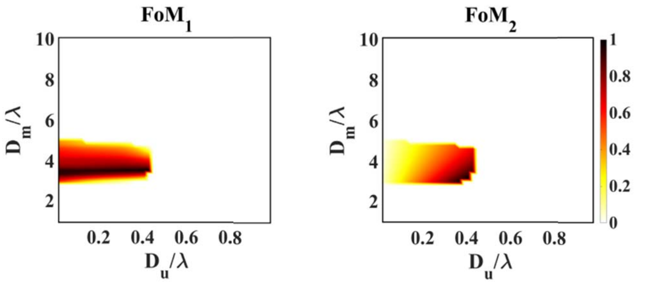

(a) Performance figure of merit. (b) Performance-cost figure of merit.

Figure 7.3-1: Evaluation, through figures of merit, of a 4-state RIS for beam steering with a beamwidth requirement of HPBW = 20◦ ± 5◦ and side-lobe level requirement SLL = −13 ± 2 dB

7.4 Other practical considerations

The present document has discussed several major directions for the development of RIS technology and provided a comprehensive list of practical considerations for its implementation/commercial deployment. The evolution of this technology is illustrated in Figure 7.4-1, which shows a transformative journey from passive to highly dynamic and active systems, marking significant advancements in the capabilities of EM manipulation. The most advanced iteration involves EM wave domain computing RIS (WDC-RIS), which is designed to receive and process signals through computational operations such as Fourier transforms directly within the analogue domain. This capability allows RIS to perform complex mathematical computations on the signals they interact with, paving the way for systems that integrate communication and processing in a single platform. These developments signify a pivotal shift towards more integrated and intelligent electromagnetic systems, capable of supporting the high demands of the next generation communications and beyond. This is made possible through STAR-RIS technology, which facilitates the manipulation of EM wavefronts via multiple layers of metasurfaces. For example, embedding a lens phase profile into the transmissive portion of the RIS allows for Fourier transformations in the K-domain. This capability is fundamental for advanced signal processing and analysis. In this case, an incoming wave that impinges on the multi-layered RIS with analogue computing capabilities can be partially reflected for communication purposes and partially sampled for processing.

The sampled portion that passes through a multilayer, metasurface would undergo computation based on specific functions and equations, demonstrating the dual functionality of communication and processing in a single integrated system. One of the most significant advantages of utilizing RIS in EM wave domain computing is its ability to perform computational operations at the speed of light, thereby bypassing the need for conversion into digital formats. This architecture may be used for distributed network processing, to ease the computational burden away from the core network and to reduce its latency. As a result, this system not only speeds up data processing but also reduces the computational load and energy consumption associated with digital conversions. Then, complex mathematical tasks such as DoA estimation, can be performed directly on the metasurface, resulting in near-zero latency of the computation in ISAC systems. WDC-RIS is also capable of performing Digital-to-Analogue Converter (DAC) and Analogue-to-Digital Converter (ADC) functionalities directly on the wavefront, as it passes through its layers, which can be used to establish a backscattering link for authentication of RIS on the network. The system models of ISAC-RIS and WDC-RIS are provided in ETSI GR RIS 006 [i.14] that is dedicated to multi-functional RIS modelling, optimization and operation.

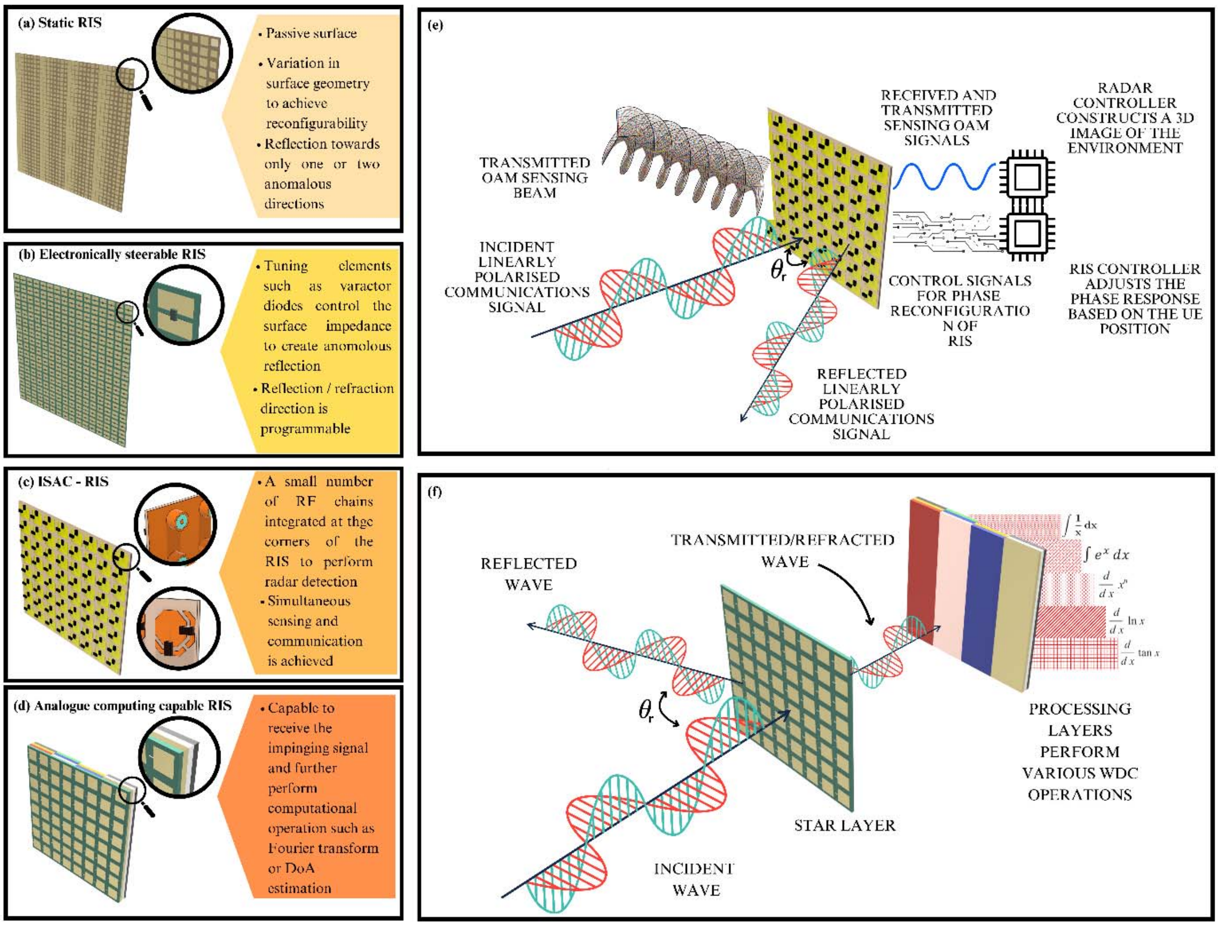

Figure 7.4-1 (a to d): Evolution of RIS from static to Wave Domain Computing (WDC)-RIS.
e) ISAC-RIS transmits and receives Orbital Angular Momentum (OAM) signals through the RF processing chains, allowing for the reconstruction of an image from the waves scattered by the environment without interference with the communication channel.
f) WDC-RIS samples a portion of the communication signal and routes it through meticulously engineered composites embedded in its STAR layer, enabling the execution of advanced mathematical operations directly on the wave in the analogue domain

The above highlights a major leap in computational efficiency and speed for the next generation of networks, firmly establishing RIS as a crucial enabler in the deployment of forthcoming high-frequency and high-speed communication systems. As this technology develops, it promises to revolutionize how data is processed and managed across vast communication networks, ensuring faster and more efficient data handling that could lead to more advanced applications and services.

8 Conclusion and Recommendations

The present document summarizes ETSI ISG RIS views on implementation and practical considerations concerning RIS, including RIS unit cell design, switching methods, RIS types, RIS controller, cost, field trials, and the measurement methods. The contents can serve as a reference point for relevant specifications and standards to study and model RIS-integrated systems.

History

Document history		
V1.1.1	March 2025	Publication